APPLICATION AND CORRELATION OF NANO RESOLUTION MICROSCOPY TECHNIQUES TO VIRAL PROTEIN LOCALIZATION

by

Jeffery Allen Hodges

A dissertation submitted to the faculty of
The University of Utah
in partial fulfillment of the requirements for the degree of

Doctor of Philosophy

in

Physics

Department of Physics and Astronomy

The University of Utah

December 2013

The University of Utah Graduate School

STATEMENT OF DISSERTATION APPROVAL

The dissertation of **Jeffery Allen Hodges**

has been approved by the following supervisory committee members:

Saveez Saffarian	, Chair	**17 August, 2013** Date Approved
Markus Babst	, Member	**19 August, 2013** Date Approved
Benjamin Bromley	, Member	**19 August, 2013** Date Approved
Jordan Gerton	, Member	**19 August, 2013** Date Approved
Orest Symko	, Member	**19 August, 2013** Date Approved

and by **Carleton DeTar**, Chair/Dean of

the Department/College/School of **Physics and Astronomy**

and by David B. Kieda, Dean of The Graduate School.

ABSTRACT

This dissertation is primarily focused on the application of super-resolution microscopy techniques to localization of viral proteins within envelope viruses.

Advances in optical super-resolution microscopy techniques have enabled scientists to observe phenomena much smaller than the Abbe diffraction limit by stochastically limiting the number of molecules excited at a given instance and localizing their positions one at a time. Additionally, methods such as Atomic Force Microscopy (AFM) allow scientists to measure the topological features and material properties of samples through contact with a force probe. This dissertation describes the application of these two techniques to virology in order to localize internal viral proteins of enveloped virions, and measure their effect on the elastic properties of the virion.

By utilizing super-resolution microscopy techniques such as Fluorescent Photo-Activated Localization Microscopy (fPALM) on virions, which have had their surface glycoproteins labeled with a photo-switchable label, the viral envelope may be accurately recovered. This dissertation describes the development and application of this technique as it applies to envelope

recovery of Vesicular Stomatitis Virus (VSV) and Human Immunodeficiency Virus-1 (HIV-1). By fluorescently labeling proteins, which are internal to each of these viruses, I have been able to localize a variety of viral proteins within their recovered envelopes. This is done without significant damage to the virion, making this method a highly effective in vivo technique. In the case of VSV, an asymmetric localization along the central axis towards the blunt 5' end was found to exist for both the polymerase and phosphoproteins. These have been determined to occupy a region in the central cavity of ~57 +/- 12 nm on the 5' end.

This inhomogeneity of the underlying proteins such an asymmetry would predict that the Young's modulus would vary along the central axis of the virion. This dissertation also describes utilizing AFM to explore and measure the variance in young's modulus between the two distinct elastic regions observed in VSV virions, which vary by 12% in elasticity. From these combined results I have found a strong correlation between the two methodologies in order to calculate the distribution of polymerases within VSV.

For Mary.

Without her love, sacrifice, support, and patience,

none of this would have been even remotely possible.

I love you.

TABLE OF CONTENTS

LIST OF FIGURES

Figure Page

LIST OF TABLES

ACKNOWLEDGEMENTS

First and foremost I would like to thank my loving family for their faith and support. They are amazing and I appreciate them more than I can express, even in the difficult times.

I would like to thank Saveez Saffarian, my graduate mentor for all the lessons he has taught me; Michael B. Landesman, a close friend and colleague who became an invaluable sounding board; Pei-I Ku and Xioalin Tang, my peers in the Saffarian lab for their efforts which contributed to this dissertation; Jordan Gerton and Anil Ghimire, for teaching me AFM and helping me through difficult experiments in addition to patiently giving me time and access to the equipment; Manasa Ghuti for teaching me PALM, and for being an excellent sounding board when experiments were tough; Eric Jorgenson for patiently allowing me to utilize his PALM equipment.

I lastly would like to thank William Evenson and Phil Matheson, my undergraduate mentors and friends whose subtle and timely encouragements for nearly a decade have changed my life for the better. Thank you all so very much.

CHAPTER 1

INTRODUCTION

Super-resolution microscopy techniques and their application to biophysics and virology have created a better understanding of viral pathogens. In order to understand the scope of the research chapters and the historical context of that research, an overview of modern techniques and tools are provided in this chapter. Additionally, an overview of relevant biology is presented insomuch as it is related to the materials contained in the research chapters.

Understanding of viral protein structure and their location within a virus is of critical importance to the understanding of viral behavior and life cycle. However, the protein configuration of many viruses is not known despite a variety of existing techniques capable of resolving such issues.

There are two principle areas of biophysical interest contained herein for the purpose of determining viral protein location within enveloped viruses. The first is the application of atomic force microscopy (AFM) and contact mechanics to viral structure and protein localization through a viral envelope. The second is the application of super-resolution microscopy techniques such as fluorescent photoactivated localization microscopy

(fPALM), or stochastic optical reconstruction microscopy (STORM) and their application to the same protein localization.

1.1 Historical Context

Throughout history, mankind has had a desire to conceptualize and understand that which could not be seen with the naked eye. In the consideration of matter itself, Democritus coined the term ἄτομος or átomos, which means indivisible, in order to philosophically describe the concept of a smallest possible particle of matter. While he did this in approximately 450 BCE, the philosophy of the atom existed among many cultures even earlier, including India in the 6th century BCE [1].

With the advent of the first optical microscope in 1590 CE by Dutch lens grinders Hans and Zacharias Janssen, realms of the universe which had been too small to be seen with the naked eye became accessible for the first time. Many scientists, such as Robert Hook, the author of Micrographia, utilized this new tool to better understand the newly accessible regime of the universe. Anton van Leeuwenhoek was one of the first to apply this tool to biological systems, and is attributed with being the first to describe cells, biological structures and bacteria using a microscope [2].

While this new tool opened several new realms of science to mankind, there was a limit to how small a microscope could see, because they are

fundamentally diffraction limited. Ernst Abbe demonstrating that, for optical microscopes [3], the diffraction limit is based upon the numerical aperture (NA) of the optical equipment and the wavelength of light (λ). This means that the distance (d) between two points that can be distinguished from one another is

$$d = \frac{\lambda}{2 \cdot NA} \tag{1.1}$$

Many modern optical systems are able to have an $NA = 1.4$, in which a green wavelength of $\lambda = 500$ nm would only distinguish between particles that were more than 180 nm apart. For this reason, individual atoms and molecules cannot be observed optically. In addition, many biological elements such as proteins, which are a few tens of nm in diameter, synaptic vesicles which are ~40 nm in diameter, and most viruses which are typically less than 200 nm in size cannot be resolved utilizing traditional methods at visible wavelengths.

The limitations of observable material, due to Abbe's diffraction limit, open the question as to how one goes about obtaining protein and particle configuration in a complex biological system, which exists entirely below this limit. Of particular interest here, is how does one obtain localization information when the proteins or particles of interest are somewhat disordered and interior to the body of the live biological sample? This question becomes especially difficult if the concentration of the proteins is on

the order of ten, hundred or thousand within a 100 nm radius of each other. These are the questions addressed in this dissertation.

1.2 Existing Technique Overview

Many techniques have been developed to work around the Abbe diffraction limit. For the most part these techniques deal with the utilization of smaller wavelengths or removal of light from the problem entirely. Each of these techniques has advantages and limitations, and should be considered individually with respect to both.

1.2.1 Electron Microscopy

Electron Microscopy (EM) utilizes matter wave theory from quantum mechanics to bypass the use of light. This works because, as shown by Louis de Broglie in his 1924 PhD dissertation [4], electrons can be treated as waves whose wavelength is many times smaller than that of light from the visible spectrum. The relationship between wavelength of electrons and their momentum (p) is related by Plank's constant (h = 6.58 eV·s).

$$h = \lambda \cdot p \tag{1.2}$$

This relationship allows an electron moving with momentum p to essentially be utilized like light, complete with transmission, reflection and diffraction. This physical principle allows the electron microscope to resolve

distances down to the 50 pm regime. A plethora of related techniques such as Transmission Electron Microscopy (TEM), Scanning Electron Microscopy (SEM), and Cryo-Electron Microscopy (Cryo-EM) have been developed and applied to biological samples [5]. These techniques have yielded a wealth of knowledge, but due to their assay requirements, they typically are very destructive to the biological sample during preparation. Samples will typically need to be metal coated, plasticized, stained, flash frozen or otherwise prepared for their target assay and vacuum imaging conditions. All of these in vitro assays have limited return of information for their sample. Coated samples typically return only topological information from outer atomic layers of the sample, TEM samples return a two-dimensional projection of electron density through a sample, and sample averaging from Cryo-EM will return only ordered periodic data within the structure of interest.

1.2.2 Atomic Force Microscopy Synopsis

A nondestructive assay for small biological samples comes in the form of Atomic Force Microscopy (AFM), which utilizes a piezoelectric driven cantilever to which a very small scanning probe is attached (typically 5 - 50 nm radius). This probe is used to feel out by touch the topological features of a sample. This method can be done on biological samples in a buffered aqueous environment, thus allowing for in vivo information gathering.

However, as the sample is felt out, only topological information for the top regions of the sample and surface characteristics such as adhesion can typically be obtained. Under the right conditions, a probe can be pressed into a soft sample in order to measure its elastic properties. This particular method is one utilized throughout this dissertation and will be discussed in greater detail later in this chapter (see section 1.3).

1.2.3 Fluorescent Labeling

By returning to optical solutions, one is still left with the diffraction limitations. The main problem with the Abbe diffraction limit [6] is resolving multiple particles of interest which are too close together. If there were only one particle of interest, the diffraction of the individual particle would return a clean Airy point spread function centered about the particle of interest. Calculation of that center becomes a simple matter in theory, but is complicated slightly by the camera technology utilized due to capture of the photon information being pixilated. The current methodologies allow for the center of a single point to be localized to within a 10 nm precision, as discussed within this dissertation (section 1.5 and Chapter 2) [7].

Several techniques have been developed in order to capitalize on this fact, but all must address the same basic problem, how to observe molecules, one at a time. Direct observation becomes a problem as most proteins are so small that they are optically transparent, and what few interactions with incident

light that do return through a microscope system will not return much in the way of a signal. Observation is thus handled through the use of fluorescent labeling [3]. This allows the particle of interest to emit its own light in a particular wavelength at vastly higher quantum yields (QY) than can be expected through direct observation. Fluorescence works by exciting an electron into a higher energy state than its ground state with a laser. As the electron relaxes back to its ground state, it emits a photon which, due to a Stokes shift [8], is of a different wavelength than then excitation laser. A system can then filter out the laser light and all but a small window of wavelengths around the peak emission wavelength in order to more easily observe the molecule directly.

In biological samples the fluorescent label for proteins is typically Green Fluorescent Protein (GFP) (see section 1.8), or one of its derivatives. GFP gene is fused to the nucleotide sequence of a protein of interest, and when the protein is folded in the cellular machinery, the GFP is folded into its configuration as well.

In recent years, linkers have been developed which can allow the GFP to be offset from the protein in order to minimize distortion of the protein's function. Once proteins of interest are labeled and both the GFP and protein are functional, they can be observed and localized; however, proteins rarely exist in a system in small enough numbers to be able to distinguish them spatially as independent sources of light. For example, glycoproteins on the

exterior of a cell membrane often exist in high densities. Having several hundred such proteins within a hundred nanometer radius of a point on interest on a cell wall would not be unreasonable. These several hundred would all exist in a region smaller than their diffraction limit, so how would a single protein would be observed?

1.2.4 Super Resolution Microscopy Techniques

In order to overcome ensemble issues with proteins, one need only to discretize the observation of a single selected protein temporally from the other proteins in the ensemble. This can be accomplished stochastically by exciting a small subset of fluorescently labeled proteins, preferably singly, and then a large number of fluorescent proteins can be observed piecewise through the same process via repetition. This would allow for the mapping of individual proteins in space. Alternatively, a deterministic approach can be used. Since laser light is utilized to excite the fluorophores, minimizing the cross section of excitation to subdiffraction limited areas would localize a fluorophore to the excitation volume only. Thus, by tracking the volume of excitation very accurately, a fluorescent signal that is observed must be local to the excitation volume, and therefore its position in space is known. To this end, the several stochastic techniques (see section 1.5) such as fluorescent Photoactivated Localization Microscopy (fPALM)[9,10] or Stochastic Optical Reconstruction Microscopy (STORM)[11], and deterministic techniques such

as Stimulated Emission Depletion (STED)[12] have been developed in recent years.

In conjunction with these methods, fluorophores (see section 1.8), which can easily be excited and quenched, have been developed in order to improve the operational characteristics of these methods. It is through these methods that resolution of discrete particles on the 10 nm scale is possible. Fortunately these methods work in a biological system, and can even be used in vivo. Typically these methods have been applied to cellular and bacterial systems; however, the emphasis of this dissertation is the application of Atomic Force Microscopy and Photoactivated Localization Microscopy to the localization of internal viral proteins within Human Immunodeficiency Virus type 1 (HIV-1) and Vesicular Stomatitis Virus (VSV).

1.3 Atomic Force Microscopy

Atomic force microscopy is a subclassification of scanning force microscopy in which a very finely tipped mechanical probe typically of radii between 5 nm and 50 nm is used to feel out the surface, and some properties of a sample. This surface interaction is a function of the Lennard-Jones potential [13] (equation 1.3), which is the sum of the attractive van der Waals forces and the Pauli repulsion due to overlapping electron orbitals (see Figure 1.1).

$$V = 4\varepsilon\left[\left(\frac{\sigma}{d}\right)^{12} - \left(\frac{\sigma}{d}\right)^{6}\right] \tag{1.3}$$

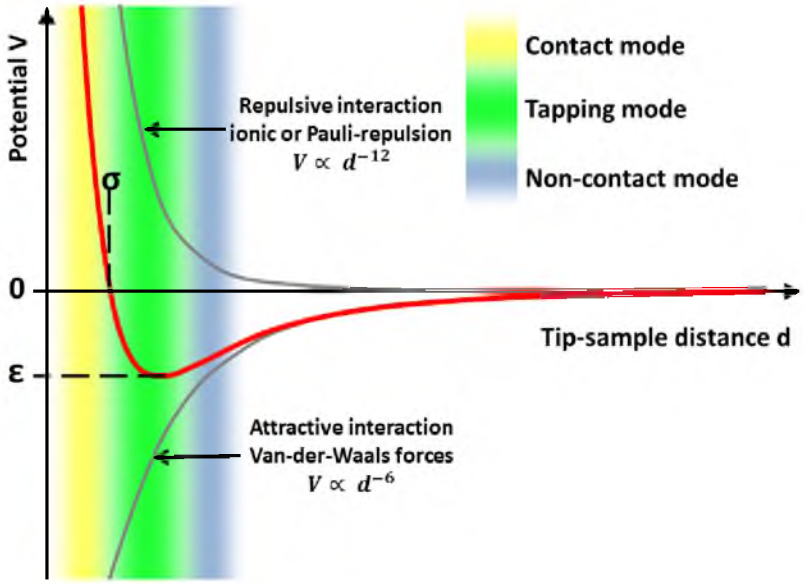

Figure 1.1 A force distance curve of the attractive and repulsive regimes in AFM. These occur from tip and sample interactions, where ε is the depth of the potential well, σ is the finite distance at which the interparticle potential is zero, d is the distance between the probe and sample.

where ε is the depth of the potential well, σ is the finite distance at which the interparticle potential is zero, d is the distance between the probe and sample.

These techniques have a demonstrated resolution on the order of angstroms, making their topological resolution approximately three orders of magnitude higher than the optical diffraction limit and comparable if not superior to many electron microscopy techniques.

The first AFM was developed by Gerd Binning, Calvin Quate, and Christopher Gerber in 1986 [14] as a variation of the scanning tunneling

microscope for which Gerd Binning and Heinrich Rohrer had earned the Nobel Prize for Physics in 1986 [15].

Perhaps the most critical component of the AFM is the cantilever which has a small sharp tip oriented perpendicularly to the cantilever arm. The cantilever is typically made of silicon or silicon nitride and is often coated in a metallic skin (typically gold). These materials are highly flexible but can vary greatly in their mechanical and material properties, which means the cantilevers and their tips can be engineered for specific application such a material property analysis of biological samples [16,17,18,19]. The tip itself can vary in shape and radius through its construction and these properties can play a role in sample interaction as well.

The system works by flexing or oscillating the cantilever. This flexing/oscillating is controlled through the use of a piezoelectric driving element. In order to determine the position and orientation of the probe, a laser is employed to reflect off of the cantilever at the position of the tip. This reflection is then recorded via a photodiode connected to the systems detector and feedback electronics. The photodiode is located relatively remotely from the tip such that small perturbations in the tip position (on the angstrom scale) are reflected as significantly larger positional changes on the photodiode. The photodiode itself is divided into four sections of detection aligned with the cantilever and can be used to not only determine changes in the Z position of the probe, but torsions exerted on the probe.

Through manipulating the conditions on the tip, the AFM can be operated in a few modes; namely, contact mode in which the tip remains in contact with the surface of the sample, noncontact mode in which the probe does not touch the surface, but instead is operated at the resonant frequency just above the sample surface, or tapping (alternating contact) mode which oscillates the tip into contact with the surface at regular intervals. These modes can be operated in such a manner as to be responsive to the surface in an attractive or repulsive manner as determined by the relationship of the oscillations to the resonance frequency of the cantilever.

Contact mode is a static mode of scanning in which piezoelectric oscillations are not applied to the cantilever. This mode works by statically dragging the probe tip across the surface lightly and deflection of the probe due to contour variations of the sample surface are recorded and a topological map of the surface is recovered. This puts the tip in the repulsive regime of a force/distance curve.

In contact mode the system maintains a constant deflection of the laser and thus scans with a constant force interaction between the tip and sample. This mode can be prone to many other types of surface interaction such as adhesion, and capillary forces which can be quite strong and cause the tip to snap violently to the surface. For these reasons contact mode is almost always done in a manner to ensure that the interaction forces are always in the repulsive regime, in order to minimize the effects of adhesive and

capillary forces. This constant interaction of the tip with the surface can be quite destructive to both the sample and the tip making this mode difficult to deconvolve laterally, as well as making it difficult to maintain constant scanning conditions.

Noncontact mode relies heavily on attractive van der Waals forces for sample interaction. These forces are typically strongest within 1 nm to 10 nm of the surface. The cantilever is oscillated either at or just above its resonant frequency specifically to take advantage of the attractive force, and respond prior to entering the repulsive regime. The attractive van der Waals force interacts with the tip and will decrease the resonant frequency of the cantilever through the tip. The decrease of the resonant frequency is fed through a feedback loop in the system which tries to maintain a constant oscillation frequency in order to have a constant distance between tip and sample. The tendency to remain in the attractive regime is determined by the amount above resonant frequency at which the tip is oscillated. This operating above the resonant frequency over dampens the oscillations making the tip more than 90° out of phase with the driving oscillation, and thus less likely to oscillate into the repulsive regime before responding to the driving force. By over damping the oscillations while using small amplitude in the tip, contact with the surface is minimized. During scanning of the tip, a topological reconstruction of the sample surface is made by measuring the tip to sample distance at scanning points on the surface. Since the tip is not

often in contact with the sample surface, neither the sample or the tip will become degraded during the scan, which makes this mode popular for scanning soft samples such as biological samples.

Tapping mode is done by driving the cantilever to oscillate up and down near its resonant frequency similarly to noncontact mode. However the amplitude of the oscillation is typically much larger than in noncontact mode and calibrated to allow the tip to touch the surface of the sample at regular intervals. This is accomplished by driving the tip just below the resonant frequency effectively under damping the oscillation (less than 90 degrees out of phase) and allowing the tip to be driven through the attractive regime and into the repulsive regime.

In order to reduce tip and sample degradation a set point is established which informs the system as to what response force in the sample will trigger a retraction of the tip from the surface. A servo adjusts the height of the cantilever in order to maintain this response force relationship between the tip and the surface. Tapping mode thus produces images by using the force interaction of the oscillatory contacts to determine height and topology of the sample. The advantages of tip preservation and force mapping make tapping mode a very powerful tool when determining material properties with respect to topological position. It is for these reasons that tapping mode is the principle method used in the paper discussed in Chapter 2.

1.4 Contact Mechanics

The response force utilized in tapping mode is highly dependent upon the material properties of the sample. A very hard material will not deform before the response force is reached, while a very soft material such as a lipid bilayer will deform significantly before the response force is reached and the tip is retracted. This pressing into the material referred to as nano-indentation distorts the true height of the sample. However, if the true height of the sample is well established, the depth of depression can be very enlightening as to the material composition of the sample.

The study of the deformation of materials that are in contact is well established [20,21]. The genesis of contact mechanics as a field of study is attributed to Heinrich Hertz in 1882, in which he solved the large scale contact problem of two elastic bodies with curved surfaces pressing into each other. The solution did not include considerations for adhesive forces, or very small scales, but it is still the principle foundation for modern contact mechanics.

It was not until the 1970's until Johnson, Kendall and Roberts established a similar formalism for cases involving adhesive contact, known as the JKR model of elastic adhesive contact. Their expansion on the Hertz model allows for properties found throughout biology to be considered during contact [20].

All of these models are based on the idea of minimizing the contact pressure by increasing the contact area (a) and its relationship to the

deformation depth (d) within the materials. In an elastic model of two spheres in contact, this interaction is additionally a function of force (F) from the applied load, the effective elastic moduli (E*), and the effective radius (R) of the spheres involved, as seen in equation 1.4

$$a^3 = \frac{3FR}{4E^*} \tag{1.4}$$

where E* is

$$\frac{1}{E^*} = \frac{1-\nu_1^2}{E_1} + \frac{1-\nu_2^2}{E_2} \tag{1.5}$$

where E_1 and E_2 are the elastic Moduli and ν_1, ν_2 are the Poisson ratios (the negative ratio of transvers to axial strain) for the spheres. The effective radius R for two spheres of radius R_1 and R_2 is

$$\frac{1}{R} = \frac{1}{R_1} + \frac{1}{R_2} \tag{1.6}$$

These equations can be combined to solve for the deformation depth as a function of applied load, radius and elastic moduli,

$$d = \frac{a^2}{R} = \left(\frac{9F^2}{16RE^{*2}}\right)^{1/3} \tag{1.7}$$

It should be noted that the solution for two cylinders or a cylinder and a sphere is the same as the solution for two spheres. For all of these solutions there is a maximum contact pressure p_0 that is related to the same variables of

$$p_0 = \frac{3F}{2\pi a^2} = \frac{1}{\pi}\left(\frac{6FE^{*2}}{R^2}\right)^{1/3} \tag{1.8}$$

By relating the contact mechanics to the force of contact between the AFM tip and the sample to the deformation depth, one can back calculate some of the material properties of a sample. In general, the elastic moduli term for the cantilever material is dwarfed by the same term for the biological sample and can be ignored. Recently it has been found that relatively thin biological materials (<100 nm in height) are not simply acted upon by the force from the tip. Instead the biological material is pressed between two probes, the first being the cantilever tip, and the second being the sample substrate whose radius is effectively a half plane, therefore to quantify the material properties one should consider the forces generated by the half plane as well. This is because the compression strains from the tip do not sufficiently disperse into the material before being reflected by a response force from the substrate. For this reason, several models to solve this problem are currently being discussed in literature, but are not discussed in this dissertation. Additionally, most biological samples are not homogeneous in their construction, which is a principle constraint for all contact mechanics models.

It is for these reasons that the effective elastic moduli of VSV are not reported in Chapter 2.

The contact mechanics models here do give us some indication as to the regime of elasticity viral samples belong in, which is widely spread throughout the megapascal range (depending on virus type). Despite these limitations, the paper presented in Chapter 2 discusses the application of differing elastic responses from one end of a virion to the other on VSV.

1.5 Stochastic Super-Resolution Microscopy

The optical resolution limits in traditional optical light microscopy are due to the diffraction limit of light as elucidated by Ernst Abbe in 1873 [6]. However, this limitation is due to the physical proximity of multiple particles to one another. When the particles of interest are within a subdiffraction limit radius of one another the uncertainties in their position overlap significantly, which makes them indistinguishable. This is a situation which can be corrected stochastically, through the application of temporal offset schemes, which is to say by observing the particles of interest individually at different times. This is typically accomplished through the use of fluorescent dyes or proteins that are discussed in section 1.8.

The complex chemical nature of many fluorophores utilized as a light source in the optical experiment means that in order for the fluorophore to emit light, it must first be activated by a photon. This activation changes the

state of the dye, making able to absorb and subsequently emit photons via fluorescence. By limiting the availability of activation photons, stochastic properties arise in how fluorophores are activated. If activation photons are sufficiently limited, single fluorophores will be activated one at a time. Once activated, a dye may be kept actively in a fluorescent state by feeding it photons to absorb in its fluorescence cycle. Eventually the chemical process within the fluorescent particle will break down due to photochemical destruction of the fluorophore molecules when exposed to the excitation light. Because of this, particles will become permanently quenched and unable to emit light, which is known as photobleaching.

Through this method, individual fluorophores may be excited, and become resolvable in time, independent of their proximity to one another. Fluorophores are then either deactivated or photobleached (depending upon technique) in preparation for the next imaging cycle. This process is iterated until the sample is depleted of fluorescence, and the images are analyzed computationally.

During imaging, photons from individually activated fluorophores form a diffraction limited spot at the image plane of the microscope and can be visualized with a photo-detector, which is typically a Charge-Coupled Device (CCD) or Complementary Metal–Oxide–Semiconductor (CMOS) camera. The resultant spot is a two-dimensional Airy function; however, due to limited photon capture and pixel size within the photo-detector, the function is

typically dominated by the central peak, which may be modeled in the form of a two-dimensional Gaussian point spread function [22]. During analysis, the center of this function is easy to determine computationally, but it is the error that determines the precision to which the location of the particle is known.

The generalized precision to which a single particle may be localized (σ) is determined by the relationship of the full width at half maximum of the point spread function (typically ~250 nm) of the fluorophore to the number (N) of photons collected by the detector. [7,23] This relationship is

$$\sigma \approx \frac{\Delta}{\sqrt{N}} \tag{1.9}$$

where Δ is the FWHM of the PSF.

It is possible to calculate a more refined localization precision by considering properties which are imaging system specific such as average background signal (b), pixel area size of the detector (a) and the standard deviation of point spread functions within the system (S_i) [24]. This yields a more refined definition of localization as

$$\sigma = \sqrt{\left(\frac{S_i^2}{N} + \frac{a^2}{12N}\right) \cdot \left(\frac{16}{9} + \frac{8\pi s_i^2 b^2}{a^2 N}\right)} \tag{1.10}$$

This type of localization technique is generally defined as a single-molecule localization method (SMLM), to which STORM, PALM and fPALM belong.

These methods were all developed in parallel by different groups at approximately the same time [9,10,25].

While STORM and PALM techniques have a common underlying principle, they differ on technical details. STORM first utilized immunolabeling of the sample with antibodies tagged with organic fluorophores. PALM was first done on biological specimens that expressed fusion constructs of photoactivatable fluorophores to proteins of interest. In application, STORM utilizes stochastic blinking of fluorophores through multiple activations to separate and exploit neighboring dies, while PALM utilizes photobleaching of fluorophores to confine the life cycle of an activated fluorophore into a limited time interval. Of important note is the difference in excitation between the two techniques. While fPALM utilizes different lasers to activate and then quench the fluorophores, STORM utilized dyes that will be activated, excited and deactivated by the same color laser. Both of these techniques have been expanded to include multiple colors of fluorophores [26] and three-dimensional imaging [27,28]. This three-dimensional imaging as determined by STORM is done by analyzing the ellipticity of a point spread function induced by a cylindrical lens. This cylindrical lens is added to the imaging path to create a different focus for the X and Y directions. Because of this, only particles half way between the two lateral focuses will appear round. When not in this position the point spread functions (PSFs) will have an ellipticity which can be used to recover the particles position in Z [29]. Three-

dimensional imaging in PALM is accomplished by imaging the fluorescence in two planes and utilizing the two variant point spread functions to determine the fluorophores position in Z [30,31].

In Chapter 2 a combined STORM/PALM technique of endogenously expressed fluorophores (eGFP) and immunolabeling of viral envelopes with fluorescently tagged fluorophores (Alexa647) in three dimensions is utilized to determine the center of mass localization of viral proteins in VSV and HIV-1. The three-dimensional localization is recovered using the fPALM biplane methodology; however, the problem discussed was determined to only need consideration of axial offset in one dimension along the central shaft of the virion. Using this technique it was determined that critical proteins important to VSV replication were asymmetrically located to one side of the mature virion.

1.6 Total Internal Reflection Microscopy

While the fluorescence of single fluorophores may yield important information regarding biological configuration, bulk behavior of a system may be studied as well. In Chapter 4 we have utilized the bulk fluorescence of pH dependent dies to study the permeability of viruses to protons. When studying pH dependent behavior of viruses, it is beneficial to limit the field of fluorescence excitation. This may be done through use of the evanescent wave

produced by total internal reflection, as explained by Daniel Axelrod in 1981 [32,33]. The technique is known as TIRF microcopy.

In order to understand how TIRF works, it is important to understand the foundation of evanescent waves. When considering solutions to Maxwell's equations to waves experiencing total internal reflection, there is no solution in which the incident wave is entirely reflected. Instead there is always a component of perpendicular transmitted wave due to boundary condition continuity. This is because the perpendicular components of the magnetic field (H) interfere constructively, so they never diminish to zero, and thus, there will always be a component of transmitted wave. However, due to energy conservation, the wave cannot be sinusoidal or traveling wave, else it would transport energy away from the boundary. The only solution which fits these parameters is an exponentially decaying plane wave referred to as an evanescent wave [34].

This evanescent depth is highly dependent on incident angle and wavelength of the incident light, which allows for control of excitation volume. This controllable excitation volume is perfect for studying low volume systems, such as viruses. For optical wavelengths the evanescent wave can be used to excite fluorophores within ~200nm of the glass-media interface.

Because this system has an exponential decay in the nanometer regime, variation of interface position by just a few nanometers can have a significant

effect on fluorescent excitation within the volume. Typically this is not a problem; however, in assays where sample buffer may be exchanged, pressure differentials between the two states and/or during media exchange may easily flex a sample substrate and excitation volume out of focus. In order to correct for this, a TIRF clamp is employed in order to ensure the excitation volume is always in focus. The TIRF clamp works by utilizing the back reflected light from the sample glass on a quadrant photodiode to maintain a constant focal position. If an established focal plane drifts even slightly, the back reflectance detected in the quadrant photodiode will change, and indicate to the system to adjust the focus back to the original focal plane.

In Chapter 3, total internal reflection microscopy is utilized to explore membrane permeability characteristics of both VSV and HIV-1. Bulk fluorescent intensity was measured on pHluorin (see section 1.8.2) at different pH values, as well as their intensity progression with respect to time. The resultant permeation characteristics for both VSV and HIV-1 closely resemble the characteristics of liposomes, which are typically of similar size and made entirely of lipid membranes.

1.7 Biological Samples

A significant benefit of nano-resolution and super-resolution techniques described in sections 1.3 – 1.6 is their application to biological systems in a nondestructive manner. While cells and many other biological factors may be observed through standard optical techniques, it is the super-resolution techniques that allow study of the diffraction limited aspects of biology. Not the least of which is virology.

1.7.1 Vesicular Stomatitis Virus

VSV is of particular interest to virologists because it has many useful properties. VSV has been used in oncolytic virotherapy because of its capacity to preferentially infect most human tumor cells, as reviewed in February of 2012 by Russell in *Oncolytic Virotherapy* [35]. The VSV-G protein is commonly used in biomedical research to pseudotype retroviral and lentiviral vectors, conveying the ability to transduce a broad range of mammalian cell types with genes of interest [36].

Vesicular stomatitis virus is a bullet shaped single strand negative sense RNA virus ((-)ssRNA) of the order mononegavirales. It is on average 180 nm long by 80 nm wide, and its RNA orientation within the nucleocapsid is such that the 3' end is within the prolate curvature of the nucleocapsid. This RNA orientation is determined through tight fitting of RNA within N crystal structure and fitting of N in the single particle averaging of the VSV bullet.

VSV RNA consists of five major proteins (11,161 nucleotides) whose transcription is initiated in line from the transcriptional promoter located at the 3' end of the RNA. These are, in order from the 3' end: the nucleoprotein (N) which encapsidates the RNA into a nucleocapsid; the phosphoprotein (P) which is involved in different stages of the viral replication process; the matrix protein (M) which associates the nucleocapsid to the plasma membrane; the glycoprotein (G) which facilitates viral entry into a host cell; and the large protein (L), otherwise known as the polymerase, which is responsible for transcription of the RNA template.

Because VSV is a (-)ssRNA virus, host polymerases cannot replicate the genome. Instead specific RNA dependent polymerases must be packaged into the viral envelope in order to facilitate viral replication in a host cell. This is done in congress with cofactor phosphoproteins, which facilitate association of L with the nucleocapsid [37].

While the envelope structure of VSV, and its associated G, M, and N proteins are well understood [38], localization of the polymerase and phosphoproteins had not been previously established. The localization of L and P is the topic of the paper in Chapter 2 [39]. In order to understand how the research in those chapters was accomplished, it is important to understand the role and configuration of the envelope associated proteins, not just the role of L and P.

Surface glycoproteins mediate the virus being rapidly endocytosed into a host cell through a clathrin coated vesicle pathway by attaching to a host cell LDL receptor [40]. After endocytosis, the glycoprotein facilitates fusion of the viral envelope with the endosomal membrane allowing for the release of the nucleocapsid into the host cell's cytosol [41]. It is the glycoprotein which forms the basis of the tethering assay discussed in Chapter 4.

In budded virions the VSV matrix proteins are associated with the interior face of the viral envelope and cellular plasma membrane. They consist of 229 amino acids (26.6 kDa) with a positively charged N terminus. The primary function of M is seen during viral budding in which it self-associates with the host cell membrane and facilitates association of the VSV nucleocapsid to the same [42]. Additionally, M functions as a cytotoxic agent that rounds the host cells up and inhibits endogenous protein expression.

The VSV nucleoprotein associates tightly with the VSV genomic RNA and, encapsidates the RNA to protect the genome from the cellular environment during all stages of viral replication [43]. It is believed that this allows the virus genome to avoid detection and degradation by the host cell defense mechanisms, as reviewed in *Nucleoproteins and Nucleocapsids of Negative-Strand RNA Viruses.* [44]. This complex known as a ribonucleoprotein (RNP) forms a left handed helical template along the central shaft of the assembled virion [38]. This template also functions as a substrate for the RNA-dependent RNA polymerase L and associated P proteins during replication.

The position of G, M and N along with the RNA has been established in CryoEM [38]; however, the protein density averaging technique failed to clarify the location of the L and P proteins within the central cavity. This may be due to an inherently disordered nature of the proteins within the central cavity, or it may be due to a significantly differing periodicity of the L and P proteins within the assembled virus. Despite this, Chapter 2 discusses research establishing that both the L and P proteins are asymmetrically located near the 5' blunt end of the virus.

1.7.2 Human Immunodeficiency Virus Type One

Human immunodeficiency virus is a genus lentivirus of the retrovirdae family. A retrovirus HIV is of particular interest to study because it is a human pathogen, with variants being pathogenic to many other mammals. In particular the HIV-1 virus causes acquired immunodeficiency syndrome (AIDS). It does this by attacking T cells in the immune system and lowers their concentration in the body. Opportunistic diseases such as infections and pneumonia then attack the body with a compromised immune system, which may be lethal.

Two species of HIV have been characterized, type one and type two. Of principle interest here is HIV-1, or more specifically virus like particles (VLPs) of HIV-1, which allow for the noninfectious study of the virus.

HIV-1 is an enveloped spherical virus approximately 120 nm in diameter [45]. It is a lentivirus, meaning it has a delay in onset of infection, and it is part of the retrovirus family meaning it inserts a copy of its genome into the DNA of the host cell in order to replicate. The lentivirus taxonomy is due to an asymptomatic phase of variable length in which it is known that the virus has a low steady-state plasma viremia and few overt symptoms. However, during this phase the virus is known to be replicating at high levels, but not accumulating. This is because host system infected lymphocytes are quickly cleared by immune response [46]. Despite this, HIV-1 eventually decimates the body's natural defenses and immune system, leading to immunodeficiency, namely AIDS [47]. Despite this latency period, HIV replicates in a complex pattern, and during acute infections it replicates and overwhelms the immune system very quickly.

The HIV-1 virus is a complex configuration of 9 genes. Three of these genes (gag, pol and env) are contained in all retroviruses, while the remaining 6 genes tat, rev, nef, vif, vpr, and vpu make up the rest of the HIV-1 genome. These 9 genes encode 15 proteins which are assembled to form a new virion at the plasma membrane of the host cell. Among these proteins, the Gag gene, Gag-Pol gene, Env gene, and tRNA are all essential for viral replication, as well as the two copies of genomic RNA and lipid envelope.

Upon budding out of the host cell, HIV-1 recruits the host cell Endosomal Sorting Complex Required for Transport (ESCRT) complexes in order to

facilitate assembly and escape as reviewed in 2012 by Wesley Sundquist [48]. These components and their association with host cell ESCRT proteins have been heavily studied as reviewed in 2008 by Calrson [49]. There are several other accessory proteins, such as Alix which have occasionally been found in HIV-1 VLPs but are less well understood.

HIV-1 is initially released from the host cell in an immature configuration which is noninfectious. This immature particle is comprised of a layer of uncleaved Gag polyproteins on the internal face of the viral envelope. In time the immature viral particle is converted into the mature, infectious virion by the viral protease cleaving Gag in five distinct positions [50]. The cleaved proteins then form a protective nucleocapsid around the two copies of the genomic RNA.

In Chapter 2, HIV-1 VLPs pseudotyped with VSV G have been labeled on the internal portion of the transmembrane protein with eGFP. The VSV G protein is utilized to tether the HIV-1 VLPs to the glass substrate, as well as provide an immunolabeling site for VSV G antibodies labeled with alexa647 for envelope recovery. These two fluorescent signals are utilized to test the colocalization of proteins, as being labeled on both sides of the same protein, the signals theoretically should colocalize. In Chapter 3 the permeation characteristics of both mature and immature HIV-1 VLPs are quantified and compared utilizing pH sensitive pHluorin.

1.7.3 Lipid Membranes

In Chapter 3 the permeability of viruses to protons is considered. Many envelope viruses incorporate specific protein channels that regulate the permeation of protons across their membrane [51,52,53,54]. Because of this, many virologists believe that envelope viruses are typically impermeable to protons. When considering the composition of lipid bilayers, and permeation characteristics of small lipid based vesicles within a cell, this is not likely true, but instead the envelope proteins regulate permeation independent of envelope permeability.

It is know that lipid bilayers, without considering associated membrane proteins, consist of three basic components, namely phosphoglycerides or phospholipids which make up the majority of the bilayer, sphingolipids, and cholesterol. As envelope viruses obtain their lipid envelope from the host cell, the configuration of these three components within the lipid bilayer has a significant effect on the behavior and material properties of the lipid bilayer in both cells and viruses. These properties include fluidity, permeability and diffusion across a lipid bilayer. As such their structure is important to understand.

Phospholipids are based on a glycerol-3-phosphate with a hydrophilic phosphatidyl head, and a hydrophobic fatty acid tail or tails. The configuration and orientation of phospholipid head groups play a significant role in bilayer stability, function and electric charge, all of which can effect

permeation. For example, phosphatidylethanolamine (PE), which has a zero net charge head, and phosphatidylserine (PS), which has a -1 net charge head, are typically found on the cytosolic side of membranes and vesicles, while Phosphatidylcholine (PC) and the sphingolipid sphingomyelin (SM), both of which have a zero net charge head, are typically found in the extracellular space. This asymmetry is not well understood, but it is well established that it plays a critical role in many cellular activities [55]. For example, the scrambling of this asymmetry via a scramblase will cause PE and PS to be on the cell surface, and this signals to macrophages to phagocytose the cell. The orientation of this asymmetry depends on the genesis of the lipid bilayer [56], and can vary in composition accordingly. Additionally, the orientation of the fatty acid chains give most phospholipids a cylindrical occupational volume, however, flexion in the fatty acid chains of PE give it a slight conical shape which is tapered at the lipid head. This can have a significant effect on curvature and malleability of the lipid bilayer. This curvature is very important in small radius vesicles and viruses alike.

Sphingolipids in most lipid membranes are predominantly made up of sphingomyelins (SM) or glycosphingolipid, which both have a sphingoid backbone that is typically attached to a hydrophobic fatty acid, and both of which are associated with a head group. This head group of sphingomyelin typically consists of a phosphoethanolamine, phosphorylcholine or a

ceramide, all of which have a zero net charge. The head group of a glycolipid is a carbohydrate with a -1 net charge.

Cholesterol is the third basic lipid membrane component and consists of a rigid steroid ring structure for a body, with a polar head and a nonpolar hydrocarbon tail. This polar configuration typically aligns the head with the hydrophilic head and the nonpolar tail with the hydrophobic tails of lipids. Cholesterols often associate with phospholipids within the bilayer and will change the physical properties of the lipids they are associated with. For example, when associated with PC the fatty acid tails of the PC will straighten slightly, and as a result thicken the lipid bilayer. The thickness of a lipid membrane is important as this stretching from cholesterol is also a control for which membrane proteins will associate with the region due to protein length through the lipid bilayer.

Fluidity is controlled by configuration of tail groups. The more ordered the tail groups of the lipids, the straighter they are and the more rigid or gel like the membrane within the layer. The more gel like/less fluidic in nature of lipid rafts prevents lateral diffusion of lipids within the membrane and can lead to ordering defects, which will be discussed later as transient pores that, as we will discuss later, can allow proton and ion diffusion across the membrane through structures known as transient pores.

Due the existence of their hydrophobic tails and hydrophilic heads, lipids will spontaneously form into lipid bilayer liposomes (50-200nm in diameter)

in water, assuming their critical concentrations are sufficiently high enough. Typically the concentrations at 37°C are 10^{-10} Molar for lipid bilayers. These facts are not only the basis for the cell wall, but also for the entire family of vesicles which can be found within a cell. This would include synaptic vesicles, multivesicular bodies, and even the viral envelopes of VSV and HIV-1.

Typically when discussing the properties of the cell membrane, textbooks [57] refer to the membrane as compartmentalizing the cellular environment from the extracellular environment and as being selectively permeable to molecules, and ions. This selective permeability is a control over the cellular environment; however, this property is not the same for all lipid membranes [58], and many phospholipid membranes have been shown to be diffusively permeable in some small degree. It is these small liposomes which give reason to believe that the envelope of viruses is permeable independent of regulatory proteins because they are of approximately the same size. However, as discussed in Chapter 3, envelope protein concentration may play a significant role in permeation characteristics.

1.8 Fluorophores

As discussed previously, fluorescence microscopy works by exciting an electron within a fluorophore into a higher singlet energy state (S_1) than its singlet ground state (S_0) with a laser, after which the electron relaxes back to

its ground state by emitting a photon. The term singlet is in reference to the spin multiplicity of the electron, and its having a total spin of zero. In most cases the emitted photon has a lower energy than that of the excitation photon, and as such it has a longer wavelength. This difference between absorption and emission photon energy is known as a Stokes shift, and is the result of a variety of internal energy loss mechanisms. Because of this Stokes shift a system can filter out the laser light and all but a small window of wavelengths around the peak emission wavelength in order to more easily observe the particle directly. Under some conditions it is possible for the electron to transition into a triplet state (total spin of one) before emitting a photon and returning to the ground state. However, this is categorized as phosphorescence, and is not a topic considered in this dissertation.

The standard means for visualizing this absorption and emission process is a Jablonski diagram (Figure 1.2) developed by Alexander Jablonski in 1935 [59]. In the diagram, nonradiative transitions are indicated by dashed arrows and radiative transitions by solid arrows. The vibrational ground states of each electronic state are indicated with thick lines, the higher vibrational states with thinner lines [3].

1.8.1 Green Fluorescent Proteins

Green fluorescent protein (GFP) is a 26.9 kDa protein composed of 238 amino acid residues that are fluorescent (509 nm wavelength) when exposed

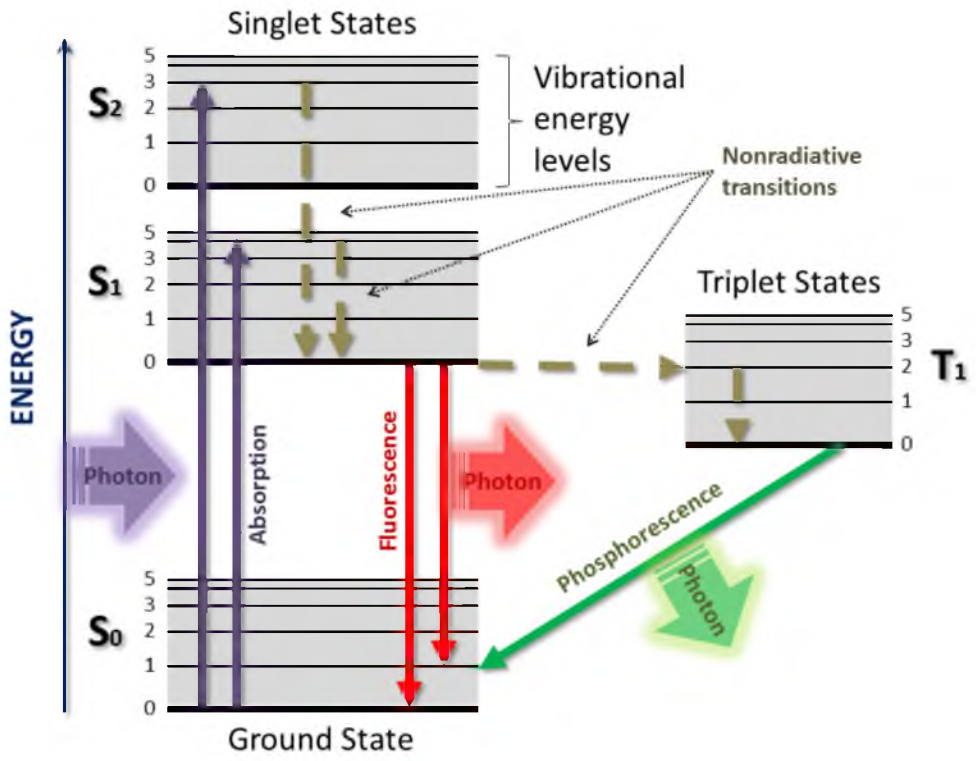

Figure 1.2 A typical Jablonski diagram showing both fluorescence and phosphorescence.

to light in the blue to ultraviolet region (360 nm to 475 nm) of the electromagnetic spectrum [60]. The use of fluorescent markers such as GFP in biological samples has become the standard for localization of proteins. The center of mass of these small particles can be localized to within 10nm utilizing the Thompson method [7] (see Chapter 5).

The structure of the GFP [60,61] consists of eleven ß-sheets and six alpha helices [62] arranged in a barrel scaffold, with the functional group chromophore centrally located within the barrel. The ß-sheets within the walls of the barrel protect the chromophore from interaction with water and

other solvents, thus shielding its fluorescence from quenching. GFP fluorescence is due to the inward facing side chains from the barrel structure, which induce specific ionization driven cyclization reactions in the tri-peptide Ser65–Tyr66–Gly67 of the central chromophore. This chromophore is a 4-(p-HydroxyBenzylidene) Imidazolidin-5-one (HBI), and is covalently bonded to the rest of the GFP structure. The cyclization reactions are driven by ionization specifically involving donation of a hydrogen atom from serine 65 to glutamate 222, which influences chromophore ionization during the cycle [63].

The ionized chromophore undergoes a conformational change of the molecule such that electrons will jump between energy levels of extended pi orbitals. These pi orbitals are created by a series of alternating single and double bonds, and it is the relaxation by the electrons during this cyclic change in energy levels which releases the photons observed as fluorescence. In a Jablonski diagram this can be seen as a fluorescent relaxation to a lower energy state, complete with a Stokes shift between the excitation and emission wavelengths, discussed above.

In wild type (wt) GFP, unless the chromophore is properly folded into is scaffold it will mainly remain in the unionized, state thus nonfluorescent. When properly folded, the hydrogen-bonding network and electron-stacking interactions with the side chains of the chromophore influence the color, intensity and photo-stability of GFP and its numerous derivatives [64].

In nature, Aequorea Victoria, a jellyfish, utilizes the wt GFP co-expressed with the separate luminescent protein aequorin as its system for bioluminescence, and it was this system that was first quantified for fluorescent proteins. The aequorin in A. Victoria is activated by a chemical bond of specific sites to Ca^{2+} ions, which converts through oxidation its tightly bound coenzymes, coelenterazine (a luciferin), into excited coelenteramide and CO_2. As excited coelenteramide relaxes to the ground state, it will emit a Stokes shifted blue light (wavelength = 469 nm). Some of this luminescent energy is transferred to the GFP, exciting it and activating the chromophore. This sharing of photons gives wt GFP with aequorin a primary excitation peak at a wavelength of 395 nm and a secondary excitation peak at 475 nm from the GFP which can be excited by blue emissions from the aequorin. Upon relaxation of the GFP, the emission peak is Stokes shifted to 509 nm, which is in the green portion of the visible spectrum. This shifts the overall color of the aequorin towards green [61,65].

Many derivatives and alternatives of the original A. Victoria GFP exist. The first major improvement was a single point mutation S65T [64] which improved the overall characteristics of GFP, resulting in a shift of the major excitation peak to 488 nm along with an increase in fluorescence and photostability. The emission peak of the S65T mutant remains at 509 nm, which brings both the emission and excitation peaks in line with commonly used filter sets. Additionally, enhanced GFP (eGFP) [66] introduced a 37 °C

folding efficiency point mutant F64L to the S65T mutation scaffold which solved a temperature based folding issue with A. Victoria GFP, and allowed the practical use of GFPs in mammalian cells. The fluorescence quantum yield (QY) (photons emitted/absorbed) of eGFP is 0.60 as opposed to the QY of 0.79 for A. Victoria GFP, but the availability of eGFP at mammalian temperatures makes it the standard in mammalian biology.

1.8.2 pH Sensitive Fluorophores

While all fluorophores are sensitive to changes in pH to some very small degree [67], and eGFP can be utilized as a pH indicator (pKa = 6.0) [68], derivative fluorophores known as pHluorins that are highly sensitive to pH have been developed [69]. These pHluorins can partially or completely quench based on proton concentration in their environment, with a high fluorescence correlation to the bulk pH in the system. This is due to the likelihood of protonation of individual pHluorin at a given pH. The underlying chemistry for the two excitation maxima of GFP is protonated and deprotonated states of Tyr 66, which forms part of the chromophore. The GFP is trapped in one of two alternative conformations. In the first conformation the chromophore is protonated and can be excited at 395 nm. In the second conformation the chromophore is deprotonated and can be excited at 475 nm. In order to facilitate the switching between protonated and deprotonated states, and couple those changes to the bulk pH of the chromophore's

environment, histidines were positioned near key residues in the Tyr-66 proton-relay network [70]. These histidines facilitate protonation through the neighboring hydroxyl group. Histidines were chosen because their acid dissociation constant pK_a (pH 7.1) is appropriate for the biochemistry involved in synaptic pathways, the original motivation for the development of pHluorins [69].

Two forms of pHluorins resulted from these mutations. Ratiometric pHluorin shifts excitation from 395 nm to 475 nm as pH is lowered while maintaining overall excitation properties. Ecliptic pHluorin (e-pHluorin) gradually loses fluorescence as pH is lowered, until at pH values of 6.0, the excitation peak at 475 nm vanishes completely. In an environment of pH <6.0, the protein is therefore eclipsed (invisible) under 475-nm excitation, but the chromophore can still be weakly excited at 395 nm. These changes are reversible within 20 ms after returning to neutral pH [69]. This is a powerful tool, which allows for observation of many chemically dependent (pH) processes in the cell.

In the original consideration of synaptic vesicles, pHluorin on the interior of acidified synaptic vesicles (pH 5.6) were fused to pH neutral vesicles (pH 7.4) of hippocampal neurons. In these cases ecliptic pHluorin that had been quenched recovered its fluorescence upon integration with the pH 7.4 environment [69].

Additionally, ecliptic pHluorin can be used to observe synaptic vesicle interactions with respect to both endocytosis and exocytosis throughout the transmission pathway. All synaptic vesicles have obligatory transport proteins which are a proton pump that generate low pH (~5.4) within the vesicle in order to signal it for uptake by the neurotransmitter. The pH gradient across the vesicle membrane is created by V-ATPase which utilizes ATP for energy. An ensemble of internally labeled pHluorin within a synaptic vesicle that is acidified would not fluoresce until the neurotransmitters associated with the vesicle are released into a higher pH environment (pH 7.4 for typical cytosol), where the pHluorin will return to fluorescence. These vesicles are very simple in construction, mainly due to their limited size of 40 nm diameter. This volume limits the number of proteins capable of fitting into the spherical vesicle.

It is these properties of ecliptic pHluorin that make them highly desirable for permeation studies in viruses. Specifically the pK_a (7.18) and ecliptic quenching properties fit well with viral entry and environmental conditions encountered by the virus within a cell. It was the protein of choice for the research covered in Chapter 3.

The application of pHluorin to other small volume problems such as multivesicular bodies (MVB) has garnered information regarding proton diffusion across lipid membranes that do not have proton pumps available for gradient maintenance [71]. In these studies, super-ecliptic pHluorin could be

seen to quench over time across lipid membranes, which is conventionally believed to be proton impermeable.

It is important to understand that bulk pH properties and kinetics are difficult to apply at such volumes, since the external volume of a 40 nm diameter sphere is only ~34 zeptoliters (10^{-21} L or $10^3 nm^3$). The internal volume would be only ~14 zeptoliters if one assumes a 5 nm lipid envelope, and the internal protein concentrations would be quite large. One can easily calculate the number of protons for a particular pH in such a volume and find that the internal volume has ~0.001 protons in that volume at pH 7.4, and ~0.1 protons at pH 5.6. The current models do not allow for bulk protonation of many pHluorin with subunit protons. The pHluorin needs a discrete proton in order to be protonated, and thus quenched [67]. As the charge on protons is discrete, these subunit numbers in the volume must relate to the activity of the proton, possibly the temporal availability of a free proton. This does not contradict the assumption that protonation at a single site will quench a pHluorin when one considers the kinematics of a proton in cytosol with respect to the recovery time of a pHluorin. If one considers the temporal resolution of the intensity variant of the Henderson-Hasselbach equation (equation 1.11) to be much larger than that of the transition time between proton sinks within the system, then an effective subunit proton can be considered as the average availability of a free proton without considering the discrete kinetics of all protons involved in the system.

$$\Delta I = \frac{1}{1 + 10^{pKa-pH}} \tag{1.11}$$

where ΔI is the relative intensity to a completely unquenched system.

1.9 Surface Chemistry for the Adhesion of Viruses to Glass

For many nano-scale microscopy assays, surface charge density on a glass substrate can function as either a bane or a boon. Protein adsorption due to charge density is commonly used in electron microscopy grids and substrates in order to adhere proteins tightly to a surface prior to insertion into the vacuum chamber. However, such protein adsorption can have a highly distortive effect on the topology of soft samples, such as envelope viruses.

Topological distortion is of particular concern when working in methods such as atomic force microscopy (AFM), a very valuable tool for studying viruses [72]. Enveloped viruses often have many surface proteins which may interact with the glass surface through an electrostatic attraction. This interaction can convolute both the height and shape of the virus away from its natural shape, or add tension forces within the virus that can perturb material properties such as the Young's modulus. This can be a significant problem as material properties are widely studied in order to better understand their configuration [73], as well as their behavior and conformational properties [74]. In order to reduce this distortion, it becomes

important to decrease protein adsorption to the glass surface while maintaining adhesion of the virus to the same glass surface. These are seemingly mutually exclusive conditions. However, with proper surface chemistry, both conditions can be obtained.

Poly(ethylene glycol) (PEG) is a thin film surface graft that provides surface resistance to nonspecific protein binding [75,76,77]. This surface resistance is due to a steric repulsion that prevents direct interaction between proteins and the glass surface [78]. This protein repulsion supplies an effective barrier to electrophilic interactions of viral proteins with a charged surface. On its own, PEG will not easily absorb onto glass surfaces. It must be grafted to the surface in order to achieve surface densities capable of protein repulsion. When grafted to a poly(L-lysine) the resultant poly(L-lysine)-graft-poly(ethylene glycol) (PLL-g-PEG) graft will easily adsorb to a glass surface and provide the desired protein repulsion.

Since PLL-g-PEG on its own will prevent viral adhesion to the surface, a viral tether to the surface is necessary. Through the functionalization of the PLL-g-PEG with biotin, a foundation of limited adhesion sites can be achieved. This is accomplished by having the desired percentage of PEG-biotin grafted to the poly(L-Lysine) at the time of grafting. For the purposes of viral adhesion we utilize a PLL(20)-g[3.5]-PEG(2)/PEG(3.4)-biotin(20%) (manufactured by SuSoS) which provides between 15% to 25% functionalized biotin on a coated surface. Each of these biotin potential binding locations can

be functionally enhanced by the addition of tetrameric avidin or NeutrAvidin (Invitrogen A2666) to the PEG treated thin film surface. The biotin-avidin bond has a very low dissociation constant and is one of the strongest known noncovalent bonds [79]. This allows for significantly more massive particles such as a virus to be tethered to a PEG treated surface. Viruses are not naturally binding to biotin, so the addition of another intermediary is required. By using a biotinylated virus specific antibody, a virus can be made to associate with an avidin treated surface. This can be accomplished in one of two ways, depending on desired results.

The first method is to treat the avidin surface with biotinylated antibody prior to viral adhesion. With this method antibody concentration can be controlled and viral adsorption to the surface can be diluted according to desired result. Additionally, antibodies that tether the viral particle to the surface are found near the surface and will not significantly affect viral topology in AFM experiments.

The second method is to attack the virus in solution with the biotinylated antibody prior to adhesion of the viruses to the avidin treated surface. This method has the advantage of allowing the antibody treatment to be designed according to optical results. For example, in our experiments biotinylated antibody is mixed with fluorescently labeled antibody in ratios that allow for sufficient adsorption of the virus to the avidin treated surface while maintaining a high concentration of fluorescent label on the exterior of the

viral envelope. This can be an advantage when attempting envelope recovery in viral protein studies utilizing PALM.

The resultant biotin-avidin-biotin-antibody tether will strongly bind the virus to the substrate while the PEG thin film maintains its protein repulsion characteristics.

1.10 Chapter Conclusion

The materials contained in sections 1.1 - 1.9 give a foundation upon which the research contained in the remaining chapters are based. From this foundation the biophysical properties of VSV and HIV-1 VLPs have been studied in order to determine a variety of important viral characteristics, including the permeability of VSV, mature HIV-1, and immature HIV-1 as well as the protein localization of VSV L and VSV P within the central cavity of the VSV virion, none of which were previously known.

CHAPTER 2

ASYMMETRIC PACKAGING OF POLYMERASES WITHIN VESICULAR STOMATITIS VIRUS

Jeffery Hodges[1,2], Xiaolin Tang[1,2], Michael B. Landesman[1,2], John B. Ruedas[3], Anil Ghimire[1], Manasa V. Gudheti[4,7], Jacques Perrault[3], Erik M. Jorgensen[5,7], Jordan M. Gerton[1,6], and Saveez Saffarian[1,2,7*]

[1] Dept. of Physics and Astronomy, University of Utah
[2] Center for Cell and Genome Science, University of Utah
[3] Dept. of Biology, San Diego State University
[4] Vutara, Inc., Salt Lake City, UT
[5] Howard Hughes Medical Institute
[6] Dept. of Bioengineering, University of Utah
[7] Dept. of Biology, University of Utah
*Correspondence to: saffarian@physics.utah.edu

This article has been published in the journal Biochemical and Biophysical Research Communications, Volume 440, Issue 2, 18 October 2013, Pages 271-276, ISSN 0006-291X, http://dx.doi.org/10.1016/j.bbrc.2013.09.064.
http://www.sciencedirect.com/science/article/pii/S0006291X13015453

2.1 Chapter Introduction

As mentioned in Chapter 1, this chapter is based upon a paper accepted for publication in which the localization of the polymerase and phosphoproteins within the central cavity of fully formed vesicular stomatitis virus are determined. These proteins were localized through the application of contact mechanics via AFM to the viral body in which a variance in elastic properties was found along the central axis of VSV, near the blunt end of the bullet shaped virus. This variation in elasticity is most easily attributed to increased protein density within the central cavity of VSV. The Matrix protein M and the nucleoprotein N are distributed uniformly along the inner leaflet of the VSV envelope [38], therefore any elastic variation along the central axis would not be expected.

In order to determine the protein makeup of the underlying protein density, a combined STORM/PALM super-resolution microscopy technique was employed in which the viral envelope was immunolabeled with a photo switchable fluorophore, while proteins of interest were labeled with eGFP. The center of mass for these two fluorescence signals were compared, and an offset that correlated to the same asymmetry found in the AFM studies was found to exist for both the L and P proteins of VSV. This implies that there is an asymmetric packaging of the L and P proteins within the central cavity. It is important to note that because of the use of eGFP instead of a photo-switchable label on the proteins of interest, the topological configuration of

the resultant mass was not obtained. Additionally, the assay was performed on virions which had been harvested from host cells and stored for a short time prior to the research being performed, so it was not determined if the asymmetry is a product of viral assembly, or maturation.

2.2 Abstract

Vesicular stomatitis virus (VSV) is a prototypic negative sense single-stranded RNA virus. The bullet-shape appearance of the virion results from tightly wound helical turns of the nucleoprotein encapsidated RNA template (N-RNA) around a central cavity. Transcription and replication require polymerase complexes, which include a catalytic subunit L and a template-binding subunit P. L and P are inferred to be in the cavity, however, lacking direct observation, their exact position has remained unclear. Using super-resolution fluorescence imaging and atomic force microscopy (AFM) on single VSV virions, we show that L and P are packaged asymmetrically towards the blunt end of the virus. The number of L and P proteins varies between individual virions and they occupy 57 ± 12 nm of the 150 nm central cavity of the virus. Our finding positions the polymerases at the opposite end of the genome with respect to the only transcriptional promoter.

2.3 Author Summary

Vesicular Stomatitis Virus (VSV) primarily infects animals. Humans have innate immunity to VSV, however it can selectively grow in human cancer cells. VSV has a single stranded negative sense genome and packages an RNA dependent RNA polymerase to transcribe and replicate this genome in its host. This genome organization is shared with Ebola virus which is one of the most deadly human pathogens with a case fatality rate upward of 80%. VSV's ability to grow rapidly in cell cultures and its ease of genetic manipulation has made it a good model virus for more deadly pathogens and also a potent tool for vaccine development and anticancer therapies. VSV genome template has a single transcriptional promoter at the 3' end where the polymerases have to engage to start the transcription. The position of polymerases within the central cavity of the virus was not known. Here we have used single virus imaging tools to find that polymerases are stacked at the 5' end of the genome, at the opposite end with respect to the only transcriptional promoter within the cavity.

2.4 Introduction

Vesicular Stomatitis Virus (VSV) possesses a single-stranded negative sense RNA genome and is the prototypic model for understanding transcription and replication of potent human pathogens including Ebola and rabies. VSV is also an effective oncolytic agent since some attenuated VSV

strains replicate preferentially in malignant cells [35]. Taken together, VSV is emerging as a useful model and potent tool in the arsenal of modern medicine.

VSV virions are 180 nm long and 80 nm wide and resemble a bullet with one tapered and one blunt end. The VSV genome is tightly encapsidated by nucleoprotein (N), forming the N-RNA genome template. Recent CryoEM studies showed N-RNA forms a left-handed helix that winds around a cavity, with the 3' end at the tapered end and the 5' end at the blunt end [38,43,80] (please see corrections to ref 5 for the correct RNA orientation). Like all other nonsegmented negative sense (NNS) RNA viruses, VSV packages multiple copies of a polymerase that consists of the L protein catalytic subunit (241 kD) and a template-binding P protein subunit (30 kD). The polymerases transcribe and replicate the N-RNA genome by engaging at promoter sites at or near the 3' end of the genome template [81].

On average ~50 L and ~400 P proteins are packaged within each virion [82]. The position of the L and P proteins within the bullet shaped virion has not been established previously. L organizes itself into a ring structure with an approximate diameter of 10 nm and does not bind the template by itself [83,84,85]. P proteins form dimers through their central domains and also bind L and the N-RNA template [84,86,87]. In recent CryoEM studies of VSV [38], either symmetry mismatches between the N-RNA helix, L and P, or random positioning of L and P, resulted in averaging out of the L and P

density within the central cavity of VSV. Therefore to resolve the position of L and P, single virion imaging techniques with sufficiently high resolution are required.

While the resolution of simultaneously imaged multiple fluorophores is limited by diffraction, the position of a single fluorescent molecule can be localized with nanometer precision. The precision of localization is inversely proportional to the square root of the number of photons collected from the single molecule [7]. It is therefore possible to reconstruct an image by successively photoactivating subsets of molecules that are further apart from each other than the diffraction limit and localizing their positions with nanometer precision. This principle was developed in photoactivatable localization microscopy (PALM, [88]) fluorescence photoactivatable localization microscopy (fPALM, [10]) and stochastic optical reconstruction microscopy (STORM, [11]) to achieve in plane resolutions of ~20nm. The axial resolution of these techniques can be extended either through introduction of astigmatism associated with the out of plane images [28] or using Biplane imaging [30] both of which report an axial resolution of ~50nm.

Although fluorescence is specific, it does not report the density of unlabeled protein molecules. Atomic force microscopy (AFM) is sensitive to the overall protein density, via changes in the mechanical properties of the sample: the protein density within an object can be probed by measuring the deformation of a sample in response to a force applied by the AFM cantilever.

AFM has been used in this way to measure the stiffness of single virions [18,73,89]. In general, viruses without an envelope are very stiff with a Young's modulus in the range of GPa [18] while the enveloped viruses can be an order of magnitude softer in the range of 100 MPa [73].

Since the N-RNA is packaged with specific orientation of its 5' end at the blunt end of the virion [38] and since the polymerases can only engage a promoter at the 3' end [90,91], positioning of the polymerases within the bullet will inform our understanding of the early transcription of the N-RNA genome immediately upon delivery to the host cytoplasm and to some extent the final moments of packaging the genome in budding virions.

2.5 Materials and Methods

2.5.1 Super-Resolution Imaging and Fluorescence Localization

Images were recorded with a SR 200 microscope (Vutara, Inc.) based on the Biplane approach [30]. The envelope of VSV virions was mapped by labeling ~75% of the VSV-G protein on the exterior of the virion with Alexa-Fluor®647 (Invitrogen A21245). Alexa fluorophores can be efficiently initialized to their dark state in imaging buffer [Appendix A] and can then be photo-activated through application of 405 nm UV light. This method was used to generate the viral envelopes shown in Figures. 2.1, 2.2.

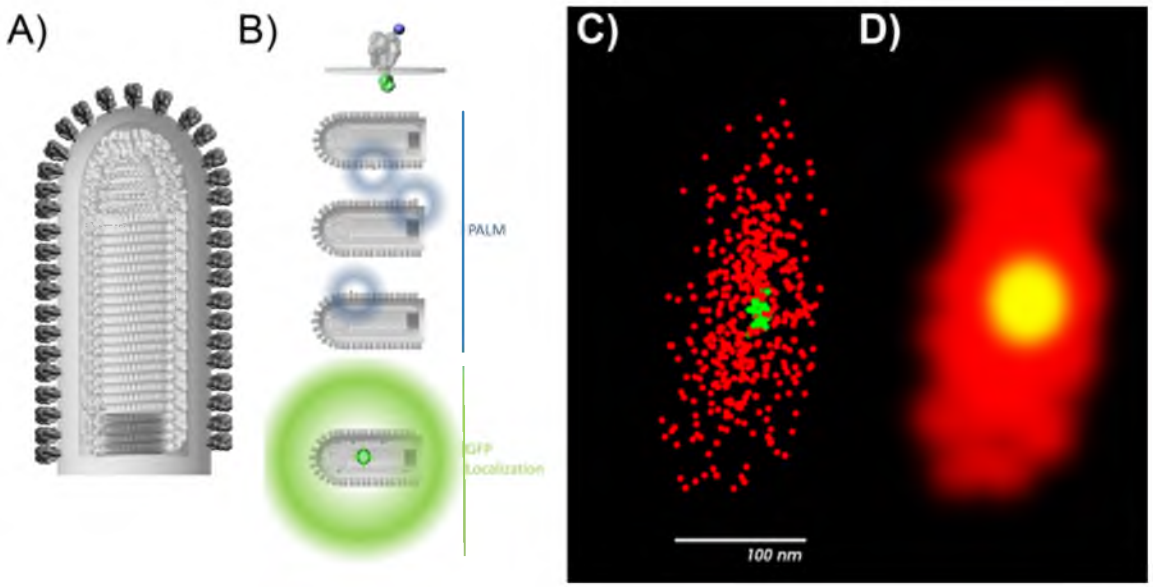

Figure 2.1: Locating eGFP center of fluorescence within reconstruction of VSV envelope. A) A model of VSV virion constructed partly from CryoEM data [38]. B) VSV-G is tagged from the exterior with Alexa 647 and internally with eGFP, ensuring that the eGFP center of fluorescence coincides with the center of the virion. C) Super-resolution fluorescence microscopy results in localization of VSV-G proteins (red) and location of the center of fluorescence of eGFP (green). D) Volumetric rendering of the VSV envelope from super-resolution fluorescence imaging data along with the location of the center of fluorescence of eGFP.

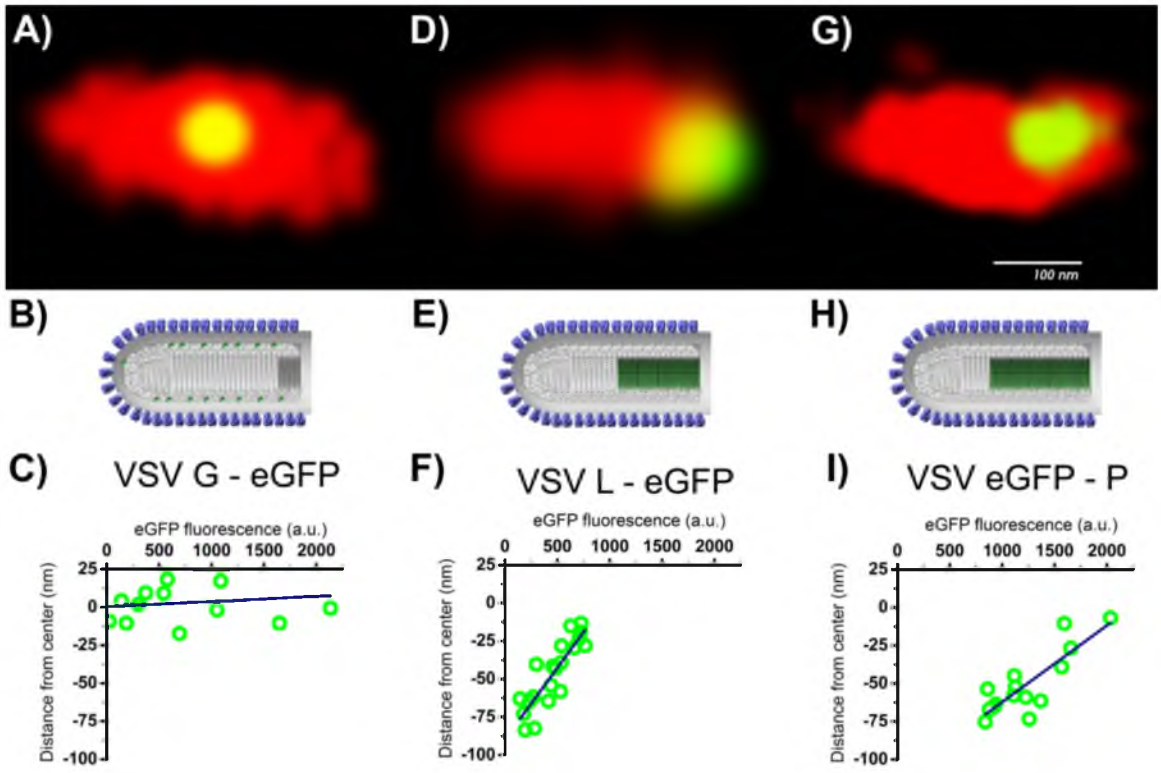

Figure 2.2: Center of fluorescence of the eGFP-linked proteins (G, P, and L, respectively A, D, and G). Images in the center (B,E, and H) show the model of the VSV constructed partly from CryoEM data [38] in comparison to representative volumetric rendering of virions (red) and G-eGFP, eGFP-P, and L-eGFP (green). The center of fluorescence of eGFP is shown in green. At the bottom (C, F, and I), the distributions of the center of fluorescence of the virions with respect to the amount of eGFP fluorescence detected from each virion shows packaging with a constant density.

To locate the internal proteins within individual virions, we used recombinant viruses encoding enhanced Green Fluorescent Protein (eGFP) linked to the viral proteins P or L. In these recombinant viruses, all of the P or L proteins are respectively replaced by P linked to eGFP (eGFP-P) or eGFP linked to L (L-eGFP) and these viruses have been previously characterized [92,93]. The center of mass of the eGFP labeled proteins was determined in each virion and its relative distance to the center of the high resolution envelope was measured. The eGFP proteins associated with these internal proteins were not photoswitched, rather their total fluorescence intensity and the position of their center of fluorescence with respect to the center of the envelope was determined.

Excitation and activation of single fluorescent molecules was achieved via a speckle-free illumination with an even intensity distribution, which was realized by a specialized beam homogenizer. Two color channels were detected sequentially at 50 frames/sec. eGFP data were collected first over 500 frames at 30% power (1.2kW/cm^2), then Alexa 647 was collected over 15,000 frames at 100% power (4kW/cm^2). Data analysis was performed using the Vutara SRX software (Version 4.01).

2.5.2 Validation of Super-Resolution Imaging Method

First we have validated the resolution of the Biplane microscope by imaging beads on the microscope for 1000 imaging frames with an average

fluorescence signal of 500 photons (comparable to our sample fluorescence). The analysis of these data, as shown in detail in Appendix A, shows that we can localize these beads with less than 10 nm precision in XY and 25 nm precision along the optical axis. Resolution of the microscope is defined by the full width half maximum analysis and is 20 nm in plane and 50 nm along the optical axis.

Since the VSV G proteins are uniformly distributed on the surface of the envelope, we used them for our control experiments. VSV virions were pseudotyped with eGFP linked to the C terminus of VSV G protein (Appendix A). Since virions are assembled on different cells within the population with varying levels of expression of VSV G-eGFP expression, the collected virions have a distribution of G-eGFP incorporation between virions. Each virion incorporates 1200 copies of G independent of whether the G has a GFP tag or not and G proteins are uniformly distributed on the surface of each virion [82]. We expect that the center of fluorescence of G-eGFP to colocalize with the center of the viral envelope independent of the number of G-eGFP proteins packaged on the surface of the virion. Because the virus is pseudotyped on a population of cells with varying expression levels of G-eGFP (Appendix A), we also expect that the amount of G-eGFP in each virion will vary. As Figures 2.1 and 2.2 (A-C) show, the G-eGFP center of fluorescence overlapped with the center of the virion to within ±11 nm, measured for 13 VSV:G-eGFP virions.

We also verified this method on HIV virions. HIV forms spherical virions with a diameter of 120-150 nm [48]. The membrane of these virions is coated internally with a lattice of Gag proteins as observed through CyoEM. The Gag lattice is uniformly distributed inside the virions with the exception of a few gaps [94], therefore we expect that the center of mass of Gag be very close to the center of the virion, if not exactly on the center of virions due to the possible empty patches. We verified our super-resolution fluorescence imaging method on HIV Virus Like Particles (VLPs) pseudotyped with VSV G which incorporated Gag-eGFP proteins (Appendix A). G proteins were labeled with Alexa 647 tagged antibodies to mark the envelope of the VLP and 12 HIV virions pseudotyped with G incorporating Gag-eGFP showed that the center of the virion colocalized with the center of the Gag signal to within 12 nm precision as shown in (Appendix A).

2.5.3 AFM Materials and Methods

We used Atomic Force Microscopy (AFM) for iso-force scans across the surface of several virions. The AFM (Asylum Research MFP-3D in a dark environmental chamber) consists of a pyramidal gold-coated tip (radius of curvature ≃20 nm; height ≃10 μm) attached to the underside of a pliable cantilever (force constant ≃3N/m ; length = 200 μm), a piezoelectrically actuated sample scanner (<1 nm precision), and associated digital control and data acquisition electronics. On stiff samples, the AFM cantilever bends

easily to accommodate changes in the sample height, so the path of the tip faithfully reports sample topography. When the sample is more pliant than the cantilever, the sample will deform under the force of the tip, so the height signal becomes more indicative of the sample's stiffness rather than its topography, therefore, the height signal provides an isoforce map of the sample surface rather than a true topographical map.

2.6 Results

2.6.1 Super-Resolution Fluorescence Imaging Shows P and L are Localized at the Blunt End of VSV

To measure the center of mass of P and L proteins within the virus, we used recombinant viruses encoding enhanced Green Fluorescent Protein (eGFP) linked to the viral proteins P or L. In these recombinant viruses, all of the P or L proteins are respectively replaced by P linked to eGFP (eGFP-P) or eGFP linked to L (L-eGFP) and these viruses have been previously characterized [92,93]. VSV: L-eGFP is temperature sensitive, replicates in 32C and packages 1/3 of the wild type levels of the polymerase L. VSV: GFP-P grows at 37°C to a lower titer than Wild Type (WT) and packages half the L and P proteins when compared to WT virus. These fluorescent viruses although imperfect, allow localization of their L and P. Later, we will examine the effect of protein density on localization by comparing these viruses to WT using AFM.

The total fluorescence intensity detected from the virions is directly proportional to the copy number of packaged eGFP linked proteins; however, it cannot be used as an absolute measure of the copy number due to fluorescence quenching at high concentrations. More importantly for this work, the center of fluorescence of the eGFP pinpoints the center of mass of the L or P protein distributions, which can be determined with ~10 nm precision [7].

For all 15 VSV:eGFP-P virions measured, the eGFP-P center of fluorescence was located toward the blunt end of the virion. We observed a 30% variation in the total fluorescence between individual virions of VSV:eGFP-P, which represents variations in the number of P-eGFP packaged. The average fluorescence signal for 15 virions was 1233 ± 351 photons. As shown in Figure 2.2D, virions with fewer eGFP-P copies showed the largest displacement of the eGFP localization with respect to the center of the virion, while virions with the maximum number of eGFP-P copies had almost no displacement. The linear relationship between the displacement and the number of packaged eGFP-P molecules shown in Figure 2.2D indicates a constant packing density of P proteins as they fill the cavity starting from the blunt end. In average the center of mass of the P-eGFP was displaced from the center of the virion by a distance of 50 ± 21 nm.

Because P proteins associate with L, we next measured the distribution of L. We also found variation in the fluorescence signal between individual

VSV:L-eGFP virions of 461 ± 202 photons. Furthermore, as with the eGFP-P, we observed a linear relationship between the L-eGFP fluorescence intensity and the displacement of the fluorescence center from the virus center as shown in Figure 2.2F. Again, this indicates uniform packaging of L-eGFP proteins at the blunt end of the virus. The average center of fluorescence for 20 VSV:L-eGFP virions was located 46 ± 22 nm from the geometric center of the virus toward the blunt end. We conclude that P and L package asymmetrically the same volume at the blunt end of VSV.

Note that neither VSV:eGFP-P nor VSV:L-eGFP package wild type levels of L and P (see 2.6.2), so the fluorescent measurements cannot be used to estimate either the density or the exact length of the volume in which L and P package in wild type virions.

2.6.2 AFM Reveals Protein Density at the Blunt End of VSV

We next used a fluorescence-free assay both to corroborate the above results and to estimate the size of the volume occupied by L and P proteins within wild type virions. Any variation in the protein density along the length of a virus particle should lead to a change in its mechanical properties, specifically its stiffness. Stiffness of the envelopes viruses [73] is almost an order of magnitude less than viruses without envelopes like bacteriophage [18] or adenovirus [17]. The proteins associated with the envelope of VSV

(G, M and N) have a symmetric helical organization [38], therefore, the AFM tip can deform the envelope and probe the stiffness of the underlying structure which should have no variance along the central axis of the virus. Internal proteins and genomic structure of the viruses have direct effects on their mechanical properties, as shown previously for DNA binding within the capsid of parvovirus of mice [19] and maturation of HIV virions [73,95]. We hypothesized that the virus should be stiffer at the blunt end due to the presence of an over density of P and L proteins there. Using a relatively stiff cantilever with tapping-mode AFM under ambient conditions, we performed an iso-force scan of the virions tethered on glass surfaces as explained in the methods. The stiffness measurements rely on using the AFM probe as a force sensor. In particular for soft samples, the probe depresses the surface, and the degree of depression is related to the stiffness of the sample relative to the spring constant of the AFM cantilever (Appendix A). We were able to press considerably into the virus and detected an increase in the height of the virus at the blunt end. Since the scans are iso-force, the increase in height indicates an increase in stiffness from extra protein density at the blunt end. AFM was able to resolve the asymmetric bullet shape of the virions, thus placing the region of elevated stiffness at the blunt end (Figure 2.3 and Appendix A).

As shown in Figure 2.3, we observed virions with 180×80nm bullet shapes, each with recognizable tapered and blunt ends distinguished by analyzing

Figure 2.3: AFM surfaces of VSV. These show two distinct regions with respect to structural composition, specifically a variation in elastic response to the force exerted by the tip. A) Wild type VSV virions have the stiffest bump region, indicated by the tallest bump. B) The ratio of the two regions' respective heights (h' for the bump, h for the main body) is 1.14 ± 0.07 for 50 WT virions. C) A representative VSV:eGFP-P virion with a similarly distinctive bump. D) VSV:eGFP-P h'/h is 1.07 ± 0.06 for 30 virions. E) VSV:L-eGFP virions have little or no distinguishable regions towards the rear, and F) have a measured h'/h of 1.02 ± 0.01 for 30 virions. *Indicates the representative virions.

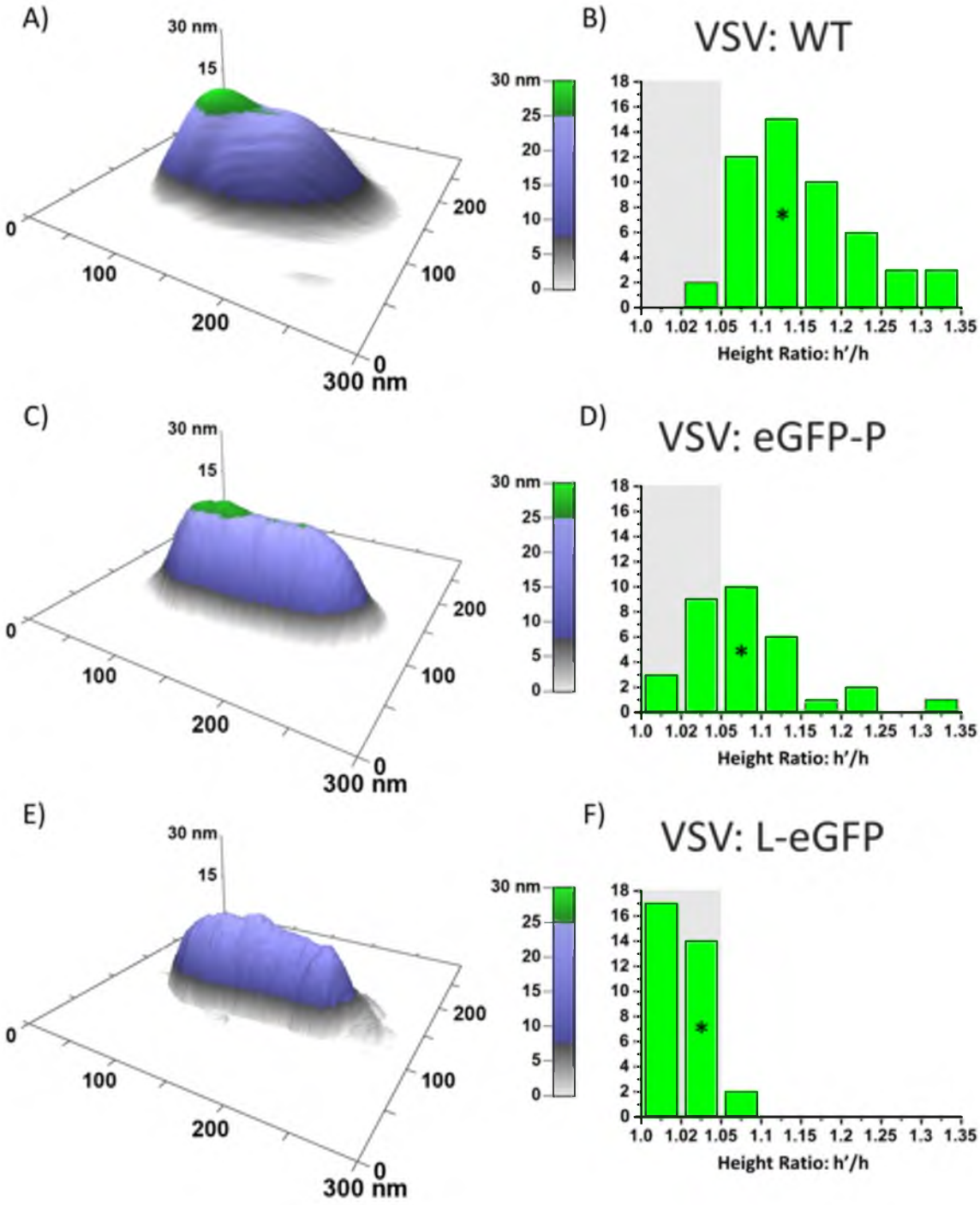
A)
30 nm
15
0
100
200
0
100
200
300 nm
B)
VSV: WT
30 nm
25
20
15
10
5
0
18
16
14
12
10
8
6
4
2
0
1.0 1.02 1.05 1.1 1.15 1.2 1.25 1.3 1.35
Height Ratio: h'/h
C)
30 nm
15
0
100
200
0
100
200
300 nm
D)
VSV: eGFP-P
30 nm
25
20
15
10
5
0
18
16
14
12
10
8
6
4
2
0
1.0 1.02 1.05 1.1 1.15 1.2 1.25 1.3 1.35
Height Ratio: h'/h
E)
30 nm
15
0
100
200
0
100
200
300 nm
F)
VSV: L-eGFP
30 nm
25
20
15
10
5
0
18
16
14
12
10
8
6
4
2
0
1.0 1.02 1.05 1.1 1.15 1.2 1.25 1.3 1.35
Height Ratio: h'/h

the AFM cross sections (Appendix A). During AFM scans, the tip locally compresses the virions to a height of~30 nm due to deformation of the soft viral envelope, but the measured widths (~100 nm) accurately reflect the true diameter of the virions with a 20 nm convolution. This demonstrates that the virions were not "pancaked" onto the substrate due to surface interactions or dehydration. This was confirmed by increasing the force and pushing the virus into the non-elastic region which resulted in fully deformed virions (data not shown).

For all wild type virions measured, there was a region at the blunt end that exhibited less depression (higher stiffness) compared to the rest of the virus, as shown in green. This region extended 57 ± 12 nm in length from the blunt end, obtained from a sample of 50 wild type viruses.

2.6.3 Detected Density at the Blunt End of the Virus Correlates with the Amount of P and L Packaged

Recombinant VSV:eGFP-P viruses exhibit slower than wild type growth kinetics and package about half the number of P and L proteins compared to the wild type. Their bullet-shaped morphology is, however, indistinguishable from the wild type when viewed in EM [92,96]. For 30 VSV:eGFP-P virions, the region of higher stiffness extended 68 ± 21 nm, but the magnitude of elevated stiffness was much lower compared to wild type, as shown in Figure 2.3. These results suggest that VSV:eGFP-P forms a protein complex of lower

density compared to the wild type. A GFP-labeled P cannot package as densely as wild type because eGFP likely sterically hinders packaging. This may explain why the eGFP-P virions have a volume with lower stiffness than wild type that nonetheless extends significantly within the cavity.

VSV:L-eGFP viruses are only partially functional, package only about a third as much L as wild type (but normal amounts of P), and do not transcribe their RNA in vitro. They do, however, replicate well at 32°C and form VSV virions with the correct morphology [93]. Increased stiffness at the blunt end of VSV:L-eGFP was almost undetectable via AFM, consistent with a much lower density volume of polymerase complexes compared to wild type.

2.7 Discussion

Using high-resolution fluorescence imaging and center of mass calculations on recombinant viruses in which all wild type L or P proteins were genetically replaced with GFP linked fusion proteins of L and P, we show asymmetric packaging of the polymerase complex of VSV at its blunt end. L and P packaged within the blunt end of the virus create a region of higher stiffness within the blunt end of the virus. We measured this region of higher stiffness using AFM and in WT virions report its average length at 57 nm with a variation of ± 12 nm among virions. This variation reflects the variable number of L and P packaged in each virion as also measured with fluorescence and shown in Figure 2.2.

The present study has focused on identifying the position of the polymerases within the cavity of VSV, which resulted in identifying the asymmetric distribution of polymerases at the blunt end of the virus. Transcription of the virion N-RNA is the first step required for virus multiplication after entry into the host cytosol, and this can only initiate at or near the 3' end [90,91]. Recent CryoEM studies showed the N-RNA winds around a cavity in a left-handed helix, starting with its 3' end at the virus's tapered end and culminating with the 5' end at the blunt end of the virus [38,43]. Based on our observations, the polymerases are therefore stacked at the 5' end of the genome rather than at the 3' end where the transcriptional promoter is located. We envision two ways in which the polymerase units can reach the 3' transcriptional promoter. In the first model, we hypothesize it would be possible to start transcription through formation of an N-RNA template loop that brings the 3' end of the genome close to the 5' end of the N-RNA where the polymerases are located. Such N-RNA loops have been identified in the cytoplasm of cells infected with VSV before [39]. The observed asymmetry of the polymerase localization along the genome however cannot rule out the traditional model of transcription in which L-P_x complexes dissociate from the N-RNA and re-engage the promoter at the 3' end.

2.8 Acknowledgements

We thank Prof. Stephen Harrison for fruitful discussions and comments in preparation of this manuscript. We thank Jeff Ballew for providing support and technical assistant. This work was supported by NSF grants 1121972 (SS) and DBI-0845193 (JMG).

2.9 Chapter Conclusion

Since this paper was authored and submitted for publication, the techniques discussed have been refined in order to allow for a superior recovery of both viral envelope and protein location within a VSV virion. The improved viral envelope recovery is discussed in Chapter 4, and consists of immunolabeling of the virion in solution prior to adhesion to the glass surface. This technique has the advantage of improving envelope coating with the fluorescent label while decreasing nonspecific labeling which is seen as noise in the assay. Additionally, the Saffarian lab has developed VSV proteins labeled with photo-switchable labels in order to utilize the full advantages of the STORM/PALM technique. It is hoped at the time of this writing that future work with these improvements will illuminate the protein configuration within the central cavity further and possibly allow for the counting of individual proteins of interest.

CHAPTER 3

PROTON PERMEABILITY OF HIV VIRUS-LIKE PARTICLES AND VESICULAR STOMATITIS VIRUS

Jeffery Hodges[1,2*], Pei-I Ku [1,2,*], Michael L. Landesman[1,2], Peter Williams[1,2], Xiaolin Tang[1,2], and Saveez Saffarian [1,2,3,#]

1 Department of Physics and Astronomy, University of Utah
2 Center for Cell and Genome Science, University of Utah
3 Department of Biology, University of Utah
* Equal Contribution
Correspondence to: Saffarian@physics.utah.edu

3.1 Chapter Introduction

As discussed in Chapter 1, this chapter contains a paper that is in the process of being written for publication during the time this dissertation is being written. The paper recognizes a difference in permeation rates between immature and mature HIV-1 VLPs. The cause for this variance is the difference in protein configuration at the lipid envelope. This essentially challenges a prevailing notion that envelope viruses are impermeable [54,97] in the short term to pH permeation. This notion exists independent of significant research showing that liposomes, whose envelopes are very similar to viral envelopes, are permeable [98].

By utilizing the pH sensitive fluorophore ecliptic pHluorin, the bulk pH of HIV-1 VLPs were measured over time in order to determine the permeation characteristics of the envelopes. This permeation is a two stage event in which transient pores initially allow for a rapid exchange of protons followed by a slower diffusion period where protons diffuse into the system.

Beginning at pH 7.2, the external environment of VLP's was rapidly exchanged with a lower pH (6.2) and the fluorescence of the VLPs was watched. On average, the majority of VLPs demonstrated a significant decrease in fluorescence over time (on the order of 5 minutes), indicating short term permeation of the envelope. In some cases it was determined that the envelope of the VLP had been compromised in some manner prior to the pH change, and fluorescence quenching to the new pH 6.2 intensity took only

a few seconds. In a few cases, the envelope was observed to compromise during the process and quenching to the pH 6.2 was finished in only a few seconds. These results indicate that while the lipid envelope does act as a barrier to instantaneous pH response, it is not impermeable. Additionally, the observed difference in permeation characteristics between immature VLPs, which have a higher concentration of proteins associated with the envelope, and mature VLPs, which have a lower concentration of proteins associated with the envelope, showed that envelope protein concentration plays a significant role in the rate of diffusion of protons into the envelope.

3.2 Abstract

Enveloped viruses have been assumed to be impermeable to protons around natural pH. While some enveloped viruses like HIV fuse at the plasma membrane and do not enter low pH environments, some viruses like Vesicular Stomatitis Virus (VSV) fuse at the endosomes under low pH environments. In viruses that enter through low pH environments, regulation of the internal pH is critical for proper delivery of their genome to the host cell. Here, we report the permeability of bald as well as VSV-G pseudotyped HIV virus like particles (VLPs) in their mature and immature states as well as wild type vesicular stomatitis virus virions. Permeability was measured on single isolated virions/VLPs. The virions/VLPs incorporated multiple copies of a pH sensitive GFP variant (pHluorin) whose fluorescence

depended on its protonation state with a pKa of 7.18. Permeability was measured by the change in fluorescence as the external pH was lowered from neutral to 6.2. We found all HIV VLPs and VSV virions to be permeable to protons, with fast permeation due to transient nanopore formation at the initial phase followed by the diffusion of protons across the membrane. Maturation of the HIV VLPs increased the permeation rate by a factor of two suggesting the Gag lattice lowers the permeability of immature VLPs. The average permeation rate of the VSV virions as well as HIV VLPs was similar to the previously measured rate for 150 nm lipid vesicles and all virions equilibrated to the outside pH well below 10 minutes. Our data suggest that permeation of envelopes within VSV virions and HIV VLPs is governed through the same permeation mechanism as lipid vesicles with similar sizes and none of the virions/VLPs in this study are impermeable, at least if given sufficient time.

3.3 Introduction

Lipid bilayers have a hydrophobic core sandwiched between two layers of charged hydrophilic head groups. The hydrophobic core might appear impermeable to protons, but protons can transit this region via two distinct mechanisms. First, upon application of a pH gradient across the bilayer, transient hydrated pores permit rapid permeation of protons on a picosecond timescale. Second, a solubility-diffusion mechanism operates on a time scale

of hundreds of seconds [99,100]. This biphasic mechanism of proton permeation is seen in lipid vesicles (d = 150 nm) encapsulating pH sensitive dyes [98].

The development of pH sensitive green fluorescent protein (GFP) variants (pHluorins [70,101]) allows the measurement of pH within small biological structures. In the case of multivesicular bodies (MVB), the lumen of the internal vesicles (d = 40nm) was thought to be protected from acidification until fusion with the vacuole. Using pHluorin, acidification of these vesicles is observed prior to fusion, indicating that the bilayers of MVB vesicles are permeable to protons [71]. Synaptic vesicles (d = 40 nm) are similar in size; however, to function they must maintain a pH gradient [70,101]. To work against the diffusive forces that would otherwise equilibrate the pH, synaptic vesicles incorporate a vacuolar H^+ ATPase [102].

How do enveloped viruses (d = 100-300 nm) regulate their permeability to protons given that their lipid envelopes are bent and their life cycle can carry them through extremely variable pH environments? A classic example is influenza virus, whose envelope is assumed to be impermeable to protons around neutral pH. As influenza virions pass through the endosome, acidification of the virus interior is required to release genetic material into the cytoplasm. Viral M2 proton channels facilitate this acidification and are required for efficient replication [53,54]. Here, we examine two enveloped viruses that differ in their route of entry to the cell. One of them (HIV) fuses

at the plasma membrane and does not travel through low pH environments while the other one, Vesicular Stomatitis Virus (VSV), is endocytosed and fuses within with the endosomal membrane under low pH.

VSV enters cells via endocytosis and fuses with the inner leaflet of the endosomes to release its genome into the cytoplasm. There are no previous data on the permeability of VSV around neutral pH. Unlike influenza, VSV does not incorporate any known proton channels, however, glycoprotein of VSV (VSV-G) are shown to permeate protons below pH 6 [82]. VSV is a bullet shaped rhabdovirus. The bullet-shape appearance of the virion results from tightly wound helical turns of the nucleoprotein encapsidated RNA template (N-RNA) around a central cavity. The matrix protein forms a helical structure along the inner leaflet of the lipid bilayer, in effect connecting the N-RNA to the inner leaflet of the viral envelope. This binding pattern gives VSV its rigidity and bullet-like shape [38]. It is reported that (VSV-G) dependent acidification of the interior of the virion below pH 6 helps with dissociation of the matrix protein before N-RNA is released into the host cytosol [103].

Approximately 1200 copies of VSV-G decorate the surface envelope of the VSV virion and have three conformational states: the native state detected at pH 7 and above, the activated hydrophobic state which interacts with the target membrane during fusion and the inactive postfusion form [104]. Unlike class I fusion proteins, VSV-G is in equilibrium between the three

conformational states. It is believed that this property is critical to allow the VSV-G to fold back correctly after passing through the Golgi apparatus en route to the plasma membrane after synthesis [105]. The optimum pH for VSV-G fusion is pH 6. The conformational changes of the VSV-G protein down to pH 6 are all within the ectodomain and do not affect the permeability of the underlying membrane. The G protein has pore formation properties below pH 6 [103,105,106]. How the VSV virion permeate protons around neutral pH is critical for understanding the VSV-G independent acidification of the virions.

HIV fuses at the plasma membrane of its host and therefore does not enter low pH environments like influenza and does not incorporate proton channels. Bald HIV VLPs have previously been assumed to be impermeable to protons around neutral pH [107]. HIV Gag is sufficient to create fully formed VLPs with an average diameter of 130 nm that bud into the extracellular space similar to the full virus [108]. VLPs will also assemble from a mixture of Gag and Gag-fused to GFP variants with identical kinetics and size distributions [107,109].

HIV Gag consists of three folded domains (MA, CA, and NC) and binds to the plasma membrane through insertion of a myristoyl group into the bilayer and interactions with the MA domain. HIV also produces a smaller population of Gag-Pol protein, encoding a protease that binds the plasma membrane in a similar fashion. In an immature virion, Gag forms an

incomplete lattice with hexagonal geometry on the inner leaflet of the envelope [110,111]. After release of the virus into the extracellular space, maturation occurs, during which the protease cleaves Gag at specific sites, allowing NC proteins to condense around the RNA-genome and CA proteins to self-assemble into a conical capsid around the NC-RNA complex (reviewed in [48]). Permeability of HIV VLPs is not well understood around neutral pH.

Here, we examine the permeability of HIV VLPs and VSV close to the neutral pH. The HIV VLPs in this study either have no glycoproteins (bald) and/or are pseudotyped with VSV-G. Super ecliptic pHluorin (SEpH) [101] with a pKa of 7.18 allows the measurement of permeability well above pH activated permeability mediated by VSV-G. While proton permeation at low pH is relatively understood to be driven through protein channels such as the M2 or VSV-G, the envelopes above pH 6 were assumed to be impermeable. Understanding the base rate of permeability of the envelopes around neutral pH will allow us to refine the role of the protein channels within these enveloped viruses. Measurements of permeability on single VLP/virions will also allow characterization of potential envelope failures due to entrance into a low pH environment. Envelope failure poses a great risk to virions which have to travel to low pH environments.

3.4 Materials and Methods

3.4.1. Preparation of Immature, Mature, Bald, and VSV-G Pseudotyped HIV Virions

Immature VLPs were prepared by transfection of 293T cells with Gag, Gag-SEpH and VSV-G plasmids. Maturation competent VLPs were prepared by transfection of 293T cells with pCMVΔR8.2 [112], Gag-SEpH, and VSV-G. Immature bald VLPs were prepared by transfection of 293T cells with Gag and Gag-SEpH plasmids. Cell medium was harvested 24 hours post-transfection, filtered and purified through a 20% sucrose cushion. Purified VLPs pseudotyped with VSV-G were applied to glass coverslips coated with layers of biotinylated-PEG, NeutrAvidin, and biotinylated-antibody to VSV-G. Purified bald VLPs were absorbed to glass coated with Poly-L-Lysine.

3.4.2 Preparation of Pseudotyped VSV Virions

Pseudotyped VSV virions were prepared by transfection of BHK cells with VSV-G-SEpH plasmid using Lipofectamine 2000. At 24 hours post-transfection, cells were incubated with VSV wild type of MOI 3 for 1 hour and then changed to a fresh DMEM medium. At 24 hours postinfection with VSV, medium was harvested and filtered with 0.22 µm membrane. Filtered medium was concentrated down by centrifuging in Thermo Scientific fiberlite f21s-8×50 rotor at ~40,000×g for 90min @ 4°C. Supernatant was removed and virus pellet was resuspended overnight in ~400µl NTE (10 mM Tris pH 7.4

100mM NaCl 66mM EDTA) at 4°C. The sample was then purified through a 10% sucrose cushion in NTE for 1hr @ ~160,000×g. The pellet was resuspended in NTE slowly overnight at 4°C. After purification through 15%-45% gradient sucrose in NTE at ~80,000×g for 3.5hr a clear virus band was extracted and then purified through 10% sucrose cushion as described above. Pseudotyped VSV virions were resuspended in NTE with 10mM HEPEs and stored in an -80°C freezer. Virions were then applied to glass coverslips coated with layers of biotinylated-PEG, NeutrAvidin, and biotinylated-antibody to VSV-G.

3.4.3 Imaging Apparatus

We utilized a Focht Chamber System 2 (FCS2, Bioptechs Inc., USA) flow chamber with a 10 second fluid exchange mounted on an iMIC digital microscope equipped with a Yanus scan head and Polytrope II beam conditioner (Till Photonics, Germany). The HIV VLP and VSV fluorescence were excited using 488 nm excitation in TIRF mode with a penetration depth of 100 nm. The back reflected light from the sample during TIRF was used to clamp the focus of the objective on the sample during buffer changes (TIRF Clamp). We measured the permeability of individual VLPs and virions by measuring their total fluorescence intensity every 2 seconds for HIV and every 4 seconds for VSV as the buffer was rapidly changed.

3.4.4 Data Analysis

We utilized open VLPs and virions in order to more precisely calculate the pH of the surrounding environment. Upon changing of the buffer solution, a small amount of residual solution may be left over from the original buffer, causing the final surrounding pH to be higher than that of the pH 6.2. By measuring the final intensity of open VLPs and virions, we calculated a more accurate value for the final pH. These open VLP/virion traces are shown in red in Figures 3.1 and 3.2.

We modeled the quenching profiles of the closed VLPs and virions by the following two exponential decay functions:

$$[H^+](t) = [H^+]_{end} + [H]_p \cdot e^{-k_p t} + [H^+]_d \cdot e^{-k_d t} \tag{3.1}$$

The fast rate constant (k_p) represents the flow of protons through transient pores, governing the short-term quenching behavior, while the slow rate constant (k_d) represents diffusion across the envelope, governing the long-term quenching behavior. This function was previously used to measure the permeability of 150 nm lipid vesicles [98]. We converted the fluorescence data to represent $[H^+]$ using the equation:

$$[H^+](t) = 10^{-\left(7.18 - log\left(\frac{1+10^{7.18-7.10}}{F_n(t)} - 1\right)\right)} \tag{3.2}$$

where 7.18 is the pKa of SEpH [101], pH_{init} is the pH before the quench, and $F_n(t)$ is the normalized fluorescence intensity.

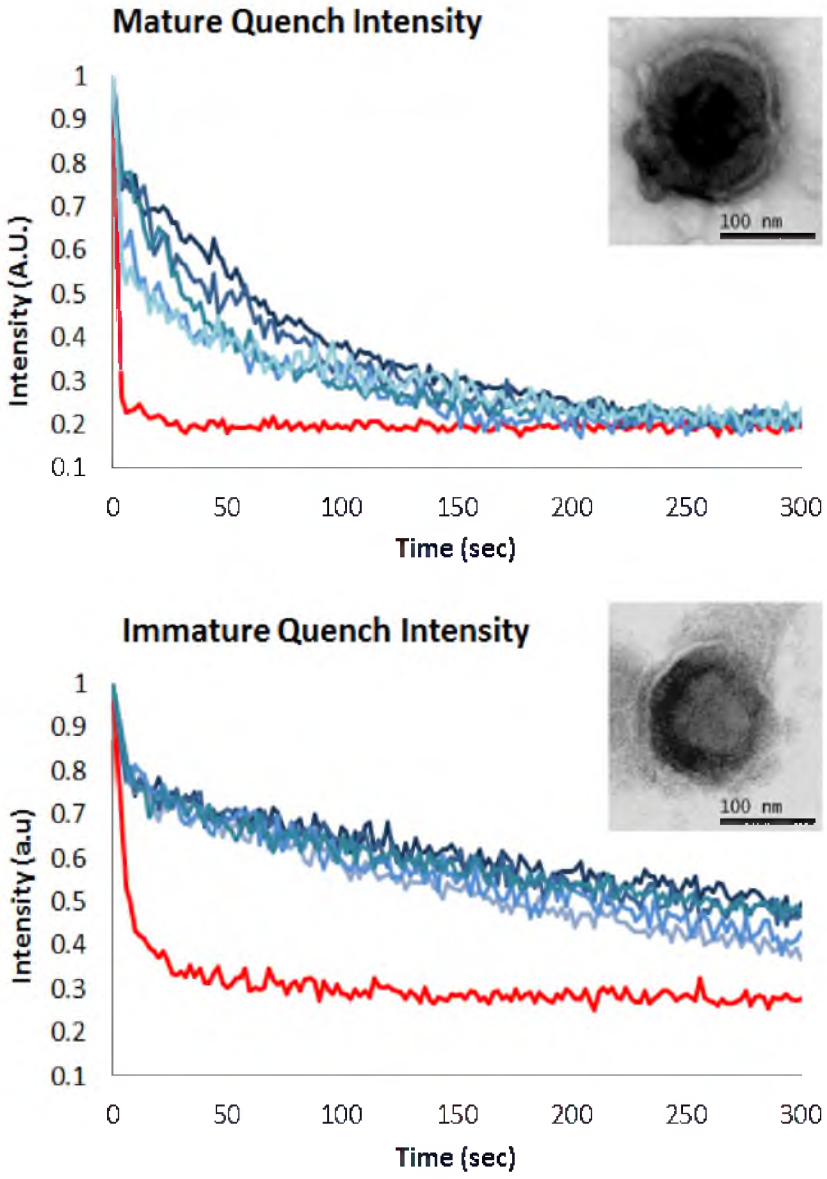

Figure 3.1 The intensity profiles of six mature and six immature VLPs during a quench. Representative TEM images of VLPs are inset with 100 nm scale bars. Blue curves show typical VLP quenching behavior, while red curves illustrate compromised envelopes.

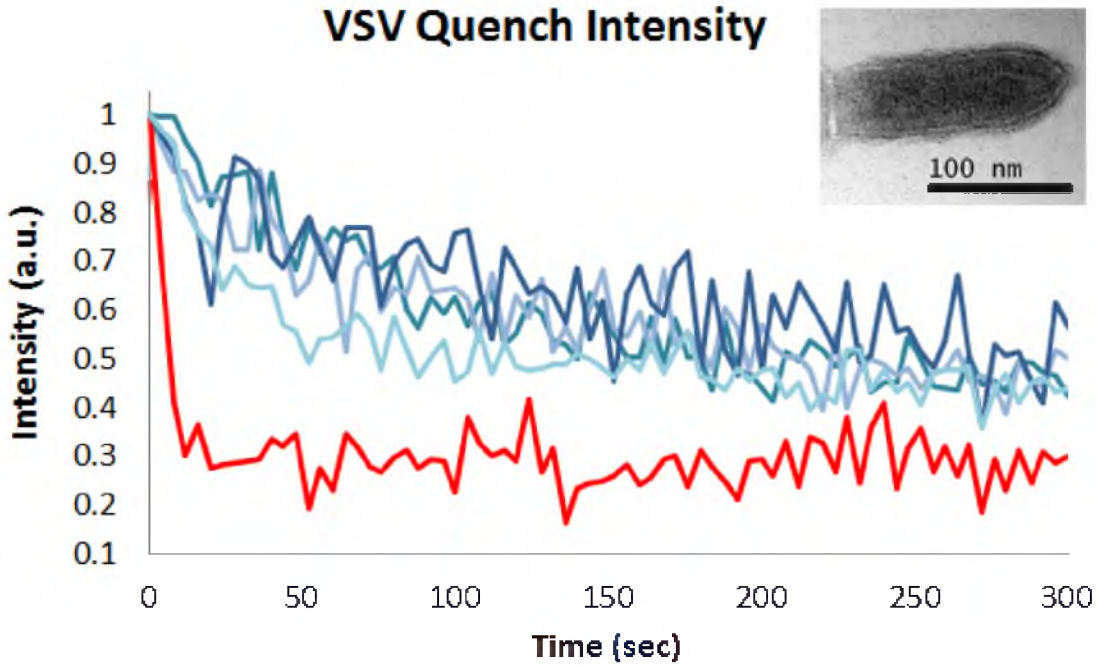

Figure 3.2 The intensity profiles of five VSV VLPs during a quench. A representative TEM image of a VLP is inset with a 100 nm scale bar. Blue curves show typical VLP quenching behavior, while the red curve illustrates a compromised envelope.

The rate constants (k_p and k_d) are related to the permeation of the envelope by the equation $P = k(R/3)$, where R is the radius of the vesicle [98]. Due to its bullet shape, we use the slightly modified equation $P = k(5R/12)$ to find the envelope permeation in VSV.

3.5 Results

Bald HIV VLPs deposited on glass are permeable to protons: In our initial experiments, we observed HIV VLP formation in live HeLa cells, transiently transfected with a mixture of HIV Gag and Gag-SEpH. Cells were plated on coverslips coated with layers of biotinylated-PEG, NeutrAvidin and biotinylated-fibronectin. Once VLP assembly was complete, the cells were washed away from the coverslip by application of flow, while the newly formed VLPs were retained on the coverslip. Upon changing the buffer (30 mM HEPES, 15 mM MES, 119 mM NaCl, 2.5 mM KCl, 2 mM $CaCl_2$, 2 mM $MgCl_2$, 01% PEG 8000) from pH 7.4 to 6.4, the total fluorescence of these VLPs dropped a relative 72% (Figure 3.3). This result was consistent with the characterization of the pKa curve of SEpH [101], in which this pH change would result in a fluorescence drop of 77%. This drop in fluorescence demonstrates that VLPs formed only from HIV Gag and Gag-SEpH are permeable to protons.

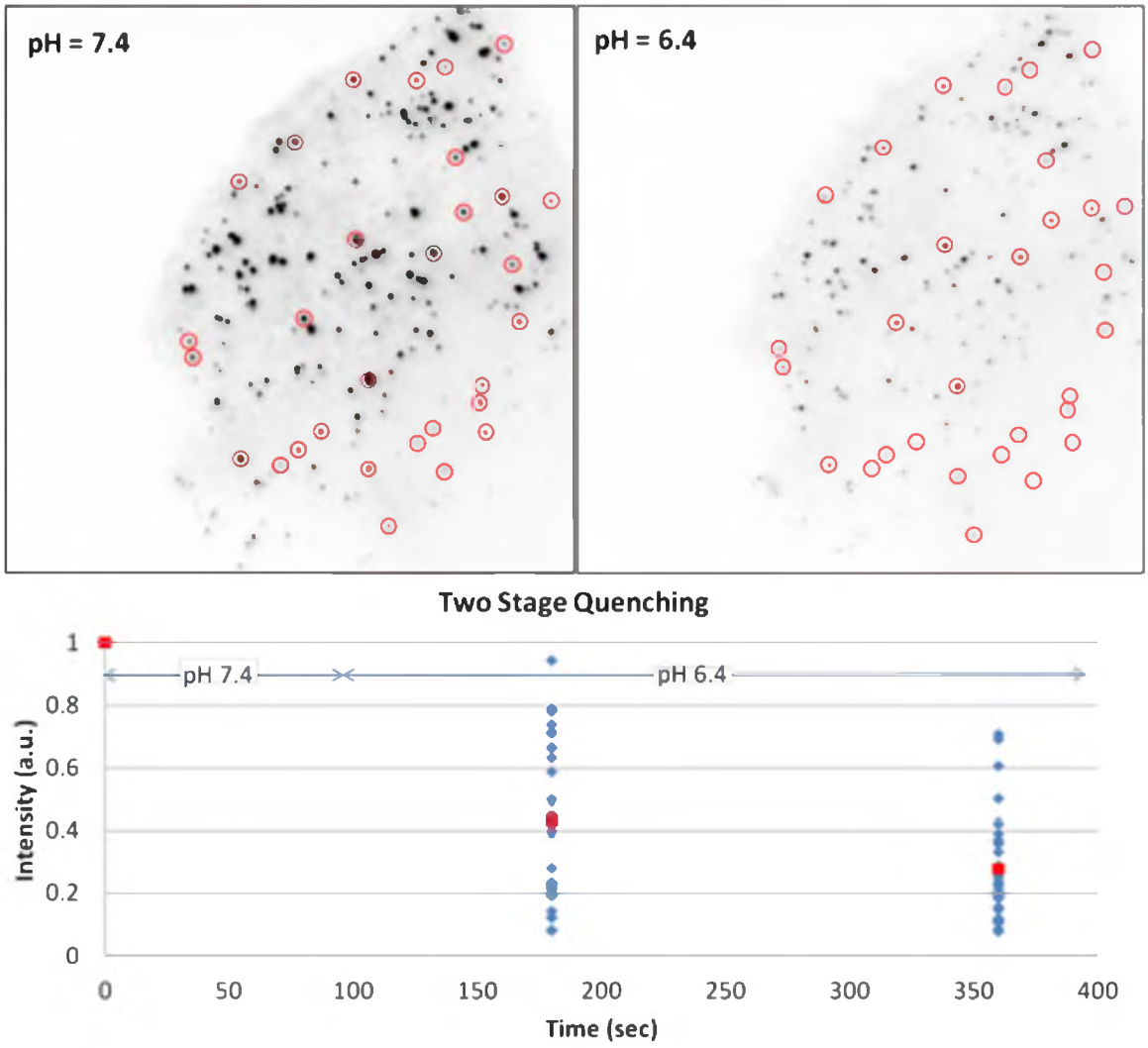

Figure 3.3 The intensities of 30 HIV VLPs (circled in top images) in pH buffers of 7.4 and 6.4. Red data points show the average fluorescence intensity of the VLPs at specific time points.

3.5.1 Measurements of Permeability in Single HIV Virions

VSV-G pseudotyped mature and immature HIV virions: To accurately measure the behavior of individual VLPs, we isolated mature as well as immature HIV VLPs pseudotyped with a transmembrane anchor, VSV-G from 293 cells as described previously in the methods section. These VLPs were tethered to the glass surface using a PEG-Biotin_Avidin-anti VSV-G sandwich as explained in the methods section and were exposed to a change of pH at the beginning of the experiments. In both mature and immature HIV VLP samples, ~40% of VLPs exhibited a near instantaneous response to the pH change, returning a fluorescence intensity consistent with 6.2 in less than 6 seconds (Figure 3.1, red curves). We believe that the envelopes of these VLPs are compromised and behave as if open to the external environment. We measured 47 mature VLPs and 71 immature VLPs in which the envelope remained intact (Figure 3.1, blue curves), which we will term "closed." When these VLPs were subjected to pH 6.2, a rapid fluorescence quench step followed by a slower quench step was observed. As demonstrated in the graphs, VLPs did not always quench to the base level predicted by the Henderson–Hasselbach equation when observed for 300 seconds. This is particularly true for immature HIV where VLPs quenched to only ~50% of their original intensity in the 300 second time frame shown. When observed

for longer time scales (10 min) however, both mature and immature VLPs quenched to predicted levels (data not shown).

Figure 3.1 shows the permeation of mature and immature HIV VLPs pseudotyped with VSV-G. Average mature HIV VLPs had $k_p^{mat} = 9.4\times10^{-2} \pm 2.8\times10^{-2}$ and $k_d^{mat} = 5.8\times10^{-3} \pm 2.4\times10^{-3}$, which result in first and second stage permeations of $P_p^{mat} = 2.7\times10^{-7} \pm 7.8\times10^{-8}$ cm/s and $P_d^{mat} = 1.7\times10^{-8} \pm 7.0\times10^{-9}$ cm/s. The average immature HIV VLPs had $k_p^{im} = 6.0\times10^{-2} \pm 0.7\times10^{-2}$ and $k_d^{im} = 3.4\times10^{-3} \pm 1.4\times10^{-3}$, which result in permeations of $P_p^{im} = 1.4\times10^{-7} \pm 1.6\times10^{-8}$ cm/s and $P_d^{im} = 7.9\times10^{-9} \pm 3.2\times10^{-9}$ cm/s.

Bald immature HIV virions were utilized as a control to measure the permeation of immature HIV VLPs immobilized onto a Poly L coated glass surface. The closed VLPs had permeations of $P_p^{im\ bald} = 1.3\times10^{-7} \pm 6.3\times10^{-8}$ cm/s and $P_d^{im\ bald} = 2.3\times10^{-8} \pm 1.1\times10^{-8}$ cm/s, which is comparable to the VSV-G pseudotyped virions; therefore, the presence of VSV-G dose not significantly alter the proton permeability of these VLPs.

For comparison the permeation rates of 150 nm lipid vesicles has been reported as $P_p^{\text{vesicles}} = 2\times10^{-7} \pm 3\times10^{-8}$ cm/s and $P_d^{vesicles} = 1\times10^{-8} \pm 4\times10^{-9}$ cm/s [98].

3.5.2 Measurements of Permeability of VSV Virions

Similar to HIV VLPs, ~35% of VSV virions showed quenching behavior, as if they were open to the environment, exhibiting a near instantaneous

response to the pH change (Figure 3.2, red curve). We measured 34 closed VSV virions in which the envelopes remained intact (Figure 3.2, blue curves). This subpopulation showed the same rapid fluorescence quench step followed by a slower quench step as seen with the HIV VLPs. As with immature HIV VLPs, not all VSV virions quenched to the predicted base level in 300 seconds. Again, though, they did reach this level when observed for longer time scales.

Due to its bullet shape, we use the slightly modified equation $P = k(5R/12)$ to find the envelope permeation in VSV. Average VSV virions had k_p^{vsv} = $1.1\times10^{-1} \pm 7.0\times10^{-2}$ and $k_d^{vsv} = 2.4\times10^{-3} \pm 1.8\times10^{-3}$, resulting in permeations of $P_p^{vsv} = 1.9\times10^{-7} \pm 1.2\times10^{-7}$ cm/s and $P_d^{vsv} = 4.1\times10^{-9} \pm 3.1\times10^{-9}$ cm/s.

Visually comparing Figures 3.1 and 3.2, VSV appears to follow a quenching behavior similar to that of immature HIV. In both immature HIV and VSV, the closed VLPs and virions quenched to approximately 50% of their original intensity after 300 seconds had lapsed. The closed mature HIV VLPs, on the other hand, nearly all quenched to the level predicted by the Henderson-Hasselbach equation in the same amount of time.

We observed catastrophic failure of several envelopes. Unlike VLPs that exhibit an instantaneous response to the pH change or those that follow the two stage quenching behavior, we observed some that exhibit a combination of the two behaviors (Figure 3.4, red line). We believe that these were VLPs whose envelopes started off intact and then ruptured during the quench.

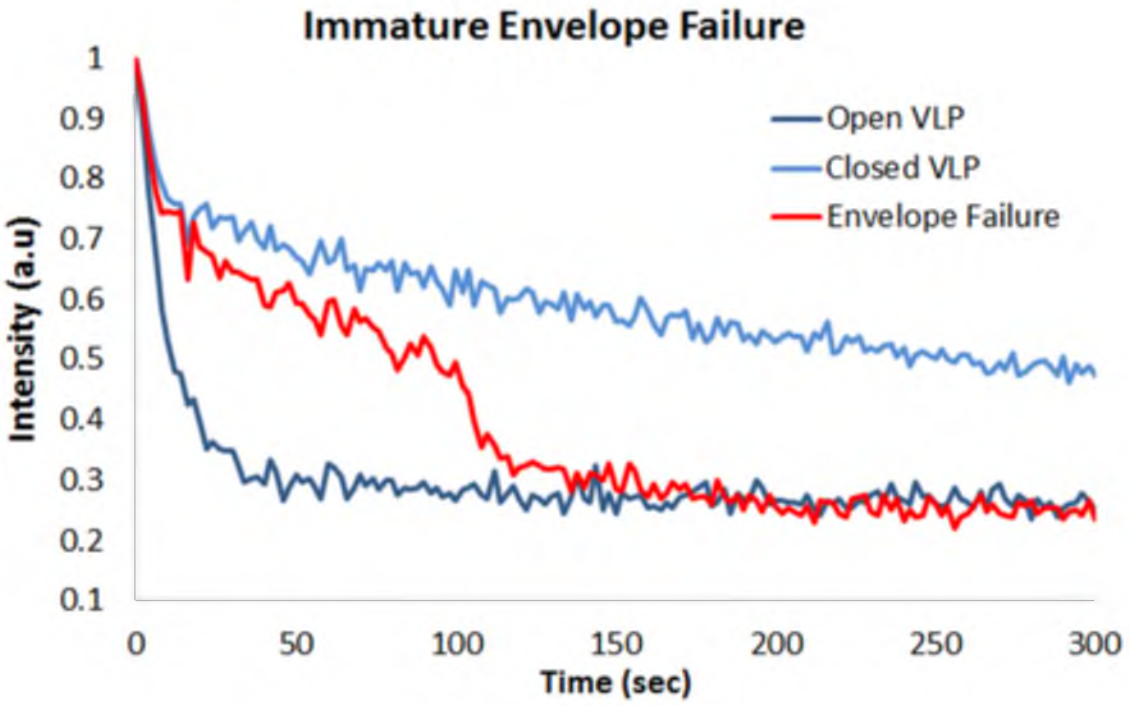

Figure 3.4 The intensity profiles of three immature HIV VLPs during a quench. The dark blue curve shows the typical quenching behavior of an open VLP, the light blue curve shows that of a closed VLP, and the red curve illustrates that of a VLP whose envelope ruptured part way through the quench.

We see that they first follow the typical closed VLP quenching behavior and then suddenly drop down to the intensity of the VLPs we classify as having compromised envelopes. This indicates that there is no difference between what we classify as an open VLP and what we classify as a closed VLP other than the integrity of the viral envelope. This same behavior can also be seen in VSV virions (data not shown).

3.6 Discussion

We have measured the permeability of bald immature HIV VLPs as well as VSV-G pseudotyped HIV VLPs and VSV virions. All virions/VLPs were found to permeate protons through nano-pore formation followed by diffusion across the membrane. A summary of the permeation rates is presented in Figure 3.5. These data demonstrate that permeation from transient pores in HIV increases two-fold through maturation of the VLP. The resulting 2:1 ratio of transient pore permeability may be due to the cleavage of the Gag lattice which reinforces the lipid envelope of immature VLPs [73,95,113]. This indicates that the presence of proteins along the viral envelope may decrease permeability due to transient pores in both HIV and VSV. The variations in permeability may reflect differing rates of pore formation and/or differing lifetimes of transient pores.

Together, these observations suggest that mature and immature HIV VLPs and VSV are all permeable to protons. In both transient pore

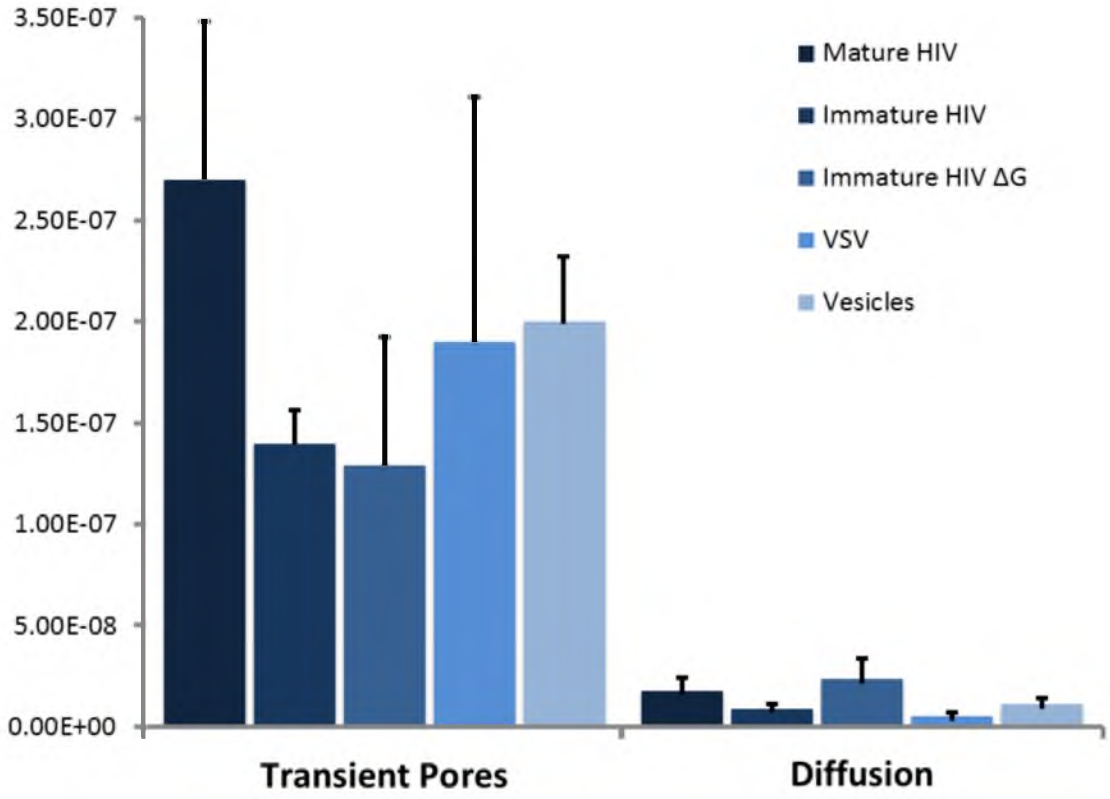

Figure 3.5: A comparison of the permeations (cm/s) of pores and diffusion for mature HIV, immature HIV both with and without VSV-G pseudotyping, VSV, and lipid vesicles.

permeability and diffusion permeability, mature HIV VLPs have the highest rates. There are two main mechanisms by which proteins bound to the inner leaflet of the envelope may decrease proton permeability. First, in immature HIV VLPs, the Gag lattice effectively extends the distance that protons must transit to enter the interior of the VLP and protonate SEpH. The matrix protein and nucleoprotein serve the same purpose in VSV, extending the distance protons must travel by ~190 Å[43]. Second, the Gag lattice also modifies the mechanical properties of the envelope [73,95], likely contributing to the envelope's susceptibility to transient pore formation and proton diffusion. It is possible that the VSV matrix protein and nucleoprotein do not modify the properties of the envelope to the same extent as the Gag lattice, resulting in a lesser effect on the envelope's susceptibility to transient pore formation.

While our data does not make clear the mechanisms by which proteins inhibit proton permeability, it is evident that, in general, permeability decreases with increased protein structure along the envelope.

3.7 Conclusions

VSV virions as well as HIV VLPs, either mature or immature, pseudotyped with VSV-G or bald, are permeable to protons around neutral pH. It takes less than 10 minutes for the interior of the virion to equilibrate with the outside pH. This rate is very similar to the rate by which 150 nm lipid

vesicles equilibrate to the outside pH (Figure 3.5). Although the permeation rate of the membrane varies significantly due to protein binding at the inner leaflet of the virion, all virions remain permeable. So can these virions be assumed impermeable? We propose that the answer to this question depends on the time scale on which one is observing these effects. Within very short timescales, the interior of the virion will respond to the external pH through formation of transient pores but these pores are unable to equilibrate the full pH gradient. Therefore, if the virions need to lower the internal pH drastically during their entry, as is suggested for influenza and VSV [53,103], then proteins associated with the envelope like M2 and VSV-G need to help equilibrate the proton gradient at low pH. Our study also shows a real risk of envelope compromise when virions are exposed to a sudden lower pH environment (see Figure 3.4). The rapid equilibration of the internal cavity of the virion through pumps may also serve as a mechanism to protect the membrane against these ruptures.

Bald HIV VLPs were assumed to be impermeable in previous studies, our studies show that these VLPs are permeable; however, none of our HIV VLPs incorporate the full length HIV envelope protein Env. Therefore, we do not claim to have measured the final permeability of HIV virions, rather the permeability of HIV VLPs in their bald as well as VSV-G pseudotyped state.

3.8 Acknowledgements

The authors thank Dr. Wesley Sundquist for sharing the HIV vector system. This work was supported by grant 1121972 (SS) from the National Science Foundation.

3.9 Postpaper Discussion

This paper was authored and submitted for publication as a Biophysical Journal Letter; however, the journal requested that the letter be expanded into an article, as the material was too long to be properly treated in a letter format. The above is the expanded article in process of being written at the time this dissertation was being written.

CHAPTER 4

SAMPLE PREPARATION FOR SINGLE VIRION ATOMIC FORCE MICROSCOPY AND SUPER-RESOLUTION FLUORESCENCE IMAGING

Jeffrey A. Hodges[1,2] and Saveez Saffarian[1,2,3]

1 Department of Physics and Astronomy, University of Utah
2 Center for Cell and Genome Science, University of Utah
3 Department of Biology, University of Utah

At the time of submission of this dissertation, this article has been accepted for publication online by the Journal of Visual Experiments, and is in press as e51366, URL: http://www.jove.com/video/51366 DOI: doi:10.3791/51366

4.1 Chapter Introduction

After writing the papers contained in Chapters 2 and 3, it became clear that significant space was being utilized within papers to explain the protocols employed in both our AFM and super-resolution techniques. In order to resolve this issue, the paper contained here in Chapter 4 was written so it can be referenced in the future, thus freeing space in future papers.

This paper primarily discusses sample preparation that can be utilized for a variety of techniques utilizing viruses. The initial sections include glass preparation and surface chemistry followed by viral adsorption to the surface. Also included are particulars on how to prepare samples for AFM and super-resolution microscopy.

This paper is in press at the time of the writing of this dissertation.

4.2 Abstract

Immobilization of virions to glass surfaces is a critical step in single virion imaging. Here, we present a technique, adopted from single molecule imaging assays which allows adhesion of single virions to glass surfaces with specificity. This preparation is based on grafting the surface of the glass with a mixture of PLL-g-PEG and PLL-g-PEG-Biotin, adding a layer of avidin, and finally creating virion anchors through attachment of biotinylated virus specific antibodies. We have applied this technique across a range of experiments including atomic force microscopy (AFM) and Super-resolution

fluorescence imaging. This sample preparation method results in a control adhesion of the virions to the surface.

4.3 Introduction

Charge based nonspecific interactions are routinely used for adhesion of virions in atomic force microscopy [73,95]. These techniques especially work well when used on virions without an envelope which have very stiff capsids [16,17,18,19]. Although these techniques are very effective in immobilizing the sample, they do not prevent non-specific binding of proteins to the surface. The nonspecific binding can create a problem when attempting to image virions with AFM and super-resolution fluorescence techniques that require incubations of the sample with various antibodies. Here, we outline a sample preparation method for specific immobilization of virions.

Poly(ethylene glycol) (PEG) grafted to poly (L Lysine) (PLL) and adsorbed onto a glass surface provides a significant block for the electrostatic interactions of proteins with glass [114]. Single molecule assays, which require immobilization of single molecules on glass surfaces, have taken advantage of this property and used it to create a specific PEG based single molecule immobilization technique [115,116,117]. This preparation was also used to immobilize clathrin cages onto the glass surface [118] as well as creating a homogenous fibronectin coating for control cell adhesion [119].

We have adopted the sample preparation method based on PLL-g-PEG adsorption to glass surfaces from single molecule imaging methodologies and applied it to imaging single virions of vesicular stomatitis virus (VSV). These single virions were imaged using atomic force microscopy (AFM). Similar experiments were also performed on functionalized beads as a control. The virions were also imaged by super-resolution fluorescence microscopy were a VSV-G antibody labeled with alexa 647 was used to create an image of the envelope of single virions. High-resolution fluorescent imaging utilizes localization of single molecules to create an image [9,10,11]. fPALM Bi-planar imaging allows localization of single molecules with 20nm in plane and 50nm resolution along the optical axis [10,30] this Bi-planar technique was used to image super-resolution fluorescent images present in this study. An alternative technique that has similar results is STORM [11,28,120].

Both AFM and super-resolution fluorescent images of VSV anchored to the glass by the procedures outlined in this paper, showed specific binding of virions to the glass with minimum nonspecific interactions [121]. Here, we present the sample preparation protocols for the AFM and super-resolution fluorescent imaging experiments. In brief: Clean glass coverslips are functionalized by adsorbing a mixture of PLL-g-PEG and PLL-g-PEG-biotin. It is typical for this thin film to be engineered to provide between 15% to 25% functionalized biotin on a coated surface. The coverslips are further incubated with tetrameric avidin. A biotinylated viral antibody is then used to create a

unique binding site for the virions. Binding of the antibody can be done in two ways.

The first method is optimized for AFM, however, it remains suitable for super-resolution fluorescence imaging. In this method the avidin coated surface is treated with biotinylated antibody prior to viral adhesion. The immobilized virions are treated with alexa 647 labeled antibody to cover the envelope and allow super-resolution fluorescence imaging of the virions.

The second method is to attack the virus in solution with the biotinylated antibody and alexa 647 labeled antibody prior to adhering the viruses to the avidin treated surface; this method is optimized for super-resolution fluorescence imaging experiments in which recovery of the viral envelope is important. This method has the advantage of allowing uniform antibody coating on the viral surface. The biotinylated antibody may be mixed with alexa 647 labeled viral antibodies in ratios that allow for sufficient adsorption of the virus to the avidin treated surface while maintaining a high concentration of fluorescent label on the exterior of the viral envelope. These alexa 647 labeled viral antibodies are not biotinylated and their excess may be rinsed away in order to reduce background noise.

4.4 Protocol

- 1. Chemistry Preparation

    1.1) Preparation and storage of PLL-g-PEG-Biotin and avidin:

1.1.1) Dissolve the polymer PLL-g-PEG-biotin in PBS buffer according to manufacturer's directions at a concentration of 1.0 mg/ml.

1.1.2) Aliquot according to coverslip size (see Table 4.1) and store at -80 °C for up to 1 year.

1.2) Preparation and storage of Avidin/NeutrAvidin

1.2.1) Dissolve the unlabeled Avidin/NeutrAvidin in PBS buffer according to the manufacturer's directions at a concentration of 1.0 mg/ml.

1.2.2) Aliquot according to coverslip size (see Table 4.1) and store at -20 °C for up to 3 years.

1.3) Virus sample preparation: Prepare virus samples according to experimental need and lab protocol prior to this assay. Utilize step 1.3.1 for method 5A, or 1.3.2 for method 5B.

1.3.1) Prepare virus samples for method 5A in advance of stage 2. Utilize prepared viral samples within 1–2 days of preparation, or aliquot according to cover slip size (see Table 4.1) then flash freeze in liquid nitrogen and store at -80°C for up to 1 year. When thawed, use immediately.

Table 4.1 Fluid aliquots according to coverslip size.

Coverslip Size	Fluid
40 mm	65 µl
35 mm	50 µl
30 mm	36 µl
25 mm	25 µl
20 mm	16 µl

1.3.2) Prepare virus samples for method 5B similar to 1.3.1. Thaw aliquots of virus in advance of 5B and store at 4 °C no more than 24 hours prior to mixing with antibodies.

1.4) Prepare appropriate biotinylated antibodies for the experiment.

- 2. Coverslip Cleaning in Preparation for Chemical Treatment

2.1) Place coverslips in an appropriately sized Teflon coverslip rack that holds them in a vertical orientation and submerge them in a beaker filled with filtered (0.2 μm) ethyl alcohol (190 proof).

2.2) Sonicate the coverslips in the filtered ethyl alcohol (190 proof) for 30 minutes.

2.3) Remove coverslips from alcohol and rinse coverslips extensively with ultra-pure water.

2.4) Place rinsed coverslips in a separate clean Teflon rack and beaker filled with 1 M NaOH.

2.5) Sonicate the coverslips in the 1 M NaOH for 30 minutes.

2.6) Remove coverslips from NaOH and rinse them extensively with ultra-pure water.

2.7) Dry the rinsed coverslips with a nitrogen stream, and place them in a clean, dry Teflon rack.

2.8) Inspect the coverslips for any visible film or particles which remain on the coverslip. If any visible material remains, the

coverslip has not been properly cleaned and rinsed. If not properly cleaned repeat steps 2.1–2.7.

2.9) Clean the coverslips with oxygen-plasma for 2 minutes. This step is optional but recommended.

- 3. Formation of the PLL-g-PEG Thin Film Layer

3.1) Immediately after drying in the nitrogen stream (or the optional oxygen-plasma), place one coverslip horizontally in a sterile petri dish. Pipet in the center of the coverslip an appropriate amount of thawed PBS buffered PLL-g-PEG-biotin (see Table 4.1).

3.2) Place another cleaned coverslip atop the fluid in a sandwich method. Note that this method consists of having two coverslips incubate their chemical films by orienting their chemically treated "active faces" towards each other, separated only by the current chemical layer. Make sure there is sufficient fluid such that the volume between the two coverslips is completely filled with fluid, but that no fluid leaks out from between the coverslips (See Table 4.1). The "active face" henceforth designates coverslip faces which have been in contact with the fluid in the sandwich configuration.

3.3) Place the lid of the petri dish over the coverslip sandwich and incubate at room temperature for 45-60 minutes.

3.4) Remove lid of petri dish and pick up the sandwich with a pair of tweezers. Be careful not to pinch out excess fluid. Use the thumb and index finger to pinch the sandwich lightly and slide the coverslips in opposite directions horizontally with respect to one another, then separate the two coverslips from each other without touching the active faces.

3.5) Rinse both active faces with ultra-pure water by pipetting 25 ml of ultrapure water over the active face 2-4 times, and then dry the coverslips with a nitrogen stream. Be sure to note which coverslip faces are active.

3.6) Utilize the coverslips immediately, or store overnight with the active face up in a sterile petri dish placed in a dust free low humidity environment.

- 4. Avidin Binding Enhancement

4.1) Place a PLL-g-PEG treated coverslip with active face up in a sterile petri dish.

4.2) Pipette an appropriate amount of thawed avidin in buffer (prepared in step 1.2) onto the middle of the active face.

4.3) Place another coverslip (active face downward) atop the fluid in the sandwich method. Note the active face of the coverslips. It is important that the active faces be in contact with the fluid during the incubation (see step 3.2).

4.4) Place the lid of the petri dish over the coverslip sandwich and incubate at room temperature for 25-30 minutes.

4.5) Remove the petri dish lid and separate the two coverslips as described in step 3.4, making sure to keep track of and not touch the active faces.

4.6) Rinse both active faces with ultra-pure water by pipetting 25 ml of ultrapure water over the active face 2-4 times and then dry the coverslips with a nitrogen stream. Note the active face of the coverslips. Use immediately for the next stage.

IMPORTANT NOTE: There are two distinct methods for completing sample preparation depending on the type of assay the experiment entails. The experimenter should proceed with stage 5A in which the virus is anchored to the glass before any additional antibody treatment required for super-resolution imaging is added. 5B describes an alternative method of labeling the virus in solution before anchoring it to the glass. The representative data in this manuscript are prepared using 5A. An appropriate method should be selected according to experimental assay type.

- 5A. Active Face Antibody Tether

5A.1) Immediately after drying with a nitrogen stream in stage 4.6, place an Avidin treated coverslip active face up in a sterile petri dish.

5A.2) Pipette an appropriate amount of thawed biotinylated antibody in buffer onto the middle of the active face (see Table 4.1).

5A.3) Place another coverslip (active face downward) atop the fluid in a sandwich method. Note the active face of the coverslips, it is important the active faces are in contact with the fluid for incubation (see step 3.2).

5A.4) Place the lid of the petri dish over the coverslip sandwich and incubate at room temperature for 45–60 minutes.

5A.5) Remove the petri dish lid and separate the two coverslips as described in step 3.4, making sure to keep track of and not touch the active faces.

5A.6) Rinse both active faces with PBS by pipetting 25 ml of PBS over the active face 2-4 times, do not dry and use immediately. Be sure to keep track of which coverslip faces are active.

5A.7) Place an antibody treated coverslip active face up in a sterile petri dish, and pipette an appropriate amount of thawed virus in buffer onto the middle of the active face.

5A.8) Place another coverslip (active face downward) atop the fluid in a sandwich method. Note the active face, as it is important the active faces are in contact with the fluid for incubation (see step 3.2.)

5A.9) Place the lid of the petri dish over the coverslip sandwich and incubate at room temperature for 45-60 minutes.

5A.10) Remove the petri dish lid and separate the two coverslips as described in step 3.4, making sure to keep track of and not touch the active faces.

5A.11) Rinse both active faces with PBS by pipetting 25 ml of PBS over the active face 2-4 times. Do not dry the coverslips, instead place them in a Teflon rack and beaker filled with PBS immediately. Be sure to keep track of which coverslip faces are active.

5A.12) Utilize the prepared samples immediately or store in an appropriate buffer at 4 °C for up to 3 days without significant loss of integrity.

IMPORTANT NOTE: If samples are to be used in an AFM assay, the preparation is complete and they can be utilized immediately or stored as described in step 5A.20 – 5A.21. If samples are to be utilized in a super-resolution fluorescence

imaging assay, proceed to the antibody labeling described in steps 5A.12–5A.19.

5A.13) Place both virus treated coverslips active face up in a sterile petri dish and pipet enough protein blocking buffer on the coverslips to bead enough fluid volume to cover the central 95% of the coverslip without flowing any blocking buffer off the coverslip (typically 100–200 µl.) Incubate at room temperature for 60–90 minutes.

5A.14) Carefully remove blocking buffer by removing the coverslips one at a time from the petri dish and pouring the fluid off of the coverslip into a waste beaker. Be careful not to drop the coverslip.

5A.15) Rinse both active faces with PBS by pipetting 25 ml of PBS over the active face 2–4 times, do not dry and use immediately. Be sure to keep track of which coverslip faces are active.

5A.16) Place a single blocking buffer treated coverslip active face up in a sterile petri dish, and pipette an appropriate amount of fluorescently labeled viral antibody in buffer onto the middle of the active face.

5A.17) Place another coverslip (active face downward) on top the fluid in a sandwich method. Note which face is active, it is

important that the active faces are in contact with the fluid for incubation (see step 3.2).

5A.18) Place the lid of the petri dish over the coverslip sandwich and incubate at room temperature for 30 minutes.

5A.19) Remove the petri dish lid and separate the two coverslips as described in step 3.4, making sure to keep track of and not touch the active faces.

5A.20) Rinse both active faces with PBS by pipetting 25 ml of PBS over the active face 2-4 times, do not dry and use immediately. Be sure to keep track of which coverslip faces are active.

5A.21) Do not dry the coverslips, instead place them in a Teflon rack within a beaker filled with PBS. Be sure to keep track of which coverslip faces are active.

5A.22) Utilize the prepared samples immediately or store in an appropriate buffer at 4°C for up to 3 days without significant loss of integrity.

- 5B. In-Solution Antibody Attack

This method is an optional enhancement of the labeling strategy for the super-resolution fluorescent imaging. By applying the in solution attack, better antibody coating on the viral surface can be achieved.

5B.1) Mix antibody solutions in ratios according to the experiments need. Example 1:4 ratio of 0.01 mg/ml biotinylated antibody to 0.01 mg/ml fluorescently labeled antibody will give a good binding affinity and allow for good envelope recovery in a super-resolution imaging assay.

5B.2) Mix equal portions of the antibody and virus solutions, respectively, prepared in (5B.1) and (1.3). Mix gently by pipetting up and down a few times in the aliquot. This resultant solution can be stored until needed for up to 24 hours at 4°C.

5B.3) Upon completion of step 4.6, place an avidin treated coverslip with active face up in a sterile petri dish.

5B.4) Pipette an appropriate amount of virus with antibody solution (prepared in step 5B.2) onto the middle of the active face.

5B.5) Place another coverslip (active face downward) atop the fluid in a sandwich method. Note the active face, as it is important the active faces are in contact with the fluid for incubation (see step 3.2).

5B.6) Place the lid of the petri dish over the coverslip sandwich and incubate at room temperature for 45–60 minutes.

5B.7) Remove the petri dish lid and separate the two coverslips as described in step 3.4, making sure to keep track of and not touch the active faces.

5B.8) Rinse both active faces with PBS by pipetting 25 ml of PBS over the active face 2–4 times. Do not dry the coverslips, instead place them in a Teflon rack and beaker filled with PBS immediately. Be sure to keep track of which coverslip faces are active.

5B.9) Utilize prepared samples immediately or store at 4°C for up to 3 days without significant loss of integrity.

- 6. Atomic Force Microscopy Material Property Measurement

6.1) Turn on the AFM lasers and open the AFM software. Select the appropriate scanning mode for the desired assay from the opening dialog. All necessary windows should open by default; if not consult your user's manual in order to open the desired windows.

6.2) Select a cantilever appropriate to the desired measurement and insert it into the cantilever housing according to manufacturer guidelines. There are a wide range of conditions and experiment types for which there are a variety of cantilevers. The experimenter should research cantilevers according to their need.

6.3) Insert the cantilever housing into the AFM head according to manufacturer's guidelines.

6.4) If the sample is to be used under wet conditions, remove the sample from the storage buffer and proceed to step 6.7.

6.5) If the sample is to be used under ambient (dry) conditions, remove the sample from its storage buffer and rinse it briefly by dipping in a beaker of ultra-pure water. Note: This will leave a thin hydration layer on the sample, which may induce capillary attraction with cantilevers having a low spring constant.

6.6) If the sample is to be utilized in ambient (dry) conditions, gently dry the sample with a nitrogen stream.

6.7) Gently dry the back side of the coverslip with a dust free filter paper, making sure to not touch the active face of the sample.

6.8) Place the sample in the appropriate AFM sample holder, then place the sample on the AFM stage.

6.9) If the sample is to be imaged under wet conditions, pipette a small amount of buffer onto the center of the sample (~10 μl)

6.10) Place the AFM head over the sample.

6.11) If the sample is wet, make sure that the cantilever and AFM tip penetrate the surface layer, and that there are no bubbles between the cantilever and cantilever housing.

6.12) Align the AFM laser with the cantilever in accordance with manufacturer recommendations in order to obtain the optimal signal.

6.13) Measure cantilever resonant frequency and set the scan frequency according to experiment type.

6.14) Lower the AFM tip to the surface and optimize signal settings.

6.15) Perform a 20 μm square AFM scan in the mode of your choosing. Tapping (AC) mode was used in generating representative data. Identify virus candidates by approximate height, which can typically be seen as sharp spikes on the glass surface.

6.16) Select a virus candidate and center the scan head above it.

6.17) Perform a 250 nm square scan (or appropriate super-resolution scan) about the selected virus in order to obtain its topology and orientation.

6.18) Select a point on the virus for the material property measurement (e.g., the center of a spherical virus for a Young's modulus measurement) and perform the measurement according to manufacturer's directions.

- 7. Super-Resolution Imaging Method

7.1) Open the super-resolution imaging software and calibrate the software according to manufacturer's guidelines.

7.2) Calibrate the super-resolution imaging equipment in accordance with manufacturer's directions utilizing fluorescent beads.

7.3) Assemble the sample imaging buffer from stocks just prior to imaging by combining 50 μL of 1 M MEA and 100 μL of 10 x Gloxy to 850 μL of stock buffer. Keep imaging buffer on ice for the duration of the experiment.

7.4) Remove a prepared coverslip with sample from its storage buffer and rinse it five times by dipping it in a beaker of ultra-pure water.

7.5) Dry the nonactive coverslip face utilizing a dust free filter paper. Make sure to not touch the active face.

7.6) Insert into an imaging system sample holder and add 250 μL of imaging buffer to the sample holder. It is reasonable to exchange the imaging buffer on the sample every 2 hours to maintain consistent results.

7.7) Cover the sample holder with parafilm to decrease atmospheric interaction with the room environment.

7.8) Place the sample holder into the imaging equipment for imaging.

7.9) Bring the sample into focus utilizing the manufacturer's directions.

7.10) Image the sample according to the super-resolution technique being employed. Be sure to adjust imaging conditions to

optimize signal while decreasing simultaneous activations of photo-switchable fluorophores.

IMPORTANT NOTE: Imaging conditions are sample dependent and vary according to experimental need. A typical experiment utilizing alexa 647 efficiently initialized to their dark state in the imaging buffer can then be photo-activated through application of 405 nm UV light. Images are obtained by exciting a sparse subset of alexa 647 molecules within a densely labeled sample and localizing each fluorophore with a precision limited primarily by the number of collected photons. This procedure is iterated repeatedly by the software until a desired number of acquisition cycles have happened. The experimenter should have this setting correlate with each fluorophore in the sample having been photo-bleached.

7.11) When imaging is completed, shut down the imaging equipment according to manufacturer's directions. The software may be left open for data analysis.

7.12) Data analysis is heavily dependent upon experiment; however, in all cases identify viruses by their full width at half maximum, which is compared to the known virus dimensions, making sure to take into consideration the additional size of fluorescent labels.

7.13) For better visualization, view samples by utilizing either the Isosurface rendering option or the volumetric rendering option, both of which are typically found in super-resolution imaging software.

4.5 Representative Results

4.5.1 Single Virion Imaging Using AFM

The sample preparation protocol outlined was used in anchoring wild type virions to the glass surface. VSV virions are bullet shaped 180 nm in length and 80 nm in diameter. As there are a variety of virions for which this technique may be applied, the concept is also demonstrated here on biotinylated 36 nm beads as well. The resulting AFM experiments are shown in Figure 4.1. It is important to note that the VSV virions have a lower Young's modulus (~100 MPa) compared to the viruses without an envelope (~GPa). The particular images of single virion VSV were obtained under tapping mode in ambient conditions with a stiff cantilever. The aim has been to deform the virus to the point that the extra protein density within the virus becomes visible as a bump within the AFM image. This method is used to detect the extra protein density within the virus cavity [121].

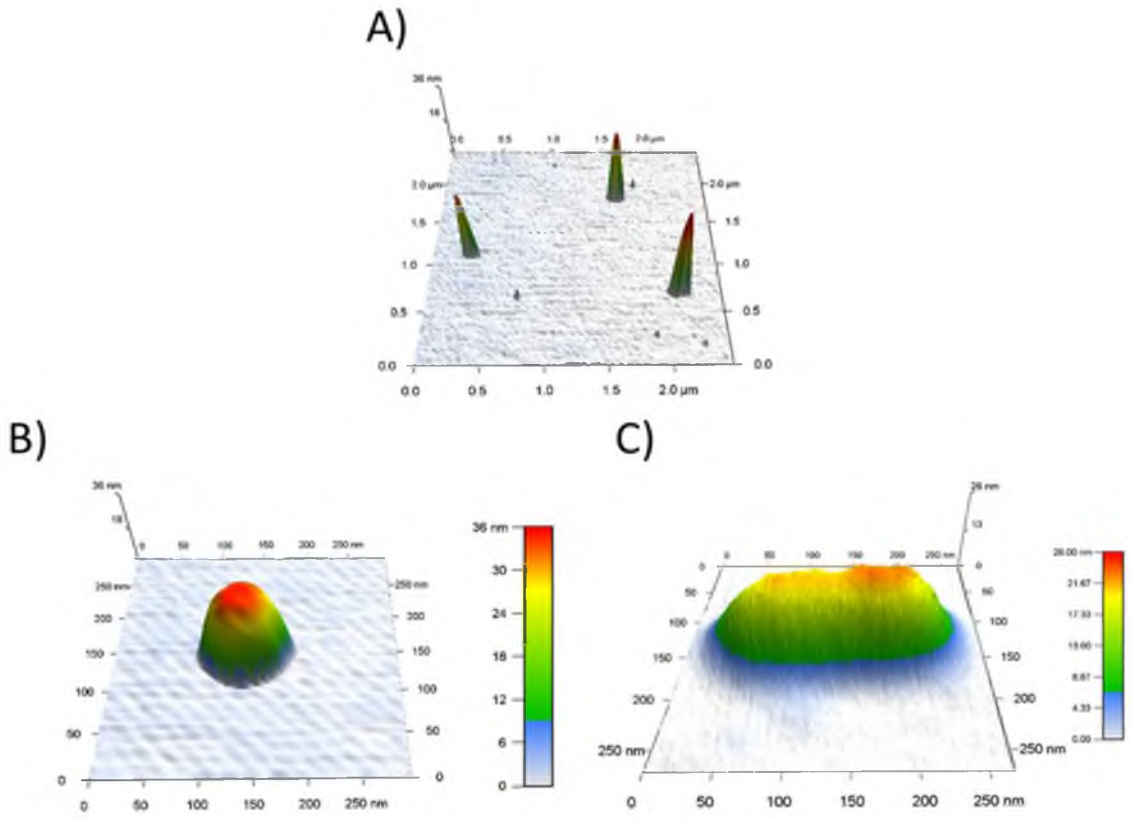

Figure 4.1 AFM imaging of beads and VSV on the functionalized PEG surface. This AFM scan of 36 nm biotinylated beads (A&B) and a VSV virion (c) anchored to the surface with a biotinylated VSVG antibody. AFM was done in AC air topography scan mode. The tip radius is < 25 nm and measurements were carried out under force modulation and light tapping. The tip had a force constant of 3N/m and resonant frequency 75 KHz with uncertainty of 15 KHz. While the beads retained their height during the AFM scan, the VSV virion has a significantly smaller Young's modulus and is significantly deformed in height. In this image the virion was specifically imaged with a stiff cantilever in tapping mode which produced a small XY convolution (used to determine the tip vs blunt end of the virus) and the height difference between the tip and blunt end of the virus is used to detect extra protein density at the blunt end of the virus [121].

4.5.2 Single Virion Imaging Using fPALM

Alexa 647 labeled VSV-G antibodies were used to coat the envelope of individual VSV virions for super-resolution experiments using method 5A. To demonstrate the tethering density and the low unspecific binding, a large scan of the sample is shown in Figure 4.2A. The recovery of the viral envelope on a representative virion is shown in Figure 4.2B (blue isosurface).

4.6 Discussion

Single virion imaging with AFM and High-resolution fluorescence imaging can be used as an alternative methodology to CryoEM tomography. Each one of these methodologies has their specific strengths. For example, AFM can be done on WT virions with no requirement on tagging the sample or the internal viral proteins. The location of viral structures is deconvolved from their contributions to the elastic properties of the virion.

Super-resolution imaging in combination with the newly developed viral reverse genetic approaches becomes a powerful technique for localizing low copy number viral proteins [122]. Recombinant viruses with replacement of their proteins with proteins fused to fluorescent proteins can be made and purified using these reverse genetic approaches. Although super-resolution imaging has specificity in part due to the genetic tagging, it requires the use of the mutant viruses.

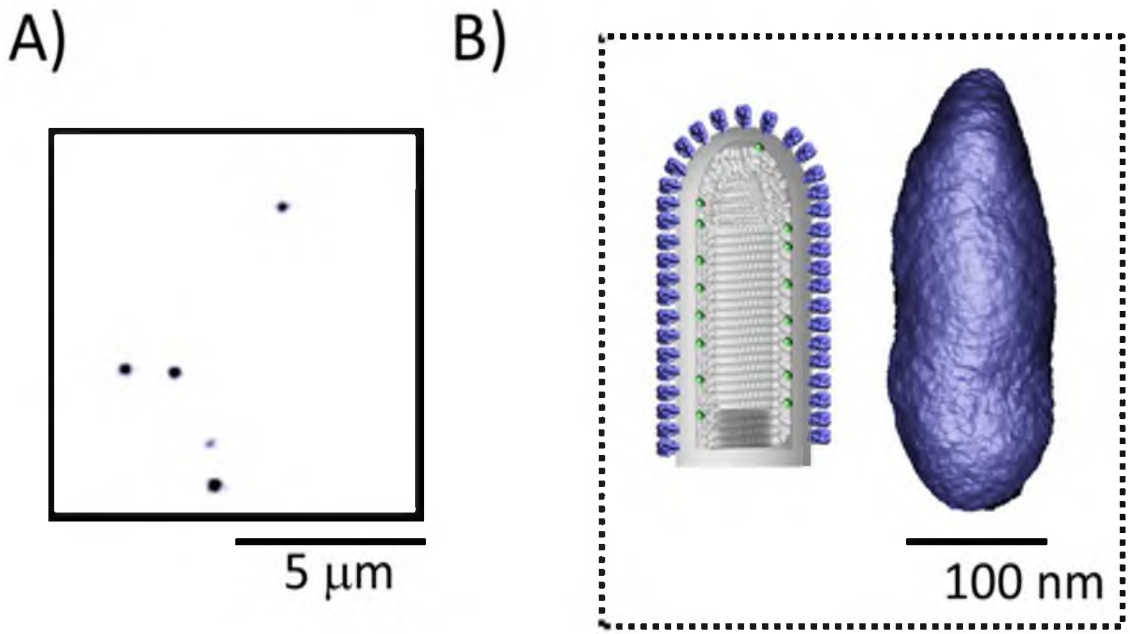

Figure 4.2 Fluorescence based imaging of VSV virions on the PEG functionalized surface. A) Recombinant VSV virioins immobilized on the PEG surface using a biotinylated anti-VSVG antibody imaged in wide field fluorescence. B) High resolution fluorescence reconstruction of the envelope of VSV attached to the PEG surface through a biotinylated anti-VSVG antibody and decorated with alexa 647 labeled anti-VSVG antibodies (Method 5A was used for creating these images). The blue surface is a two-dimensional isosurface projection. Left shows a model of the bullet shaped virus.

AFM and super-resolution imaging are complimentary methods that utilize very similar sample preparations. The methods outlined in this paper, which are adopted form earlier single molecule imaging assays, allow anchoring of single virions with little effects on the topology of the virions.

4.7 Acknowledgments

We thank Dr Till Böcking for the original single molecule preparation protocol.

This work was supported by NSF grant 1121972(SS).

4.8 Disclosures

The authors have no competing financial interests in this paper.

4.9 Materials and Equipment

The following is a table (Table 4.2) of the materials and equipment utilized within the processes described in this chapter.

Table 4.2 Materials and Equipment

Name of Reagent/ Equipment	Company	Catalog #	Comments/Description
Glass coverslips (fPALM)	Electron Microscopy Services	72225-01	25 mm Coverslips
PLL(20)-g[3.5]-PEG(2)/PEG(3.4)-Biotin (20%)	SuSoS	-	Stock: 0.5mg/mL in PBS
NeutrAvidin biotin-binding protein	Invitrogen	A2666	Stock: 0.25mg/mL in PBS
Alexa Fluor® 647 goat anti-rabbit IgG (H+L)	Invitrogen	A21245	1:200 in 0.2M KPO4, 0.15M NaCl, 10%Glycol, pH 7.2 buffer
α-VSV-G	Invitrogen	ab34774	1:200 in 0.2M KPO4, 0.15M NaCl, 10%Glycol, pH 7.2 buffer
Gluox	Sigma	G2133-250KU	Glucose oxidase type seven from Aspergillius
Catalase	Sigma	C40-100mg	Catalase from Bovine liver
MEA	Sigma	30070-10G	Cysteamine (MEA
Stock Buffer			50 mM Tris-HCL (pH 8.0) + 10mM NaCl + 10% glucose
NTE			10 mM Tris pH 7.4, 100 mM NaCl, 66 mM EDTA
Slide-A-Lyzer, mini dialysis unit	Thermo Scientific		10,000 MWCO
Microscope Cover Glass: 35 CIRCLE #1	Fisher-brand	35 CIRCLE #1	

CHAPTER 5

CONCLUSION

In nature, and in particular, the biophysics of nature, the form of a biomaterial or protein follows its function. Nature is exceedingly good at facilitating biological processes with a minimum of material, or an optimal configuration. Because of this fact, not only is the folding of proteins important, but their configuration within their natural environment is critical to understanding the underlying physics of their natural process. The papers contained in Chapters 2 through 4 are all related to the processes involved in viral property studies, in this chapter we propose how these techniques may be combined to improve future research.

Specifically when it comes to Chapter 2, the application of super-resolution microscopy techniques to in vivo viral protein localization is a new process at the time of the writing of this dissertation. However, it is clear that the process of envelope recovery and internal protein labeling is a viable solution for determining protein configurations that may not be determinable by other means. This gives scientists a powerful new, nondestructive tool that is capable of resolving proteins in assembled viruses, and possibly for

viruses in the process of assembly. This is critical for the analysis and research of viral proteins.

As mentioned in the conclusion of Chapter 2, the techniques discussed in that chapter have been refined in order to allow for a superior recovery of both viral envelope and protein location within a VSV virion. The improved viral envelope recovery was discussed in Chapter 4, and consists of immunolabeling of the virion in solution prior to adhesion to the glass surface. While this technique has the advantage of improving envelope coating with the fluorescent label while decreasing nonspecific labeling which is seen as noise in the assay, it is not the only option for improvement in the method. Indeed, more innovative techniques may be practically applied to envelope recovery. One obvious improvement is by decreasing the offset of the fluorophore from the envelope when utilizing a fluorescently labeled antibody. It is known that these antibodies have an offset from the envelope of approximately 15 nm. This offset may be minimized by utilizing a fluorescent anchor directly within the viral envelope, or directly grafted to another envelope viral protein. This would eliminate the offset generated by attacking the envelope with a labeled antibody.

Another consideration is that of internal proteins of interest. As mentioned in Chapter 2, the Saffarian lab has developed VSV proteins labeled with photo-switchable labels in order to utilize the full advantages of the STORM/PALM technique. It is hoped at the time of this writing that future

work with these improvements will illuminate the protein configuration within the central cavity further and possibly allow for the counting of individual proteins of interest within a viral body. In addition, by labeling internal proteins with photoactivatable or photo-switchable fluorophores, internal protein configurations and potential patterns may be observable. This is something which has not been possible for disordered proteins in the past. It is hoped that with the foundation techniques in this dissertation, and known advancements which are currently being applied to cellular assays will illuminate much about viral proteins which is currently not well understood.

Another potential application of the materials contained in this dissertation is that of combined techniques. The integration of atomic force microscopy with nano-resolution optical techniques on the same coverslip, within the same apparatus appears to be a natural marriage of the two techniques. By having the topological scan of an AFM visually integrated with the 3-D localization of proteins, the work of this dissertation would have been significantly easier to discover. As it was, the two processes were handled on samples prepared separately for the two methods, which is not an optimal solution. Additionally, one may consider the practical marriage of TIRF microscopy with PALM. By using an evanescent wave's adjustable field depth, one could naturally control which fluorophores become excited as a function of depth. By quenching a particular Z-depth within an evanescent

field, then adjusting the field depth, one could conceivably step through the Z axis fluorescence during imaging and reconstruct a viral body in layers. It is the belief of this author that many such combinations of technologies will greatly improve viral and small body research in the future.

It is important to remember that not only is viral protein location and configuration important, but also environment. As discussed in Chapter 3, the pH condition of a virus is important, and with the understanding that viral envelopes are permeable, a natural question for consideration is what effect does this have on protein configuration, localization and activity? It is known that pH plays an important role in the life cycles of some viruses, namely VSV, HIV and influenza. But this opens the question of what happens to the asymmetry of phosphoproteins and polymerase within VSV in a low pH environment? Also, what role does pH potentially play in their activation just prior to the fusion of the viral envelope and genomic release into the host cell? This question is mute when one assumes the viral envelope to be impermeable, however, as this is dissertation describes, this is not the case. So what role does pH play during endocytosis of viruses? There are two basic possibilities; one is that it plays no role whatsoever. However, nature abhors a vacuum and pH is a convenient chemical trigger for many biological processes. This indicates that the second possibility, that pH is an important trigger is a valid, and now an open question for consideration. Fortunately,

this question can now be studied utilizing the techniques found in Chapter 2 in different pH environments.

In conclusion, it is important to understand that many existing techniques are powerful at obtaining very specific types of data, however, throughout science it has been the ongoing comparison and correlation across a variety of techniques that generates the models we use to better understand what we study. With biophysics and viruses, this dissertation makes it clear that by applying this rather nebulous ideology more directly to particular questions, many of the unknown processes and configurations of viruses may be better understood. But it is going to require the application of state of the art techniques and fresh thinking in order to capitalize on this idea.

APPENDIX

SUPPLEMENTARY MATERIALS FOR ASYMMETRIC PACKAGING OF POLYMERASES WITHIN VESICULAR STOMATITIS VIRUS

A.1 Introduction

The materials and methods for the paper contained in Chapter 2 are extensive, and much of the work and discussion of technique are not contained in the paper's main body. In order to fully explain the materials and methods, a extensive documenting of the materials and methods was written into supplementary materials to be referenced on the publishers website. To that end the supplementary materials that accompany the publication are extensive, and contained here in the appendix.

A.2 fPALM and Fluorescence Localization

fPALM works by exciting a sparse subset of photo-activatable fluorescent molecules within a densely labeled sample and localizing each fluorophore with a precision limited primarily by the number of collected photons

[7,9,10,11]. Images were recorded with a SR 200 microscope (Vutara, Inc., Salt Lake City, UT) based on the Biplane fPALM approach [30]. The system features 4 laser lines (405, 488, 561, and 647 nm) for excitation and activation of single fluorescent molecules at up to 15 kW/cm2. Speckle-free illumination with an even intensity distribution was realized by a specialized beam homogenizer. Images of fluorescing molecules were recorded with a 60×/1.2NA water immersion objective on an EM-CCD camera (Photometrics Evolve 512). Two color channels were detected sequentially at 50 frames/sec. eGFP data was collected first over 500 frames at 30% power (1.2kW/cm^2), then Alexa 647 (Alexa Fluor® 647 goat antirabbit IgG (H+L) Invitrogen A21245) were collected over 15,000 frames at 100% power (4kW/cm^2). Data analysis was performed using the Vutara SRX software (Version 4.01).

A.2.1 fPALM Sample Preparation

A.2.1.1 Substrate Cleaning

Glass coverslips (Electron Microscopy Services Cat.#72225-01) were prepared in a clean room. Using a Teflon rack the coverslips were submerged in 95% ethyl alcohol, sonicated for 30 minutes, rinsed 4 times in 500mL of MilliQ water, placed in 10M NaOH, and sonicated again for 30 minutes. Using forceps, each coverslip was rinsed under stream of MilliQ water for 30-60 seconds and then stored in MilliQ water.

A.2.1.2 Glass Chemistry

Clean coverslips were dried under a nitrogen stream before addition of chemistry. First, 25μL of biotinylated PEG (SuSoSPLL(20)-g[3.5]-PEG(2)/PEG(3.4)-Biotin (20%) at 0.5mg/mL in PBS) was placed onto a horizontally mounted coverslip. A second cleaned and dried coverslip was placed on top to form a sandwich and left for 45 minutes at room temperature. After incubation, the glass is separated and the "active face" was rinsed twice with 25mL of MilliQ water and allowed to dry for 45 minutes. For optimal results, PEG-ylated glass was used within 24 hours. Next, 25μL of a NeutrAvidin (Invitrogen NeutrAvidin biotin-binding protein A2666, 0.25mg/mL in PBS) was sandwiched between two active faces, incubated for 30 minutes, and rinsed 4 times with 25mL of MilliQwater. Immediately after NeutrAvidin treatment, 25μL of biotinylated antibody solution (α-VSV-G Invitrogenab34774, 1:200 in 0.2M KPO4, 0.15M NaCl, 10%Glycol,pH 7.2 buffer) was sandwiched, incubated for 60 minutes, and rinsed 4 times with 25mL of cold 10mM HEPES pH 7.4. Immediately after antibody treatment, 25 μL of prepared virus (see below) was sandwiched, incubated for 60 minutes, and rinsed four times with 25mL of cold 10mM HEPES pH 7.4.

A.2.1.3 Virus Labeling

To label the virus, the active faces were sandwiched with 25μL of a primary antibody (α-VSV-G rabbit [invitrogen AB34774], 1:400) incubated for 30 minutes, and rinsed four times with 25mL of cold 10mM HEPES pH 7.4. Following the primary antibody, 25μL of a secondary antibody (Alexa Fluor®647 goat antirabbit IgG, Invitrogen A21245) was sandwiched, incubated for 30 minutes, and rinsed 4 times with 25mL of cold 10mM HEPES pH 7.4.

A.2.2 Virus Preparation

Plaque purified VSV:eGFP-P (37C) and VSV:L-eGFP (32C) were grown and purified according to the following protocol.

90% Confluent BHK-21 cells were inoculated with VSV at an MOI of 3 in DMEM containing 2% FBS, 1X PKS and 10mM HEPES (pH 7.4). The medium was extracted the next day and cell debris was removed by centrifugation at 3000 rpm for 5 minutes. After the spin the supernatant was filter clarified through a 0.4 μm filter to remove any additional cellular debris resulting from cell lysis. Virus was then pelleted by centrifugation at 40,000 x g for 90 minutes @ 4°C.Virus pallet was resuspended in NTE (10 mMTris pH 7.4, 100 mMNaCl, 66 mM EDTA) on ice overnight. This solution was further purified through pelleting through a 10% sucrose cushion spin at 157,000 x g for 1 hour @ 4°C. The virus pellet was resuspended in NTE on ice overnight.

This solution was further purified through a 15%-45% sucrose gradient spin at 79,000 x g for 3.5 hours. The virus was extracted at the boundary of the 45% sucrose using a syringe. The final virus prep was dialyzed against NTE overnight to dilute the extra sucrose.

A.2.3 Imaging of Virions via fPALM

A prepared coverslip with sample was removed from its storage buffer and rinsed 5 times by dipping in MilliQ water. The coverslip was then placed to dry active side up on dust free filter paper for 5 minutes, thus allowing the virions to lay down parallel to the glass. After drying, the coverslip was inserted into a Vutara system sample holder, and 250 μL of switching buffer was placed on top of the sample. The switching buffer was assembled from stocks, immediately before imaging and kept on ice. The switching buffer lasted ~2 hours and was replaced 2 or 3 times per imaging session. The sample holder was covered with parafilm to reduce atmospheric interactions and placed set into the fPALM equipment for imaging.

As previously mentioned, images were obtained by exciting a sparse subset of photo-activatable fluorescent molecules within a densely labeled sample and localizing each fluorophore with a precision limited primarily by the number of collected photons. This procedure was iterated repeatedly until each fluorophore in the sample had been photobleached. This method was capable of a localization precision of 20 nm or better. The localization data

was then used to recreate an image of the sample by generating a map of each fluorophore's position in space through analysis of the biplane point spread functions. The envelope of VSV virions was mapped by labeling ~75% of the VSV-G protein on the exterior of the virion with Alexa Fluor®647 (see above). Alexa fluorophores can be efficiently initialized to their dark state in the imaging buffer and can then be photo-activated through application of 405 nm UV light. This method was used to generate a high-resolution three-dimensional map of the viral envelopes shown in red in Chapter 2 Figures 2.1, and 2.2.

A.2.3.1 Imaging Buffer Preparation

A 10x Stock of Gloxy was prepared in advance by adding 1,688 active units (AU) Gluox and 14,040 AU Catalase into 1mL of 50 mMTris with 10mM NaCl (pH 8.0) and mixed gently.

The imaging buffer was created just prior to imaging by adding 50 µL of 1M MEA and 100 µL of 10x Gloxy to 850 µL of stock buffer.

A.2.3.2 Materials

- Gluox: Glucose oxidase type seven Aspergillius #G2133-250KU (Sigma)
- Catalase: Catalase from Bovine liver C40-100mg (Sigma)
- Stock Buffer: 50 mMTris-HCL (pH 8.0) + 10mM NaCl + 10% glucose.
- MEA: Cysteamine (MEA) #30070-10G (Sigma)

A.2.3.3 fPALM Control

Bead data was used to determine the accuracy of the Biplane fPALM as shown below. The precision of localization is inversely proportional to the square root of the collected photon counts. The laser intensity was lowered on the bead samples such that the beads were matched to the typical photon count from the Alexa 647 in order to demonstrate our resolution. Below we present two sets of data, one where the photon counts are around 2000 and a lower bound where the photon counts are around 500.

Bead 1 Statistical Analysis was used to determine fPALM/STORM xyz localization precision on the SR-200 super-resolution microscope. For all the bead particles captured in the images, the x, y and z position was computed through localization analysis. The data from these 1000 localizations are presented for a representative bead in Figure A.1, corresponding to data in Table A.1. For each bead, statistical analysis was performed to determine the standard deviation of the positions over 1000 frames. Similar analysis was performed for all seven beads and the results tabulated in Table A.2.

We also performed mean and standard deviation statistical analysis on the individual 1000 positions obtained for seven beads, each intensity approximately equivalent to 2000 photons, in order to match our standard case. The mean and standard deviation (which is defined as the localization accuracy) was computed and tabulated.

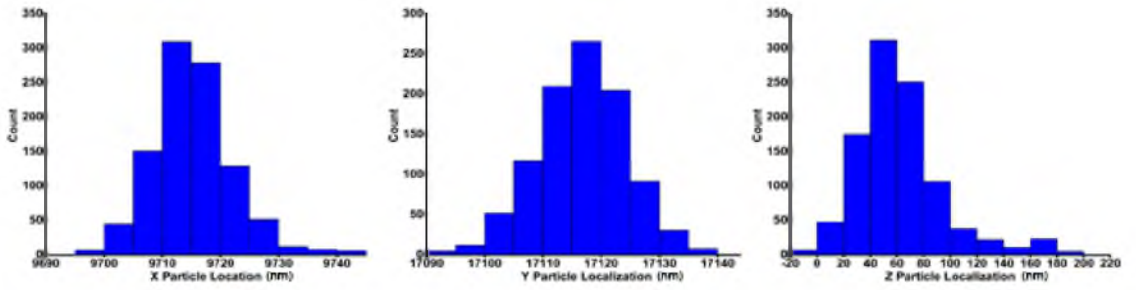

Figure A.1 Statistical analysis of Bead 1 fluorescence distribution showing over 1000 frames of collected data. The variation in location X,Y,Z was 5nm, 7nm, 21nm, respectively. Additionally there was a FWHM in X,Y, Z of 13nm, 17nm, and 51nm, respectively.

Table A.1 Localization precision for 575 photon count sample beads

	X		Y		z		Average number of photons
	FWHM (nm)	Localization Precision (nm)	FWHM (nm)	Localization Precision (nm)	FWHM (nm)	Localization Precision (nm)	
Bead 1	13	5	17	7	51	21	667
Bead 2	20	8	21	9	76	32	459
Bead 3	16	7	16	7	52	22	655
Bead 4	16	7	17	7	60	25	510
Bead 5	15	6	17	7	47	20	572

Localization precision in nm for 5 sample beads showing standard deviations of 9 nm or less with a FWHM of 21 nm or less in all X,Y. For Z, we find a localization precision of 32 nm or less and a FWHM of 76nm or less. The average capture time was corrected to have a similar photon count to our worst virions, around 572 photons per frame.

Table A.2 Localization precision for 2000 photon count sample beads

	X		y		z	
	FWHM (nm)	Localization Precision (nm)	FWHM (nm)	Localization Precision (nm)	FWHM (nm)	Localization Precision (nm)
Bead 1	15	6	12	5	51	21
Bead 2	14	6	13	5	52	22
Bead 3	18	7	14	6	41	17
Bead 4	16	6	14	6	62	26
Bead 5	14	6	13	5	37	15
Bead 6	14	6	13	5	54	23
Bead 7	16	6	17	7	43	18

Table of localization precision and FWHM measurements for 7 beads with approximately 2000 photon counts to match our standard case.

A.2.4 fPALM Analysis

Particles were identified by their brightness from the combined images taken in both planes and two color channels simultaneously. If a particle was identified in multiple subsequent camera frames, data from these frames were combined for the specific identified particle. Background was removed based on the observed signal in the frames before or after the frames in which the particle was observed in. Identified particles were then localized in three dimensions by fitting the raw data in a customizable region of interest (typically 16x16 pixels) centered about each particle in each plane with a three-dimensional model function which was obtained from recorded bead data sets. The four recorded fields were aligned automatically by computing the affine transformation between each pair of planes. Sample drift was corrected by cross-correlation of the determined localized particles [123] or tracking of fiduciary markers. Fit results were stored as data lists for further analyses. The SRX software allows the three-dimensional display of localized particles as solid-shaded spheres or as an accumulation of transparent Gaussian kernels. However, as the selection criteria of virions required them to be coplanar with the glass, for most data analysis the two-dimensional projection into the XY plane was utilized. The three-dimensional volume in any of the three main directions can be shown, and was utilized for isosurfacing, but again, only the XY projection of the isosurface was utilized

in this analysis. For the purposes of this paper particles were colored according to probe type (eGFP, Alexa647).

A.2.4.1 fPALM Data Selection Criteria

There are several selection criteria for virions used in this study.

1) Only particles with >70% confidence (as determined by the Vutara software chi^2 minimization localization) are considered. This was to eliminate noise.
2) Both probes (Alexa 647 and eGFP) must have a clear signal that was visible in the data. This was typically seen in that both the green and red channels have an obvious particle to consider. This was to eliminate nonvirion particles as a virion should have both signals.
3) Virions had to have 70% or more of the frames in the eGFP data capture with a signal above 70% confidence.
4) Virions had to have 500 or more unique Alexa 647 particles as determined above. This was to ensure the virion had enough data to properly recover the surface via isosurfacing.
5) Virions with grossly abnormal sizes (200% larger than expected in any dimension) were eliminated from consideration. This typically eliminated virions that may have had too much surfactant nearby, which distorted the antibody labeling.

A.2.5 Isosurfacing Procedure

In order to better visualize localization data in terms of a recovered volume the mapping of the date to an isosurface was utilized. An isosurface S_a was defined as the preimage of a function

$$f: R^3 \rightarrow R \tag{A.1}$$

and value a. It is the set of points in the domain that map to a, i.e.,

$$S_a = \{x \; in \; R^3 | f(x) = a\} \tag{A.2}$$

[124]. A common use of isosurfaces was to visualize objects represented by an indicator function, where f evaluates to 1 for points inside the object and 0 for points outside, with a continuous transition in between where the classification may not be precise. S_a, a in (0,1) are then surfaces dividing the interior and exterior points, or showing the boundary of the object. However, these isosurfaces are difficult to visualize directly, so there was a need to convert them to triangle meshes that can be rendered interactively with consumer GPUs.

We represent the function (f) as a set of scalar values over a uniform grid in three dimensions. This volume was constructed by accumulating Gaussian splats for each localized particle location and radius, with the radius either user-specified or dependent on the accuracy of the localization. For each cell of the grid within a user-specified distance to the particle, we integrate the

three-dimensional Gaussian over the cell. After all of the localized points have been accumulated, we normalize the volume so that it is in the range [0,1], which simplifies the user selection of the value a. This results in a volume that was close to 1 where there are many localized particles, close to 0 where there are few, and intermediate isosurfaces will show the boundary of the object being imaged. Finally, we convert the isosurface to a triangle mesh for display using the fast, simple, and robust Marching Cubes algorithm [125]. All isosurfaces were matched to the full width at half maximum measurement from the fluorescent data in order to return that topology. This allows for the analysis to be created from data as opposed to arbitrary selection criteria.

A.2.6 Calculation of fPALM Localizations/Virion

For any given data collection utilizing fPALM, for the virions we imaged, it was typical to find 2000-3000 high confidence points (as determined by the Vutara software χ^2 minimization localization) for a virion. This was explained by the fact that a single Alexa647 can be active for more than one frame. Typically very strong particles will fluoresce for five or more frames in a row. To count actual particle counts, duplicate particles that share identical locations and neighboring frames are eliminated from consideration as unique particles. When this was done it was found that typically 800-1000 unique particles exist to create the volumes and do the analysis of the virions.

This indicates that 67-83% of the available surface VSV-G proteins were labeled with Alexa 647.

A.2.7 eGFP and Photo-Bleaching Calibration

Even though eGFP data was collected for 500 frames, it was found that the eGFP signals typically bleached during this collection. So, for all virions that were selected, the first 50 frames were utilized where the variation due to photo-bleaching was minimized. The data for those 50 frames were fit to a linear function and corrected for photo-bleaching by adding the slope for intensity over time back into the intensities.

A.2.8 Data Analysis and Normalization Methodologies

After selection, all eGFP signals were rotated such that the center of fluorescence for the fluorescence of the eGFP points and the center of fluorescence of the Alexa 647 points lay along the X axis using an $e^{i\theta}$ rotation about the Alexa647 center of fluorescence as a pivot point. All virions were rotated such that the eGFP was to the right of the Alexa647. This rotation demonstrated that the offset existed along the principal axis of the virion and that each of the three virion types had differing average offsets. Additionally, there was a variation in the intensity of eGFP for both the polymerase (L) and the phosphoprotein (P) intensities, as seen in Figures A.2, and A.3 respectively.

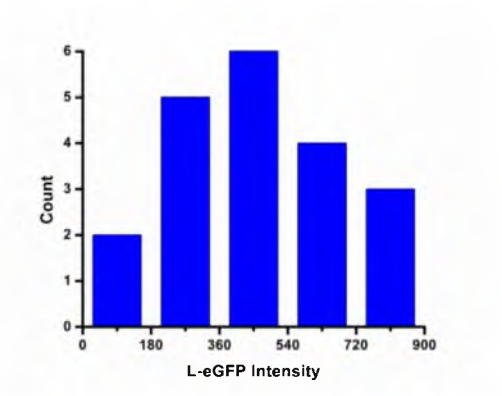

Figure A.2 Histogram of the intensity distributions for VSV L-eGFP.

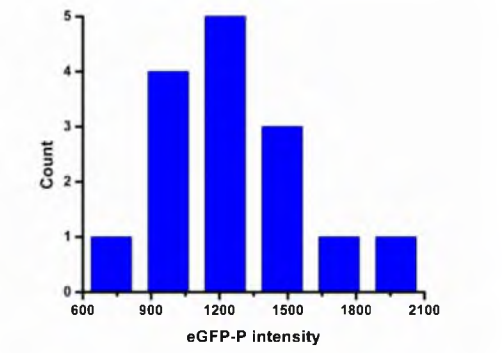

Figure A.3 Histogram of intensity distributions for VSV eGFP-P.

Alexa 647 center of fluorescence calculation, with respect to the topology of the VSV virion Calculation for the center of fluorescence of VSV virions was done considering an idealized virion modeled from cryo-EM data. We assumed that since the virion was coated on the exterior surface with antibodies and Alexa 647, that the center of fluorescence would be located at the point along the central axis where equal portions of surface area were located both above and below the point. It was also reasonable to assume this

was not the center point of the central axis as the tip has a different geometry from the base.

In modeling the idealized virion, the tip was modeled as half of a prolate ellipsoid, while the base was modeled as half of an oblate ellipsoid. The central shaft would consist of the radial wall of a cylinder. The surface areas for each of these geometries if *c* lies along the central shaft, and *a* lay in the radial direction would be:

$$S_{oblate} = \pi a^2 \left(1 + \frac{1 - e_o^2}{e_o} \tanh^{-1} e_o\right) \; where \;\; e_o^2 = 1 - \frac{c^2}{a^2} \; and \;\; (c < a) \tag{A.3}$$

$$S_{prolate} = \pi a^2 \left(1 + \frac{c}{a e_p} \sin^{-1} e_p\right) \; where \; e_p^2 = 1 - \frac{a^2}{c'^2} \;\; and \;\; (c' > a) \tag{A.4}$$

$$S_{shaft} = 2\pi ab \quad and \quad b = l - (c + c') \tag{A.5}$$

where *l* is the length of virion's central axis. We wish to find the center of fluorescence which correlates directly with the center of the surface area along the central axis. Thus we can use the relation:

$$S_{oblate} + 2\pi ad = S_{prolate} + 2\pi a(b - d) \tag{A.6}$$

where d + c were the distance from the base of the virion to the center of fluorescence, thus *d* was the distance within the cylindrical shaft from the top of the oblate region. Letting *l* = 210 nm (due to extension of the viral length by the addition of the primary and secondary antibodies ~15nm on each end,

~30nm in total),*a*=55 nm, c=40 nm and c'=88 nm, we find that the center of mass for the surface of the virion was 104.6 nm from the bottom of the base. This was 0.4 nm closer to the base than the physical center of the principle axis and was effectively the same as center.

A.2.9 HIV Co-Localization Control Experiment

To confirm our ability to determine colocalization of eGFP signal within a viral envelope, we tested VSV-G pseudo-typed HIV virus-like particles (VLP), in which a portion of HIV-Gag is tagged with eGFP. To image HIV VLPs, the same protocols for VSV experiments were used. For HIV VLPs, both Gag and VSV-G should be evenly distributed within the envelope and the signals are expected to colocalize. We observed a small shift of 12 nm ± 6 nm which was within our 20nm positional uncertainty (Table A.2). When comparing the intensity to the offset, we see that there was a low correlation between offset and intensity (Figure. A.4).

A.2.9.1 HIV-1 VLP Purification

HIV-1 VLPs pseudo-typed with VSV-G were produced in 293T cells (3×10^6 cells in 100 mm plates) by cotransfection (Fugene-HD, Roche) of the following plasmids: 7.5 μg of HIV-1 Gag (11-071), 1.5 μg HIV-1 Gag-eGFP

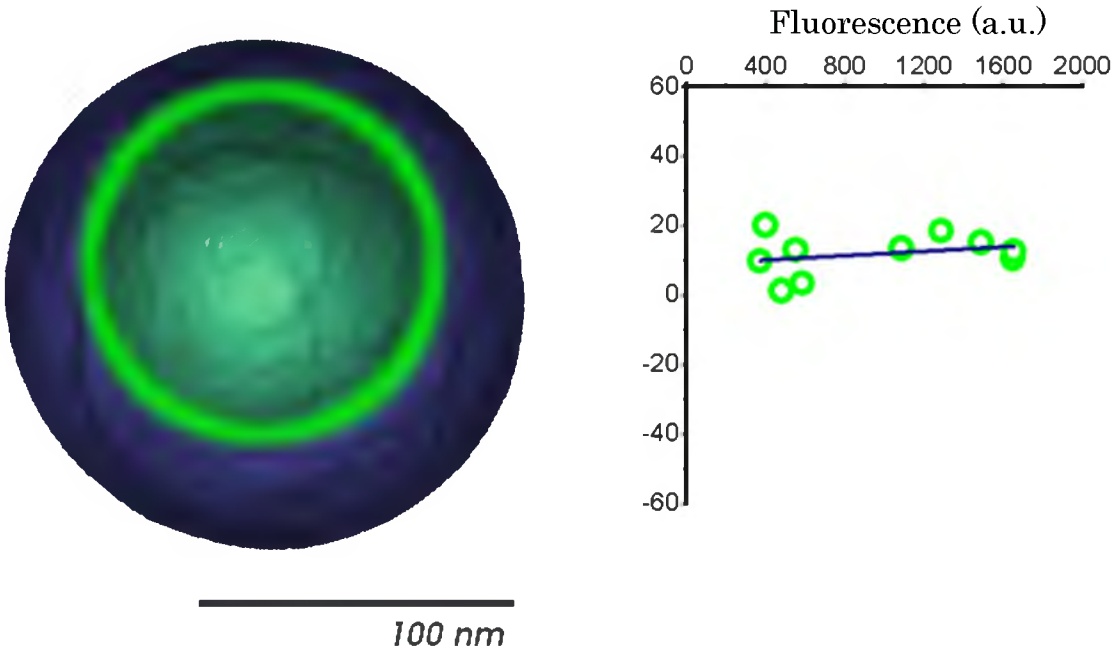

Figure A.4 HIV-1 VLP fluorescence control. Shown on left: An isosurface of the colocalization of pseudo-typed HIV GAG eGFP with VSVG and Alexa 647. Shown on right: GFP intensity vs. Offset which shows a low correlation (R^2 = 0.0798) between the two when fit linearly.

(11-075) and 2.4 µg VSV-G (11-041). The medium was replaced 8 hours after transfection, and the supernatant was harvested 32 hours later and syringe-filtered through 0.45 µm membranes. VLPs were collected by pelleting 5 mL of the filtered medium through a 1 ml 20% sucrose in PBS cushion (centrifuge, 4°C, 2 hour, 40,000 RPM). The supernatant was removed and the pellet was resuspended in 500 µL NTE (10 mMTris–HCl, pH 7.4, 100

mMNaCl, 1 mM EDTA). To remove residual sucrose before imaging, the virus sample was treated by dialysis (Slide-A-Lyzer, mini dialysis unit; 10,000 MWCO, Thermo Scientific) at 4°C against NTE plus 10 mM HEPES.

A.2.9.2 VSV:G-eGFP Preparation

Two nine three cells were plated a day before experiments and transfected using (Fugene-HD, Roche) with VSVG-eGFP plasmid. Cells were then infected with VSV WT 12 hours after transfection with an MOI of 3. Supernatant was collected 24 hours after infection and VSV virions were purified as described under virus preparation.

A.3 AFM Materials and Methods

We used atomic force microscopy (AFM) to map variations in elasticity across the surface of several virions [20]. The AFM (Asylum Research) consists of a pyramidal gold-coated tip (radius of curvature ≃20 nm; height ≃10 μm) attached to the underside of a pliable cantilever (force constant $\simeq 3N/m$; length = 200 μm), a piezo-electrically actuated sample scanner (<1 nm precision), and associated digital control and data acquisition electronics. The AFM control system dictates that the upward force on the tip from compression of the sample must balance the downward restoring force from the loaded cantilever. On stiff samples, therefore, the AFM cantilever bends easily to accommodate changes in the sample height, so the path of the tip

faithfully reports sample topography. When the sample is more pliant than the cantilever, however, the sample will deform under the force of the tip, so the height signal becomes more indicative of the sample's stiffness rather than its topography. More compliant regions of the sample (i.e., those with low Young's moduli) must be locally compressed more to achieve the required force balance on the tip, and will appear to be lower in height [21]. In the soft-sample limit, therefore, the height signal provides an isoforce map of the sample surface rather than a true topographical map.

The threshold for the isoforce was determined experimentally based on the condition that repeated scans of the virion will return nearly identical results. This gives us an isoforce regime that would consistently preserve virion integrity without breaking its elastic limit, thus remaining in the linear elasticity regime [126]. This regime had sufficient force to reveal the variance in Young's modulus. Settings are discussed later in the Appendix A materials.

All Young's modulus accuracy considerations for this AFM assay are from along the central axis. This region corresponds to the highest points along the axis of the virion and thus the region of lowest tip convolution, which is typically near zero. Additionally, this location is a normal surface facing to the incoming compression force, viz. the force calculation being tangential to the curvature of the virion. Correspondingly, a normal force indentation

analysis applies [127]. The only distortion when determining the elasticity comes from compression [20,21,126,127].

Using this technique, we have performed measurements on VSV virions. As shown in Figure. 2.3 of Chapter 2, we observed virions with clear 80×180 nm bullet shapes, each with recognizable tapered and blunt ends. The measured height of the virions was on average ~30 nm due to compression of the soft virus under the tip, as described above. The tapered end of the virion exhibited a very small region of slightly higher stiffness due to the reinforcement of the conical shape by the M-bound N-RNA underneath. A larger region of variable length at the blunt end of the virion exhibits higher stiffness, as shown in blue. This region extends 57 ± 12 nm in length from the blunt end for WT virions, measured on a sample of 50 WT and 68 ±21 nm for 30 VSV: eGFP-P virions.

All our experiments were done in tapping (AC) mode in ambient condition. The data were obtained using an Asylum MFP-3D in a dark environmental chamber. The AFM probes we used were gold-coated tips on silicon chips. These probes are designed for applications like force modulation, light tapping. Since there was a significant (three orders of magnitude) difference in the Young's modulus between the virion and the gold tip, the gold tip being greater, we opted for the superior signal of the gold tip over a silicon nitride tip. When scanning in AC mode, the height profile was a constant force topography, which allows for topological observation of variation in Young's

modulus. Tapping mode was done at +5% of the resonant frequency using a typical drive amplitude of 600 mV with an initial set point of 480 mV. Using the standard method for force calculation and K calculation we see that:

$$K_{effective} = \sqrt{\frac{F^2}{h^3 R}} \tag{A.7}$$

where R is

$$R = \left(\frac{1}{r} + \frac{1}{r'}\right)^{-1} \tag{A.8}$$

where r = 25nm was the radius of the tip, and r'= 40nm was the radius of the virion thus R=15.4nm.This results in a ratio for h/h' = 1.15, thus $K'_{effective} / K_{effective}$ = 1.23 +/- 0.13 for the two distinct regions along the WT virion. No correlation was found to exist between the $K'_{effective} / K_{effective}$ ratio and the length of the virion for any of the tested virion types (See Figure A.5).

A.3.1 AFM Information

- Atomic Force Microscope (model): Asylum MFP-3D
- Software version: 101010+1725
- Mode of scan: AC air topography

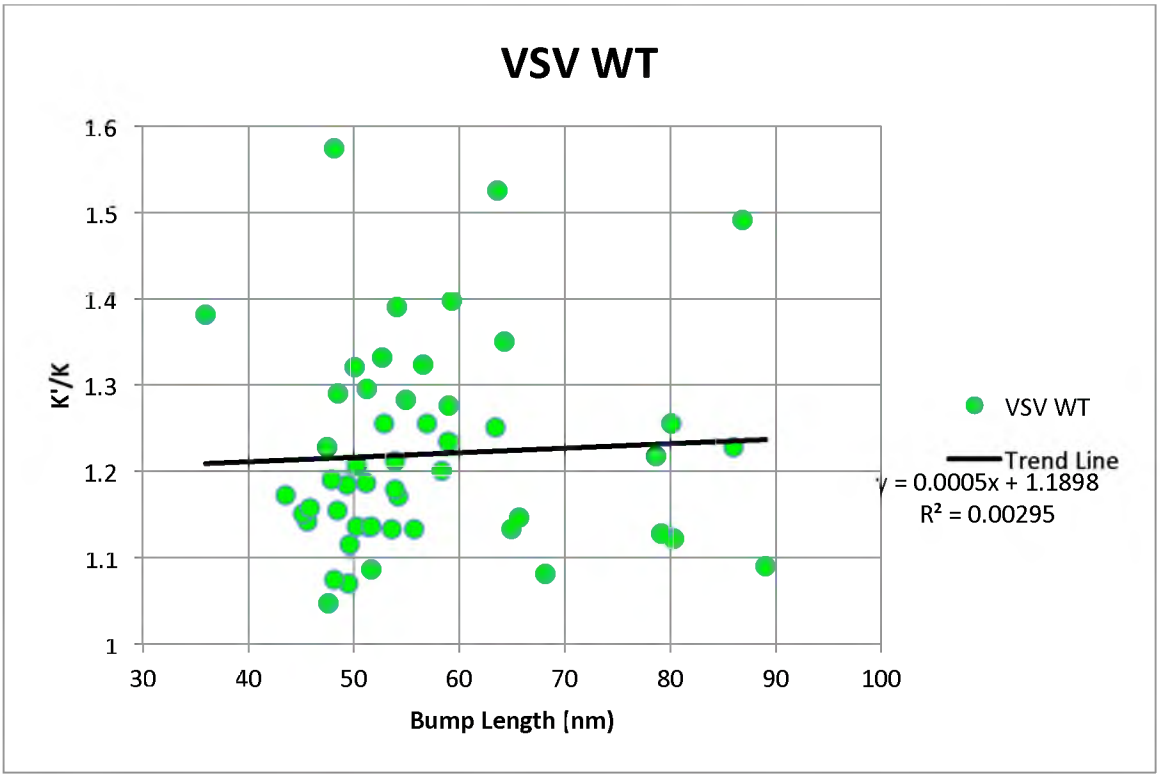

Figure A.5 Scatter plot of the relationship between K'/K and bump length showing there is no correlation ($R^2 = 0.003$).

A.3.2 Tip Information

- All the data we took using Budget Sensors probes (Multi75GB) .
- Gold Plated Silicon Nitride
- Tip radius <25nm
- Application: force modulation, light tapping.
- Force constant: 3N/m.
- Resonant frequency 75 KHz with uncertainty of 15 KHz

A.3.3 AFM Sample Preparation

Sample preparation for AFM was identical to fPALM sample preparation except AFM coverslips (AFM: Fisherbrand Microscope Cover Glass: 35 CIRCLE #1) were used. For the sandwich method, AFM coverslips required 40μL of fluid during each stage. AFM sample preparation was complete after virus laydown.

A.3.4 Blunt End Versus Tip Identification

AFM data are captured using an isoforce method maintaining the virion in an elastic region as shown in Figure A.6. These scans were used to deconvolve the virion surface based on the numerical deconvolution [20,21,126,127]. This deconvolution is justified in the regions of the bump and main body due to their linear nature (Figure A.6D).

Identification of the tapered end vs. blunt end of VSV virions in both wild type (WT) and P-eGFP mutants was accomplished by analyzing the curvature of the deconvolved scans, these curvatures showed a clear prolate region identifying the tip of the virion. We determined this by considering only the top half of the normalized curves in order to calculate ellipticity, all curves were fit with a sixth power polynomial function (with $R^2 > 0.999$ in all cases), and these fits can be categorized into two distinct groups of prolate (where the first plateau > 40nm) or oblate (where the first plateau < 40nm) ellipsoidal topology. In this idealized model, we note that the conventionally

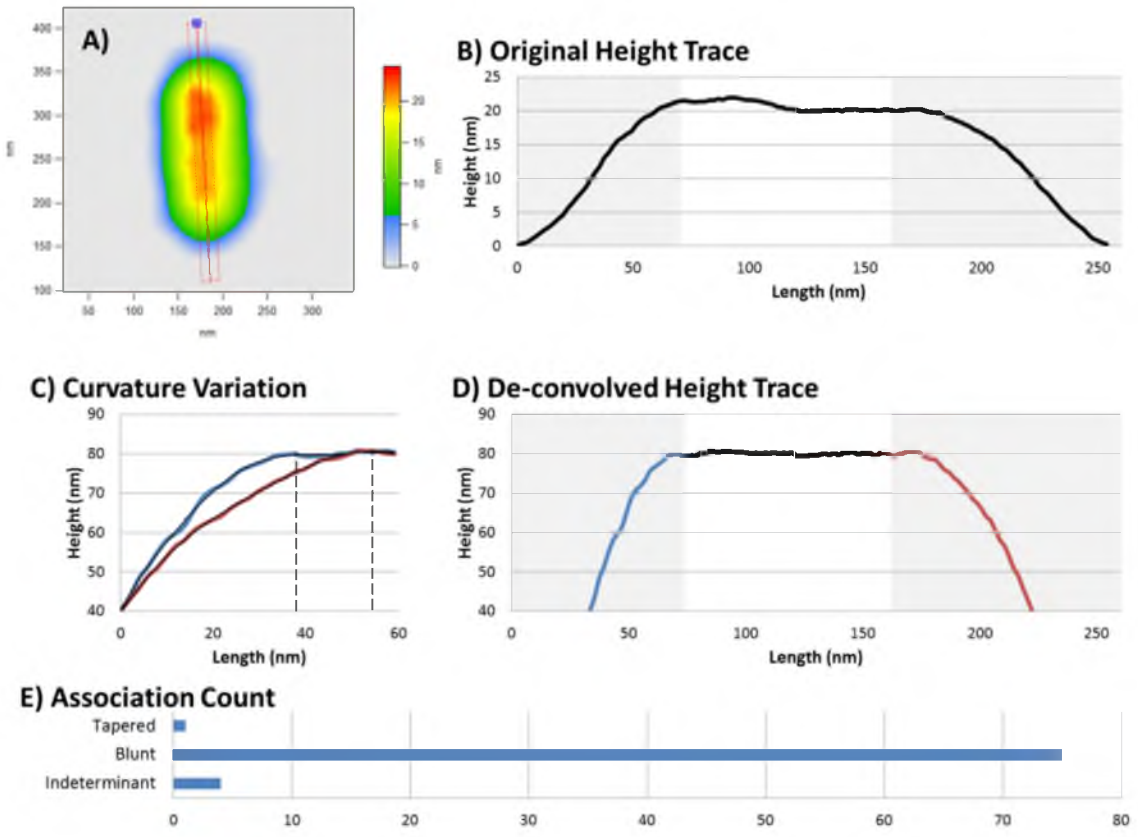

Figure A.6 AFM analysis of a typical VSV wild type virus. Deconvolution analysis for virions was accomplished by analyzing the central axis A). In this region there is little or no XY convolution due to the tip. The only convolution is in Z, B) where the virion is compressed to its lowest point. The both the original compression and the deconvolved height trace D) show that there is a significant variance in curvature from one side to the other, and when compared C) one curvature is distinctly prolate and is associated with the tapered end of the virion. When we associate the bump with the curvature E) we find that the bump is most commonly associated with the blunt end of the virion.

rounded tip of VSV is described as prolate, while the blunt end can be described as oblate.

The position of the bump which identified with the super complex was then scored versus the oblate or prolate geometry and 75 out of 80 virions analyzed showed the bump associated with the oblate geometry, one case had the bump associated with the prolate side of the virion and in 4 cases the oblate and prolate curvatures were difficult to distinguish. This data strongly correlates the presence of the bump associated with the protein concentration at the blunt end of the virus.

A.3.5 Super-Complex Distribution Analysis

The relationship between the center of fluorescence and number of P proteins packaged within each virion is linear as shown in Figure 2.2 of the Chapter 2. The simplest model that can explain these data was to assume that the protein concentration has a constant density and varies in length depending on the number of L-P units packaged within the virion. In order to eliminate the possibility that P proteins bind within the central cavity aside from the protein concentration, we have used center of mass calculations to set a limit on the maximum number of P proteins that can be uniformly distributed within the cavity and found this limit to be below 5%.

In our calculations the maximum number of P proteins could be uniformly distributed only if the remaining P's were forming a very high density protein

concentration at the blunt end. The higher the density at the blunt end, the larger the fraction of uniformly bound P's that could accommodate the measured center of mass of the P proteins. We used the maximum protein density of 1.35 gm/cm^3 for the portion of the P proteins within the protein concentration and this way generated the maximum fraction of the P proteins uniformly distributed.

For the average virion, there are ~400 P proteins; the center of mass is offset by 55nm from the center of the virion. Assuming a protein concentration with a density of 1.35, this complex will be 45nm long which will restrict the available P for uniform binding to 1.08% of the total P proteins. We have obtained slightly higher fractions up to 5% for the virions which package substantially more P proteins, however, the ratio has never been over 5% of the total P proteins that can be uniformly distributed.

REFERENCES

[1] E.R. Harrison, Masks of the Universe: Changing Ideas on the Nature of the Cosmos, Cambridge University Press, Cambridge, UK; New York, (2003).

[2] M.T. Madigan, J.M. Martinko, D.A. Stahl, D.P. Clark, Brock Biology of Microorganisms, 13 ed., Benjamin Cummings, (2010).

[3] J.R. Lakowicz, Principles of Fluorescent Spectroscopy, 3 ed., Springer, New York, (2006).

[4] L. de Broigle, Recherches sur la Théorie des Quanta (Researches on the Quantum Theory), Physics, Sorbonne, Paris, (1924).

[5] D.E.R. Chandler, Robert W. Roberson, Bioimaging: Current Concepts in Light and Electron Microscopy, 1 ed., Jones and Bartlett publishers, (2009).

[6] E. Abbe, Beitrage zur Theorie des Mikroskops und der Mikroskopischen Wahrmehmung, Archiv für Mikroskopische Anatomie 9 (1873) 413-420.

[7] R.E. Thompson, D.R. Larson, W.W. Webb, Precise Nanometer Localization Analysis for Individual Fluorescent Probes, Biophys. J. 82 (2002) 2775-2783.

[8] G.G. Stokes, On the Change of Refrangibility of Light, Philosophical Transactions of the Royal Society of London (1852) 463-562.

[9] E. Betzig, G.H. Patterson, R. Sougrat, O.W. Lindwasser, S. Olenych, J.S. Bonifacino, M.W. Davidson, J. Lippincott-Schwartz, H.F. Hess, Imaging Intracellular Fluorescent Proteins at Nanometer Resolution, Science 313 (2006) 1642-1645.

[10] S.T. Hess, T.P.K. Girirajan, M.D. Mason, Ultra-High Resolution Imaging by Fluorescence Photoactivation Localization Microscopy, Biophys. J. 91 (2006) 4258-4272.

[11] M.J. Rust, M. Bates, X.W. Zhuang, Sub-Diffraction-Limit Imaging by Stochastic Optical Reconstruction Microscopy (STORM), Nature Methods 3 (2006) 793-795.

[12] S.W.W. Hell, Jan, Breaking the Diffraction Resolution Limit by Stimulated Emission: Stimulated-Emission-Depletion Fluorescence Microscopy, Optics Letters 19 (1994) 780-782.

[13] J.E. Lennard-Jones, On the Determination of Molecular Fields, Proc. R. Soc. Lond. A 106 (1924) 463-477.

[14] G.Q. Binning, CF; Gerber, Ch, Atomic Force Microscope, Phys. Rev. Letters 56 (1986) 930-933.

[15] H.R. G. Binnig, C. Gerber, E. Weibel, Surface Studies by Scanning Tunneling Microscopy, Phys. Rev. Lett. 49 (1983) 57-61.

[16] A. Ortega-Esteban, I. Horcas, M. Hernando-Pérez, P. Ares, A.J. Pérez-Berná, C. San Martín, J.L. Carrascosa, P.J. de Pablo, J. Gómez-Herrero, Minimizing Tip–Sample Forces in Jumping Mode Atomic Force Microscopy in Liquid, Ultramicroscopy 114 (2012) 56-61.

[17] A. Ortega-Esteban, A.J. Perez-Berna, R. Menendez-Conejero, S.J. Flint, C.S. Martin, P.J. de Pablo, Monitoring Dynamics of Human Adenovirus Disassembly Induced by Mechanical Fatigue, Sci. Rep. 3 (2013).

[18] M. Hernando-Pérez, R. Miranda, M. Aznar, J.L. Carrascosa, I.A.T. Schaap, D. Reguera, P.J. de Pablo, Physical Virology: Direct Measurement of Phage phi29 Stiffness Provides Evidence of Internal Pressure (Small 15/2012), Small 8 (2012) 2365-2365.

[19] C. Carrasco, A. Carreira, I.A.T. Schaap, P.A. Serena, J. Gómez-Herrero, M.G. Mateu, P.J. de Pablo, DNA-Mediated Anisotropic Mechanical Reinforcement of a Virus, Proceedings of the National Academy of Sciences 103 (2006) 13706-13711.

[20] K.L. Johnson, Contact mechanics, Cambridge University Press, (1985).

[21] V.L. Popov, Contact Mechanics and Friction: Physical Principles and Applications, Springer Heidelberg, New York, (2002).

[22] S.P.P.M.W. Davidson, The Photoactivated Localization Microscopy (PALM) Concept, Zeiss, (2013).

[23] A. Neice, Methods and Limitations of Subwavelength Imaging, 1 ed., Academic Press, (2010).

[24] L.S.C. K. I. Mortensen, J. A. Spudich and H. Flyvbjerg, Optimized Localization Analysis for Single-Molecule Tracking and Super-Resolution Microscopy, Nature Methods 7 (2010) 377–381.

[25] M.M.B. Rust, X. Zhuang, Sub-Diffraction-Limit Imaging by Stochastic Optical Reconstruction Microscopy (STORM), Nature Methods 3 (2006) 793–796.

[26] B.H. M Bates, GT Dempsey, X Zhuang, Multicolor Super Resolution Imaging with Photo-Switchable Fluorescent Probes, Science 317 (2007) 1749–1753.

[27] B.S.J. Huang, B. Brandenburg, X. Zhuang Whole Cell 3D STORM Reveals Interactions Between Cellular Structures with Nanometer-Scale Resolution, Nature Methods 5 (2008) 1047-1052.

[28] B. Huang, W. Wang, M. Bates, X. Zhuang, Three-Dimensional Super-Resolution Imaging by Stochastic Optical Reconstruction Microscopy, Science 319 (2008) 810-813.

[29] X. Zhuang, Nano-Imaging With Storm, Nat Photonics 3 (2009) 365-367.

[30] M.F. Juette, T.J. Gould, M.D. Lessard, M.J. Mlodzianoski, B.S. Nagpure, B.T. Bennett, S.T. Hess, J. Bewersdorf, Three-Dimensional Sub-100 nm Resolution Fluorescence Microscopy of Thick Samples, Nat Meth 5 (2008) 527-529.

[31] T.J.G. M.F. Juette, M.D. Lessard, M.J. Mlodzianoski, B.S. Nagpure, B.T. Bennett, S.T. Hess, J.Bewersdorf Experimental Characterization of 3D Localization Techniques for Particle-Tracking and Super-Resolution Microscopy, Optics Express 17 (2009) 8264-8277.

[32] D. Axelrod, Cell-Substrate Contacts Illuminated by Total Internal Reflection Fluorescence, The Journal of Cell Biology 89 (1981) 141-145.

[33] D. Axelrod, Total Internal Reflection Fluorescence Microscopy in Cell Biology, Biophotonics, Pt B, (2003) 1-33.

[34] L.H. Novotny, Bert Principles of Nano-Optics, Cambridge University Press, Cambridge, (2006).

[35] S.J. Russell, K.W. Peng, J.C. Bell, Oncolytic Virotherapy, Nature Biotechnology 30 (2012) 658-670.

[36] Z.X. Cronin J, Reiser J., Altering the Tropism of Lentiviral Vectors Through Pseudotyping., Curr Gene Ther. 5 (2005) 387-398.

[37] M.S. Green TJ, Qiu S, Lebowitz J, Wertz GW, Luo M., Study of the Assembly of Vesicular Stomatitis Virus N Protein: Role of the P Protein., J Virol. 74 (2000) 9515-9524.

[38] P. Ge, J. Tsao, S. Schein, T.J. Green, M. Luo, Z.H. Zhou, Cryo-EM Model of the Bullet-Shaped Vesicular Stomatitis Virus, Science 327 (2010) 689-693.

[39] C.W. Naeve, D.F. Summers, Electron Microscopy of Vesicular Stomatitis Virus Replicative Ribonucleoproteins, Journal of Virology 34 (1980) 764-771.

[40] W.A. Finkelshtein D, Novick D, Barak S, Rubinstein M., LDL Receptor and its Family Members Serve as the Cellular Receptors for Vesicular Stomatitis Virus., Proc Natl Acad Sci U S A. 110 (2013) 7306-7311.

[41] A.A. Libersou S, Ouldali M, Maury V, Maheu C, Raux H, de Haas F, Roche S, Gaudin Y, Lepault J., Distinct Structural Rearrangements of the VSV Glycoprotein Drive Membrane Fusion, J Cell Biol. 191 (2010) 199-210.

[42] W.F. Mebatsion T, Conzelmann KK., Matrix Protein of Rabies Virus is Responsible for the Assembly and Budding of Bullet-Shaped Particles and Interacts with the Transmembrane Spike Glycoprotein G., J Virol. 73 (1999) 242-250.

[43] T.J. Green, X. Zhang, G.W. Wertz, M. Luo, Structure of the Vesicular Stomatitis Virus Nucleoprotein-RNA Complex, Science 313 (2006) 357-360.

[44] C.T. Ruigrok RW, Kolakofsky D., Nucleoproteins and Nucleocapsids of Negative-Strand RNA Viruses., Curr Opin Microbiol 14 (2011) 504-510.

[45] A.T. Gentile M, Scheidler A, Ewald M, Dianzani F, Pauli G, Gelderblom HR., Determination of the Size of HIV Using Adenovirus Type 2 as an Internal Length Marker., J Virol Methods. 48 (1994) 43-52.

[46] D.D. Ho, A. U. Neumann,A. S. Perelson,W. Chen,J. M. Leonard and M., Markowitz, Rapid Turnover of Plasma Virions and CD4 Lymphocytes in HIV-1 Infection., Nature 373 (1995) 123-126.

[47] R. Weiss, How Does HIV Cause AIDS?, Science 260 (1993) 1273-1279.

[48] W.I. Sundquist, H.-G. Kräusslich, HIV-1 Assembly, Budding, and Maturation, Cold Spring Harbor Perspectives in Medicine 2 (2012).

[49] L.-A. Carlson, J.A.G. Briggs, B. Glass, J.D. Riches, M.N. Simon, M.C. Johnson, B. Müller, K. Grünewald, H.-G. Kräusslich, Three-Dimensional Analysis of Budding Sites and Released Virus Suggests a Revised Model for HIV-1 Morphogenesis, Cell Host; Microbe 4 (2008) 592-599.

[50] F.E. Adamson CS, Human Immunodeficiency Virus Type 1 Assembly, Release, and Maturation., Adv Pharmacol. (2007) 347-387.

[51] T. Watanabe, S. Watanabe, H. Ito, H. Kida, Y. Kawaoka, Influenza A Virus Can Undergo Multiple Cycles of Replication Without M2 Ion Channel Activity, Journal of Virology 75 (2001) 5656-5662.

[52] M. Takeda, A. Pekosz, K. Shuck, L.H. Pinto, R.A. Lamb, Influenza A Virus M2 Ion Channel Activity is Essential for Efficient Replication in Tissue Culture, Journal of Virology 76 (2002) 1391-1399.

[53] L.H. Pinto, R.A. Lamb, The M2 Proton Channels of Influenza A and B Viruses, Journal of Biological Chemistry 281 (2006) 8997-9000.

[54] T. Ivanovic, R. Rozendaal, D.L. Floyd, M. Popovic, A.M. van Oijen, S.C. Harrison, Kinetics of Proton Transport into Influenza Virions by the Viral M2 Channel, PLoS ONE 7 (2012) e31566.

[55] M. Bretscher, Asymmetrical Lipid Bilayer Structure for Biological Membranes, Nature Biotechnology 236 (1972) 11-12.

[56] R.B. Bell, LM; Coleman, RA Lipid Topogenesis, J. Lipid Res. 22 (1981) 391-403.

[57] B.J. Alberts, A; Lewis, J, Molecular Biology of the Cell, Garland Science, New York, (2002).

[58] P.M. Hauser H, Stubbs M Ion Permeability of Phospholipid Bilayers, Nature Biotechnology 239 (1972) 342-344.

[59] A. Jablonski, Uber den Mechanisms des Photolumineszenz von Farbstoffphosphoren, Z phys. (1935) 38-46.

[60] M.K. Prendergast F, Chemical and physical Properties of Aequorin and the Green Fluorescent Protein Isolated from Aequorea Forskålea, Biochemistry 17 (1978) 3448-3453.

[61] J.F. Shimomura O, Saiga Y Extraction, Purification and Properties of Aequorin, a Bioluminescent Protein from the Luminous Hydromedusan, Aequorea, J Cell Comp Physiol 59 (1962) 223-239.

[62] C.A. Ormö M, Kallio K, Gross L, Tsien R, Remington S Crystal structure of the Aequorea Victoria Green Fluorescent Protein, Science 273 (1996) 1392-1395.

[63] R. Tsien, The Green Fluorescent Protein, Annu Rev Biochem (1998) 509-544.

[64] C.A. Heim R, Tsien R, Improved Green Fluorescence, Nature Biotechnology 373 (1995) 663-664.

[65] S.O. Morise H, Johnson F, Winant J Intermolecular Energy Transfer in the Bioluminescent System of Aequorea, Biochemistry 13 (1974) 2656-2662.

[66] T.V. Nifosì R, Molecular Dynamics Simulations of Enhanced Green Fluorescent Proteins: Effects of F64L, S65T and T203Y Mutations on the Ground-State Proton Equilibria., Proteins 51 (2003) 378-389.

[67] L.J. Kricka, Chemiluminescent and Bioluminescent Methods in Analytical Chemistry. A review, Analyst 108 (1983) 1274-1296.

[68] M. Kneen, J. Farinas, Y. Li, and A. S. Verkman, Green Fluorescent Protein as a Noninvasive Intracellular pH Indicator., Biophys J. (1998) 1591-1599.

[69] D.A.D. Miesenböck G, Rothman JE., Visualizing Secretion and Synaptic Transmission with pH-sensitive Green Fluorescent Proteins., Nature Biotechnology 394 (1998) 192-195.

[70] G. Miesenbock, D.A. De Angelis, J.E. Rothman, Visualizing Secretion and Synaptic Transmission with pH-sensitive Green Fluorescent Proteins, Nature 394 (1998) 192-195.

[71] D.C. Prosser, K. Whitworth, B. Wendland, Quantitative Analysis of Endocytosis with Cytoplasmic pHluorin Chimeras, Traffic 11 (2010) 1141-1150.

[72] Y.G. Kuznetsov, A. McPherson, Atomic Force Microscopy in Imaging of Viruses and Virus-Infected Cells, Microbiology and Molecular Biology Reviews 75 (2011) 268-285.

[73] N. Kol, Y. Shi, M. Tsvitov, D. Barlam, R.Z. Shneck, M.S. Kay, I. Rousso, A Stiffness Switch in Human Immunodeficiency Virus, Biophysical Journal 92 (2007) 1777-1783.

[74] R.P. Milagros Castellanos, Carolina Carrasco, Mercedes Hernando-Pérez, Julio Gómez-Herrero, Pedro J. de Pablo, Mauricio G. Mateu, Mechanical Elasticity as a Physical Signature of Conformational Dynamics in a Virus Particle, PNAS 109 (2012) 12028-12033.

[75] D.L.J.H. Elbert, Surface Treatments of Polymers for Biocompatibility, Annual Review of Materials Science. 26 (1996) 365-370.

[76] J.M.S.Z. Harris, (Ed.), Poly(ethylene glycol), American Chemical Society, Washington, DC, (1997).

[77] T.D. M. Heuberger, and N. D. Spencer, Interaction Forces and Morphology of a Protein-Resistant Poly(ethylene glycol) Layer, Biophys. J. 88 (2005) 495-504.

[78] I. Szleifer, Polymers and Proteins: Interactions at Interfaces., Curr. Opin. Colloid Interface Sci. 2 (1997) 337-344.

[79] N. Green, Avidin. 1. The Use of (14-C)Biotin for Kinetic Studies and for Assay, The Biochemical Journal 89 (1963) 585-591.

[80] A. Desfosses, E.A. Ribeiro, G. Schoehn, D. Blondel, D. Guilligay, M. Jamin, R.W.H. Ruigrok, I. Gutsche, Self-organization of the Vesicular Stomatitis Virus Nucleocapsid into a Bullet Shape, Nat Commun 4 (2013) 1429.

[81] I. Ivanov, F. Yabukarski, R.W.H. Ruigrok, M. Jamin, Structural Insights into the Rhabdovirus Transcription/Replication Complex, Virus Research 162 (2011) 126-137.

[82] H.R. Jayakar, E. Jeetendra, M.A. Whitt, Rhabdovirus Assembly and Budding, Virus Research 106 (2004) 117-132.

[83] B. Morin, P.J. Kranzusch, A.A. Rahmeh, S.P.J. Whelan, The Polymerase of Negative-Stranded RNA Viruses, Current Opinion in Virology 3 (2013) 103-110.

[84] A.A. Rahmeh, B. Morin, A.D. Schenk, B. Liang, B.S. Heinrich, V. Brusic, T. Walz, S.P.J. Whelan, Critical Phosphoprotein Elements that Regulate Polymerase Architecture and Function in Vesicular Stomatitis Virus, Proc. Natl. Acad. Sci. U.S.A. 109 (2012) 14628-14633.

[85] A.A. Rahmeh, A.D. Schenk, E.I. Danek, P.J. Kranzusch, B. Liang, T. Walz, S.P.J. Whelan, Molecular Architecture of the Vesicular Stomatitis Virus RNA polymerase, Proc. Natl. Acad. Sci. U.S.A. 107 (2010) 20075-20080.

[86] H. Ding, T.J. Green, S. Lu, M. Luo, Crystal Structure of the Oligomerization Domain of the Phosphoprotein of Vesicular Stomatitis Virus, Journal of Virology 80 (2006) 2808-2814.

[87] I. Ivanov, T. Crépin, M. Jamin, R.W.H. Ruigrok, Structure of the Dimerization Domain of the Rabies Virus Phosphoprotein, Journal of Virology 84 (2010) 3707-3710.

[88] M. Kaksonen, D.G. Drubin, PALM reading: Seeing the Future of Cell Biology at Higher Resolution, Developmental Cell 11 (2006) 438-439.

[89] J. Snijder, V.S. Reddy, E.R. May, W.H. Roos, G.R. Nemerow, G.J.L. Wuite, Integrin and Defensin Modulate the Mechanical Properties of Adenovirus, Journal of Virology 87 (2013) 2756-2766.

[90] L.E. Iverson, J.K. Rose, Localized Attenuation and Discontinuous Synthesis During Vesicular Stomatitis Virus Transcription, cell 23 (1981) 477-484.

[91] S.P.J. Whelan, G.W. Wertz, Transcription and Replication Initiate at Separate Sites on the Vesicular Stomatitis Virus Genome, Proc Natl Acad Sci USA 99 (2002) 9178-9183.

[92] D.H. Schott, D.K. Cureton, S.P. Whelan, C.P. Hunter, An Antiviral Role for the RNA Interference Machinery in Caenorhabditis Elegans, Proc. Natl. Acad. Sci. U.S.A. 102 (2005) 18420-18424.

[93] J.B. Ruedas, J. Perrault, Insertion of Enhanced Green Fluorescent Protein in a Hinge Region of Vesicular Stomatitis Virus L Polymerase Protein Creates a Temperature-Sensitive Virus That Displays No Virion-Associated Polymerase Activity In Vitro, J. Virol. 83 (2009) 12241-12252.

[94] J.A.G. Briggs, H.-G. Kräusslich, The Molecular Architecture of HIV, Journal of Molecular Biology 410 (2011) 491-500.

[95] H.-B. Pang, L. Hevroni, N. Kol, D. Eckert, M. Tsvitov, M. Kay, I. Rousso, Virion Stiffness Regulates Immature HIV-1 Entry, Retrovirology 10 (2013) 4.

[96] S.C. Das, A.K. Pattnaik, Role of the Hypervariable Hinge Region of Phosphoprotein P of Vesicular Stomatitis Virus in Viral RNA Synthesis and Assembly of Infectious Virus Particles, J. Virol. 79 (2005) 8101-8112.

[97] N. Jouvenet, M. Zhadina, P.D. Bieniasz, S.M. Simon, Dynamics of ESCRT Protein Recruitment During Retroviral Assembly, Nat Cell Biol 13 (2011) 394-401.

[98] C.L. Kuyper, J.S. Kuo, S.A. Mutch, D.T. Chiu, Proton Permeation into Single Vesicles Occurs via a Sequential Two-Step Mechanism and is Heterogeneous, Journal of the American Chemical Society 128 (2006) 3233-3240.

[99] S.D. Paula, D. W. Deamer, (Ed.), Membrane Permeability Barriers to Ionic and Polar Solutes, Academic Press, Burlington, MA., (1999).

[100] S. Paula, A.G. Volkov, A.N. VanHoek, T.H. Haines, D.W. Deamer, Permeation of Protons, Potassium ions, and Small Polar Molecules Through Phospholipid Bilayers as a Function of Membrane Thickness, Biophysical Journal 70 (1996) 339-348.

[101] S. Sankaranarayanan, D. De Angelis, J.E. Rothman, T.A. Ryan, The Use of pHluorins for Optical Measurements of Presynaptic Activity, Biophysical Journal 79 (2000) 2199-2208.

[102] N. Nelson, Structure and Function of V-ATPases in Endocytic and Secretory Organelles, Journal of Experimental Biology 172 (1992) 149-153.

[103] C.E. Mire, D. Dube, S.E. Delos, J.M. White, M.A. Whitt, Glycoprotein-Dependent Acidification of Vesicular Stomatitis Virus Enhances Release of Matrix Protein, Journal of Virology 83 (2009) 12139-12150.

[104] S. Roche, S. Bressanelli, F.A. Rey, Y. Gaudin, Crystal Structure of the Low-pH Form of the Vesicular Stomatitis Virus Glycoprotein G, Science 313 (2006) 187-191.

[105] A.A.V. Albertini, E. Baquero, A. Ferlin, Y. Gaudin, Molecular and Cellular Aspects of Rhabdovirus Entry, Viruses 4 (2012) 117-139.

[106] F. Käsermann, C. Kempf, Low pH-Induced Pore Formation by Spike Proteins of Enveloped Viruses, Journal of General Virology 77 (1996) 3025-3032.

[107] N. Jouvenet, P.D. Bieniasz, S.M. Simon, Imaging the Biogenesis of Individual HIV-1 Virions in Live Cells, 454 (2008) 236-240.

[108] D. Gheysen, E. Jacobs, F. de Foresta, C. Thiriart, M. Francotte, D. Thines, M. De Wilde, Assembly and Release of HIV-1 Precursor Pr55gag Virus-Like Particles from Recombinant Baculovirus-Infected Insect Cells, Cell 59 (1989) 103-112.

[109] S. Ivanchenko, W.J. Godinez, M. Lampe, H.-G. Kräusslich, R. Eils, K. Rohr, C. Bräuchle, B. Müller, D.C. Lamb, Dynamics of HIV-1 Assembly and Release, PLoS Pathog 5 (2009) e1000652.

[110] J.A.G. Briggs, J.D. Riches, B. Glass, V. Bartonova, G. Zanetti, H.-G. Kräusslich, Structure and Assembly of Immature HIV, Proceedings of the National Academy of Sciences 106 (2009) 11090-11095.

[111] E.R. Wright, J.B. Schooler, H.J. Ding, C. Kieffer, C. Fillmore, W.I. Sundquist, G.J. Jensen, Electron Cryotomography of Immature HIV-1 Virions Reveals the Structure of the CA and SP1 Gag Shells, The EMBO Journal 26 (2007) 2218-2226.

[112] L. Naldini, U. Blömer, F.H. Gage, D. Trono, I.M. Verma, Efficient Transfer, Integration, and Sustained Long-Term Expression of the Transgene in Adult Rat Brains Injected With a Lentiviral Vector, Proceedings of the National Academy of Sciences 93 (1996) 11382-11388.

[113] J.R. Rosé, L.M. Babé, C.S. Craik, Defining the Level of Human Immunodeficiency Virus Type 1 (HIV-1) Protease Activity Required for HIV-1 Particle Maturation and Infectivity, Journal of Virology 69 (1995) 2751-2758.

[114] S.J. Sofia, V.V. Premnath, E.W. Merrill, Poly(ethylene oxide) Grafted to Silicon Surfaces: Grafting Density and Protein Adsorption., Macromolecules 31 (1998) 5059-5070.

[115] M.-L. Visnapuu, D. Duzdevich, E.C. Greene, The Importance of Surfaces in Single-Molecule Bioscience, Molecular BioSystems 4 (2008) 394-403.

[116] M.P. Elenko, J.W. Szostak, A.M. Van Oijen, Single-Molecule Binding Experiments on Long Time Scales, Review of Scientific Instruments 81 (2010).

[117] A.M. van Oijen, P.C. Blainey, D.J. Crampton, C.C. Richardson, T. Ellenberger, X.S. Xie, Single-Molecule Kinetics of λ Exonuclease Reveal Base Dependence and Dynamic Disorder, Science 301 (2003) 1235-1238.

[118] T. Böcking, F. Aguet, S.C. Harrison, T. Kirchhausen, Single-Molecule Analysis of a Molecular Disassemblase Reveals the Mechanism of Hsc70-Driven Clathrin Uncoating, Nat Struct Mol Biol 18 (2011) 295-301.

[119] E. Cocucci, F. Aguet, S. Boulant, T. Kirchhausen, The First Five Seconds in the Life of a Clathrin-Coated Pit, Cell 150 (2012) 495-507.

[120] K. Xu, G. Zhong, X. Zhuang, Actin, Spectrin, and Associated Proteins Form a Periodic Cytoskeletal Structure in Axons, Science 339 (2013) 452-456.

[121] J. Hodges, X. Tang, M. Landesman, J.B. Ruedas, A. Ghimire, J. Perrault, M.V. Gudheti, J. Gerton, S. Saffarian, Asymmetric Packaging of Polymerases Within Vesicular Stomatitis Virus, Submitted (2013).

[122] N.D. Lawson, E.A. Stillman, M.A. Whitt, J.K. Rose, Recombinant Vesicular Stomatitis Viruses from DNA, Proceedings of the National Academy of Sciences of the United States of America 92 (1995) 4477-4481.

[123] M. Mlodzianoski, Sample Drift Correction in 3D Fluorescence Photoactivation Localization Microscopy, Optics Express 19 (2011) 15009-15019.

[124] R. Courant, F. John, Introduction to Calculus and Analysis, John Wiley and Sons, (1974).

[125] W.E. Lorensen, H.E. Cline, Marching Cubes: A High Resolution 3D Surface Construction Algorithm, Proceedings of the 14th Annual Conference on Computer Graphics and Interactive Techniques, ACM, (1987), pp. 163-169.

[126] J.E.M.a.T.J.R. Hughes, Mathematical Foundations of Elasticity, Dover Publications Inc., (1994).

[127] P.L.T.A. Wriggers, Computational Contact Mechanics, Springer Wein New York, (2007).